Università degli Studi di Udine
PhD programme in
Environmental and Energy Engineering Sciences

Experimental evaluation of biopolymer and synthetic polymer drag reduction in industrial scale facilities

Dott. Ing. Mattia Simeoni

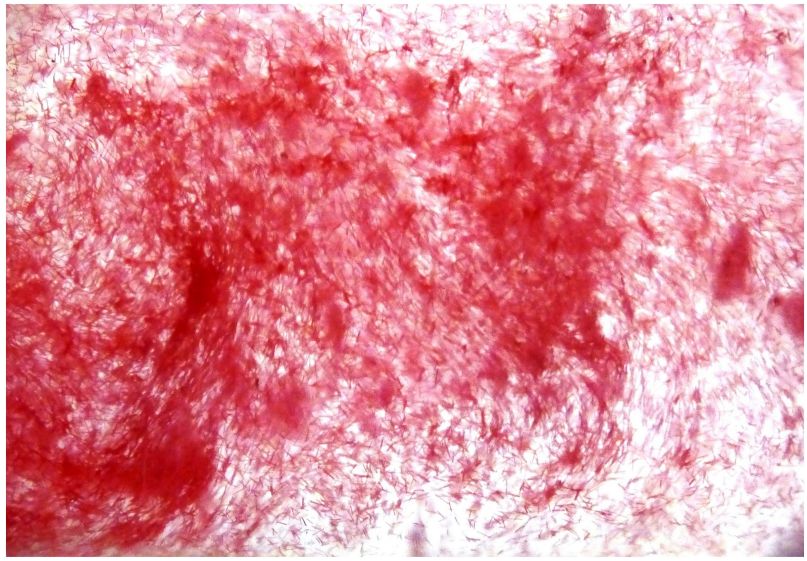

EVALUATION PANEL

Prof. Panagiota ANGELI	Reviewer
Prof. Elisabetta DE ANGELIS	Reviewer
Prof. Sergio CHIBBARO	Referee
Prof. Paolo GUALTIERI	Referee
Prof. Cristian MARCHIOLI	Referee
Prof. Alfredo SOLDATI	Supervisor
Prof. Marina CAMPOLO	Co-Supervisor
Prof. Alfredo SOLDATI	Doctorate Chair

Author's e-mail: mattia.simeoni@uniud.it

Author's address:

Dipartimento di Ingegneria Elettrica
Gestionale e Meccanica
Università degli Studi di Udine
Via delle Scienze, 206
33100 Udine – Italia
mobile. +39 349 0730456
web: `http://www.diegm.uniud.it`

Cover picture: Nylon fibres in turbulent flow (Colored rendering of shadowgraphic image. Real window size 27x18 mm. Re=100,000. Fibers length 300 μm, diameter 20 μm. Fibres concentration 0.25% in weight.).

to my Family

Not everything that counts can be counted,
and not everything that can be counted counts.

William Bruce Cameron

Non non tutto ciò che conta può essere contato,
e non tutto ciò che può essere contato conta.

William Bruce Cameron

Abstract

In this work experimental tests have been performed to investigate drag reduction by polymers in industrial scale pipes (30, 50 and 100 mm ID). Both synthetic (*Polyetylene Oxide, PEO* and *Partially Hydrolysed Polyacrylamide, HPAM*) and bio (*Xanthan Gum, XG*) polymers have been used with the objective of building a self consistent data base to better understand and predict, polymer drag reduction in industrial scale facilities.

To this aim, we run a series of experiments measuring the friction factor at different polymer mass concentrations (100, 500, 750, 1000 and 2000 ppm w/w for the XG; 0.25, 0.5, 1, 5 and 10 ppm w/w for PEO and HPAM) spanning values of Reynolds number in the range 758 to 297 000 (depending on the pipe size). For one polymer (PEO) two different molecular weights have been tested ($4 \cdot 10^6$ and $8 \cdot 10^6\, g/mol$).

The rheology of each of the working fluids (water plus one of the polymers at many different concentrations) has been characterised experimentally before performing tests to evaluate the friction factor. Results are presented in the form of (1) pressure drop per unit length as a function of the bulk velocity in the pipe, (2) using *Prandtl-Kármán* coordinates and (3) as percent drag reduction. Our data are in excellent agreement with data collected in different industrial scale test rigs, compare well with data gathered in small scale rigs and scaled up using empirically based design equations and with data collected for pipes having other than round cross section. The data confirm the validity of a design equation inferred from Direct Numerical Simulation which was recently proposed to predict the friction factor. We show that scaling procedures based on this last equation can assist the design of piping systems in which polymer drag reduction can be exploited in a cost effective way.

Data have also been compared with correlations developed to predict the upper bound for drag reduction when the mechanical degradation of the polymer is taken into account. Our results confirm that these correlations can be operatively used to identify *a priori* polymer performances as drag reducing agents in industrial scale facilities.

Preliminary results to investigate the potential role of polymeric drag reduction in fibre laden flows are also presented.

Contents

List of Figures

List of Tables

1

Introduction

Most industrial processes involve the transport of fluid along pipelines. When the power cost for pumping represents a significant part of the production cost, any reduction of this figure may generate significant savings. Power costs scale with installed power, which depends on pressure loss along the system. There are several kind of drag reducers including surfactants, polymers, fibres and bubbles which are promising for saving pumping energy in fluid transportation of pipelines.

When added to a turbulent flow, polymers are subject to local flow conditions and undergo tumbling, flow orientation, chain stretching and relaxation. The net effect of all these conformational changes appears as an intrinsic elastic stress which alters the flow field [44] and the dynamics of near wall turbulent structures which control the momentum transfer to the wall. The macroscopic result is a dramatic reduction of the friction factor. Such drag reduction has been exploited for flood control in sewer system, fire fighting systems, dredging operations, drilling applications and for the improved transport of suspended solids (see [42]). For those applications in which the long term accumulation of the polymer in the receiving environment or the contamination of the (solvent) fluid are issues of concern, bio-polymers are used instead of traditional synthetic polymers since they can be bio-degraded more easily.

Despite the variety of potential applications, guidelines to design large scale systems are still lacking: homogeneous sources of experimental data collected in large size pipes are limited and design is based on empirical correlations fitted on data collected in small scale pipes with inevitable uncertainties in the use of such correlations at industrial scale. In recent years, complementary theory has been proposed to describe the mechanisms responsible for drag reduction (see the review by [77]) and numerical experiments have been performed to examine the implications of the theory and how they compare with reality: Direct Numerical Simulations (DNS) of turbulent drag reduction by polymers elucidated the role of viscosity profile [10], polymer relaxation time [51], polymer elasticity [57], effective wall viscosity [31], and of the dynamic interaction between polymer and vortices ([14, 44] among others) on the redistribution of turbulent energy in the wall layer which induces the drag reduction. The main advantage of numerical experiments is that the effect of polymer properties (such as elasticity, stretching and concentration),

domain geometry and flow conditions can be more easily isolated and studied. Nevertheless, the correctness/adequacy of the underlying physical model needs to be corroborated *a posteriori* by independent experimental data [14]. Recently Housiadas and Beris [31], building on the systematic analysis of their DNS database, proposed a parametric relationship to predict friction factors in visco-elastic turbulent flows. This relationship could be potentially used to assist the design of piping systems exploiting polymer induced drag reduction. In such systems, a critical issue is to identify how long or under which condition, the polymer remains effective as drag reducing agent.

Vanapalli *et al.* [72] proposed a theory to predict the maximum level of drag reduction which can be achieved considering the effect of the mechanical degradation of polymers chains; the proposed correlations can be profitably used to predict the actual upper bound value of drag reduction for the flow conditions and pipeline characteristics.

The object of this work is to build a self consistent data set investigating turbulent drag reduction produced by synthetic and bio-polymers in pipes of different sizes (30, 50 and 100 mm ID). The final aim is to *i)* experimentally study the drag reduction phenomenon in large pipes, close to the industrial application, comparing results with available data from the literature (often obtained in very small pipes); *ii)* compare the effects of synthetic and bio-polymers; *iii)* validate new theoretical relations to predict the drag reduction in different pipe diameters taking into account polymer mechanical degradation; *iv)* evaluate the cost effectiveness of polymer drag reduction; *v)* assess the effectiveness of polymers as drag reducing agents in more complex flows (like fibres suspensions).

In this chapter, a brief literature review is presented; in chapter 2 the experimental rigs are described together with the materials and instrumentations used. In chapter 3 drag reduction results obtained using the bio-polymer are presented together with predictive correlations to be used for *a priori* evaluation of drag reduction in pipelines; a cost effectiveness analysis is also proposed. In chapter 4 the results obtained investigating the synthetic polymers are presented and compared with the upper bound value expected when mechanical degradation of polymer is accounted for; in chapter 5 a final discussion is presented; in chapter 6 preliminary results obtained in fibres suspension flows are presented.

1.1 Turbulent transport of fluid

In engineering applications turbulent flows are prevalent: liquids or gasses moving through pumps, compressors or along pipelines are typically turbulent. Turbulent flows are characterized by a non-dimensional parameter, the *Reynolds number*, defined as

$$Re = \frac{\rho u D}{\mu} \tag{1.1}$$

where ρ and μ are fluid density and dynamic viscosity while u and D are the section-averaged axial velocity (mean bulk velocity) and the pipe diameter. In pipe flows, as long as the Reynolds number remains lower than about 2300, the flow is laminar: fluid paths do not change with time and all the streamlines are parallel to the pipe axis. Laminar flows are characterised by viscous dissipation. When Reynolds number exceeds 4000[1] the flow becomes turbulent: streamlines modify over time and a chaotic state of the fluid is present. In this kind of flow, inertial dissipation caused by turbulent structures (coherent structures), is added to the viscous; the dissipation caused by the fluid motion will lead to a pressure loss.

Obtaining predictive relations between the flow rate and the pressure drop is a main issue for the design of industrial lines since it is crucial for the correct sizing of pumps and the economical benefit of the transport. These relations, which can be used for pure fluids, are not equally reliable for complex fluids (i.e. fluids with additives, with suspended solids and fibres).

1.1.1 Velocity profile in turbulent pipe flow

For the turbulent pipe flow a dimensional analysis can give insight into the mean velocity profile in the near-wall region. The scaling parameters are u_τ, ρ and μ; where u_τ is the friction velocity defined as

$$u_\tau = \sqrt{\frac{\tau_w}{\rho}} \tag{1.2}$$

with

$$\tau_w = \frac{D\Delta P}{4L} \tag{1.3}$$

being the mean shear stress at the wall.
The velocity profile can be written as[2]

$$U_z^+(y^+) = y^+ \quad if \quad 0 < y^+ < 5 \tag{1.4}$$

$$U_z^+(y^+) = A \ln y^+ + B \quad if \quad y^+ > 30 \tag{1.5}$$

where $U_z^+(y^+) = U_z(y^+)/u_\tau$ and $y^+ = (R^+ - r^+)$.
The flow domain in pipes can be divided into three regions: *i)* the *viscous sublayer*, $y^+ < 5$; *ii)* the *buffer layer*, $5 < y^+ < 30$ and *iii)* the *logarithmic layer*, $y^+ > 30$. For fully developed turbulent pipe flows (high *Re* numbers), $A = 2.5$ and $B = 5.5$.

[1] As the Reynolds number is increased, the transition from laminar to turbulent occurs over a range of *Re*.

[2] In cylindrical coordinates z represents the axial direction; superscript $^+$ denotes non-dimensional units.

1.1.2 Friction factor and pressure drop

Skin friction arises from the interaction between a fluid and the surface over which it is moving and it leads to a pressure loss. The *friction factor* may be defined as

$$f = \frac{\tau_w}{\frac{1}{2}\rho u_b^2} \tag{1.6}$$

where u_b is the mean bulk velocity[3]. For laminar pipe flows (Poiseuille flows)

$$f = \frac{16}{Re} \tag{1.7}$$

After the transition to turbulence, a Newtonian solvent follows the empirical Blasius friction law for smooth pipes

$$f = 0.079 Re^{-0.25} \tag{1.8}$$

A more accurate equation, still for the turbulent regime and valid for a broader range of Reynolds numbers, is that proposed by von Kármán-Nikuradse

$$\frac{1}{\sqrt{f}} = 1.7 \ln\left(Re\sqrt{f}\right) - 0.4 \tag{1.9}$$

For rough pipes, taking into account the roughness of the inner surface, the Colebrook equation can be used

$$\frac{1}{\sqrt{f}} = -1.7 \ln\left(\frac{k}{D} + \frac{4.67}{Re\sqrt{f}}\right) + 2.28 \tag{1.10}$$

When the pressure drop is known from the experimental measurements, the friction factor can be obtained by equations (1.3) into (1.6).

1.1.3 Characterization of polymer solutions

A polymer is a high molecular mass macromolecule composed by a number N of repeating units (monomers); N can reach very high values, up to 10^5 [12]. We can refer to the *polymer chain* as the whole or a part of the macromolecule [40]; the length of the chain is proportional to the number of monomers present in the macromolecule. Once the polymer is added to a still solvent, its characteristic dimension can be defined either by its *radius of gyration* R_G, typical of flexible polymers and representing the root-mean-square of chain end-to-end distance or its length, typical of rod-like polymers (see fig. 1.1).

The molecular affinity between the solvent and the polymer chain (here after indicated as solvent quality) influences the polymer conformation. Two

[3]This form of the friction factor is referred to Fanning's friction factor; it must be paid attention to do not confuse this expression with the Darcy-Weisback form which is four times higher.

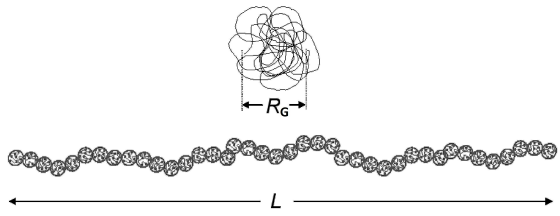

Figure 1.1: Radius of gyration of a flexible polymer (top) and length of a rod-like polymer (bottom). Adapted from Colby [7].

categories can be distinguished: *neutral polymers* and *polyelectrolytes*. The formers do not have, within their chain, any electrical charge or ionizable groups (such as Polyethylene Oxide), the latter have ionizable or ionic groups [40] (such as some bio-polymers, like Xanthan Gum). Depending on the the interaction between the monomers and the solvent molecules, three conditions can be defined:

- good solvent;
- theta solvent (θ-solvent);
- poor solvent.

If we consider a dilute solution, polymers exist as individual chains (see fig. 1.2). In the case of a neutral polymer in good solvent, the interactions between polymer monomers and solvent molecules are energetically favourable, and will cause polymer coils to expand (the radius of gyration increases). Conversely for a poor solvent, monomers self-interactions are preferred, and the polymer coil will contract (the radius of gyration decreases). In the θ-solvent condition, monomer-monomer attraction and repulsion is cancelled and the individual chain behaves essentially as ideal polymer [23]. In the case of a polyelectrolyte solution, charge repulsion dominates and this keeps the chains apart and straight. The quality of the polymer-solvent coupling depends on both the chemical compositions of the polymer and solvent molecules and the solution temperature.

The monomer-monomer interaction, which depends on the quality of the solvent, will affect the capability of the polymer to be stretched and hence its ability in reducing drag. The presence of elements in the solvent which can yield to poor solvent condition (like salt, see [61] among others) will determine a contraction of the coil, in the case of neutral polymers or an increased flexibility, in the case of rod-like polymers (giving a reduction in the chain length) both resulting in a decreased drag reduction. In can be stated that the polymer-solvent coupling is one of the main factors influencing the drag reduction efficiency. The radius of gyration, for flexible linear molecules

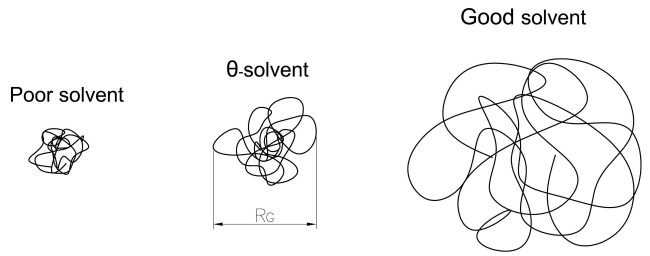

Figure 1.2: Neutral polymer conformation depending on solvent's quality. Adapted from Colby [7].

in good solvent, can be expressed as

$$R_G \approx N^{\frac{3}{5}} a \tag{1.11}$$

with a monomer's size [12].

If an external force (for example the shear in a wall bounded flow) is applied to the polymer chain, once a critical value is exceeded, the polymer will deform proportionally to the strength applied (see fig. 1.3); this phenomenon is called *coil-stretch transition* [11]. Once this condition is released, it will take some time to the polymer to restore the initial conformation. The average time taken by a stretched polymer to return to a coiled configuration is defined *polymer relaxation time* T_z (see Zimm, 1956 [82]). Polymer relaxation time can be related to the properties of the

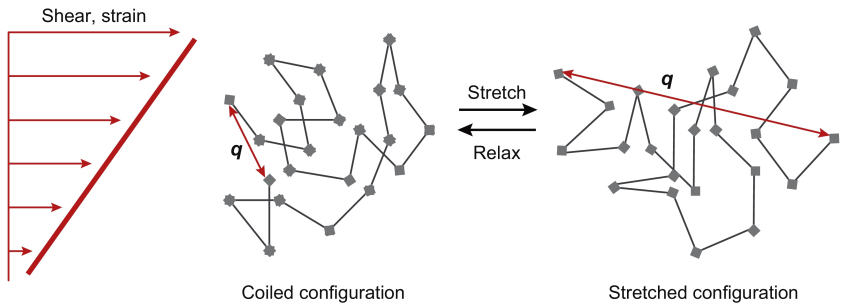

Figure 1.3: Schematic of polymer stretch and relaxation, in shear flow. From White & Mungal [77].

polymer molecule; Flory (1976) [23] proposed the following expression

$$T_z = \frac{\eta_0 R_G^3}{kT} \tag{1.12}$$

where k is the Boltzmann constant, T is the solution's temperature, η_0 is the solvent viscosity and R_G is the radius of gyration.

The initial conformation of the polymer chain influences the facility by which the flow can deform the polymer and the flow scales with which it will interact. If the polymer-solvent coupling is favourable, the radius of gyration is larger and the polymer chain can be more easily deformed under shear; this means that polymer deformation can occur at lower values of the friction strain rate. Contrary, if the solvent is poor, the radius of gyration decreases and the shear needed to obtain a certain deformation raises; this means that higher values of the strain rate have to be reached. This phenomenon is strongly related, as it will be shown later on, with drag reduction onset and efficiency.

Depending on the concentration of the polymer in the solvent, different regimes can be defined (refer to fig. 1.4):

- dilute;
- semi-dilute;
- entangled.

In dilute polymer solutions, the interactions between the coils are negligible and conformations of individual chains are controlled by intramolecular interactions. The average distance between individual polymer coils is much larger than the characteristic size of a coil [43]; the upper limit for this regime is represented by the *overlap concentration* c^*. At c^* the polymers chains start to physically interact, for $c > c^*$ the regime is *semi-dilute unentangled*. The free volume is reduced with increasing the polymer concentration and there is a progressive interpenetration of the coils. The upper bound for this regime is the so called *entanglement concentration* c_e. Above this limit, there is no more free space for the molecules and a network between the coils has been built up (*semi-dilute entangled* regime). It is no more possible to refer to the single coil and the characteristic dimension is now the size ζ of the network mesh. The upper bound for this regime is the concentration c^{**}; above this value, the regime is considered *concentrated*. In figure 1.4 the zero shear rate viscosity[4] is plotted as a function of polymer concentration: the aforementioned regimes can be recognised. It can be seen that the change in the polymer regime coincides with a change in the slope of the viscosity with respect to concentration. In particular, at the overlap concentration, where polymers coils start to physically interact, there is an abrupt increase of the viscosity within a small range of concentrations. Beyond the final critical concentration c^{**}, the solution's behaviour strongly depends on the solvent quality.

Polymer solutions present a non-Newtonian behaviour of the viscosity with respect the the shear rate. In particular they can be considered as *visco-elastic fluids*: the reaction of the fluid to an external force, depends on the

[4]The viscosity at the limit of low shear rate. In other words, the maximum plateau value attained as shear stress or shear rate is reduced. Zero-shear viscosity is effectively the viscosity of a product at rest.

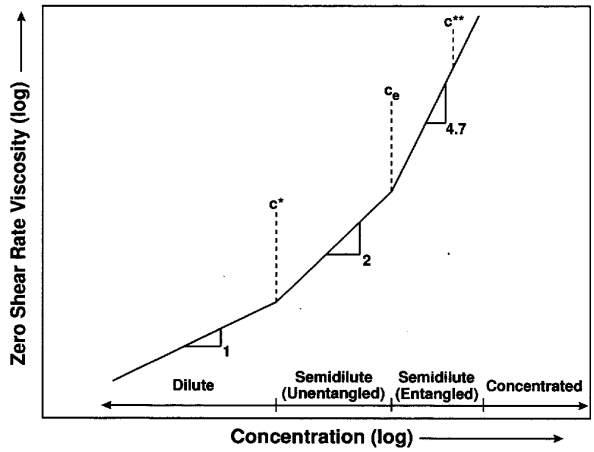

Figure 1.4: Zero shear rate viscosity scaling as a function of concentration. From Wyatt [78].

characteristic time of the deformation with respect to the polymer's relaxation time. A visco-elastic system can be represented as a spring & dashpot model: for quick deformations it reacts as a spring while for slow deformations it reacts as dashpot (Maxwell's model, see fig. 1.5). This means that in the case of a long-time deformation the medium behaves like a viscous flow while, for a short time deformation, it behaves like an elastic solid. To

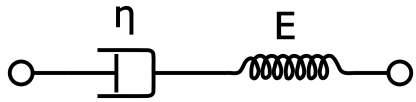

Figure 1.5: Maxwell's spring & dashpot model for visco-elastic behaviour: η representing the viscous component and E, the elastic modulus, representing the elastic part.

characterize the behaviour caused by a specific strain on the flow element, the *Weissemberg number* can be defined: it represents the ratio between the polymer characteristic time scale (i.e. polymer relaxation time) and the flow time scale of the near-wall turbulence

$$We = \frac{T_z}{t_{def}} = \frac{T_z \rho u_\tau^2}{\mu_s} \tag{1.13}$$

When $We \to \infty$ the fluid acts like an elastic solid while, when $We \to 0$ it acts like a viscous fluid. When a slow deformation is applied, the polymers chains can slip one respect to the other allowing a viscous behaviour; conversely, in

the case of quick deformation, there is no possibility of unentanglement of the coils and the response will be like an elastic solid.

The visco-elastic behaviour is more pronounced with increasing polymer concentration and the properties of a visco-elastic polymer solution can be characterised by rheology measurements. In figure 1.6 the shear viscosity of different xanthan gum solutions is shown. As can be seen the viscosity

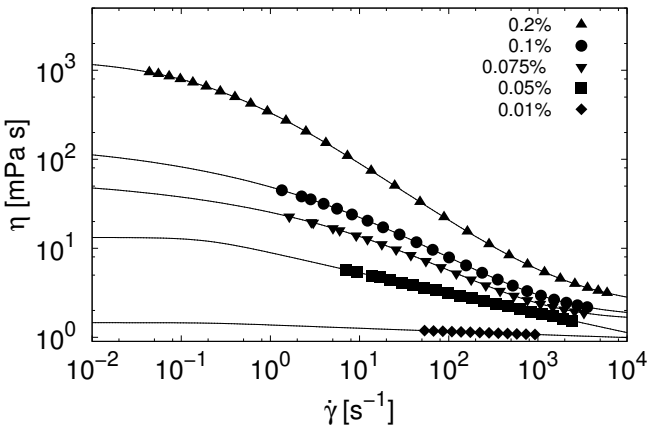

Figure 1.6: Measured shear viscosity of different xanthan gum solutions at $20°C$; experimental data fitted by the Carreau-Yasuda model [81]. Adapted from Campolo *et al.* [4].

decreases with increasing the shear rate, typical of a *shear-thinning* behaviour. With increasing polymer concentration, the shear-thinning effect is more pronounced. Three regimes can be identified with increasing the shear rate: *i)* an initial zero shear rate Newtonian plateau; *ii)* a power law region where the viscosity decreases almost linearly and *iii)* another Newtonian plateau at very high shear rate values. In this case, the experimental values have been fitted using the Carreau-Yasuda model, which represents the shear-thinning behaviour of the viscosity as a function of different parameters

$$\frac{\eta - \eta_\infty}{\eta_0 - \eta_\infty} = \frac{1}{[1 + (\lambda\dot{\gamma})^a]^{n/a}} \tag{1.14}$$

where η_0 is the zero shear rate viscosity, η_∞ is the value of the viscosity at high shear rates, λ represents the inverse shear rate at the onset of shear-thinning, n is tha power law index and a is a fitting parameter introduced by [81]. To characterise the prevalence of an elastic or viscous behaviour of a solution, rheological oscillatory test should be performed. In this case, the specimen is deformed applying a sinusoidal cycle, which can be express as

$$\gamma = \gamma_0 = sin(\omega t) \tag{1.15}$$

where γ_0 is the maximum value of the deformation and ω is the frequency of the oscillation. Due to the applied deformation, the fluid will react with a tangential stress

$$\sigma(t) = \sigma_0 sin(\omega t + \delta) \tag{1.16}$$

This means that σ will vary at the same frequency as γ but with a phase displacement δ. In figure 1.7 three cases can be distinguished: *i)* if the behaviour is like an elastic solid, the deformation γ and the shear stress σ will be in phase ($\delta = 0$); *ii)* in the case of pure viscous fluid, there will be a displacement between the phases equal to $\pi/2$; *iii)* in the visco-elastic situation, the phase displacement will be intermediate between the elastic solid and the viscous fluid with $0 < \delta < \pi/2$.

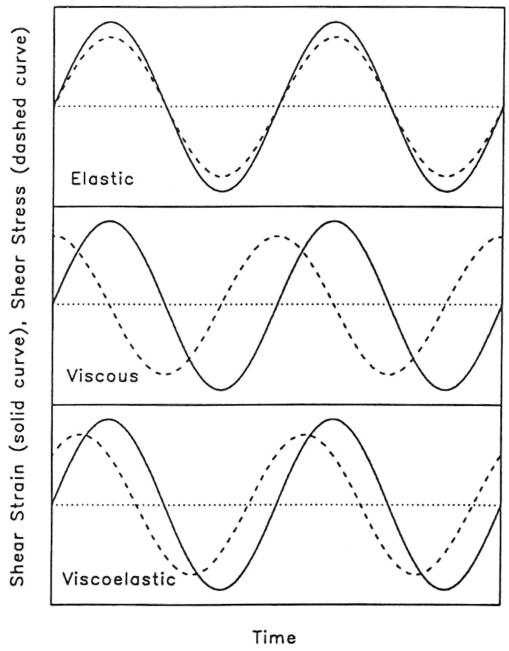

Figure 1.7: Top to bottom: γ (solid lines) and σ (dashed lines) phase behaviour for elastic solid, viscous and visco-elastic fluid.

The visco-elastic behaviour can be hence represented as the sum of an elastic and a viscous component; the consequent shear stress can be written as

$$\sigma = \sigma_0 cos\delta sin(\omega t) + \sigma_0 sin\delta cos(\omega t) \tag{1.17}$$

Dividing by the maximum deformation γ_0 (see Eq. (1.15))

$$\frac{\sigma}{\gamma_0} = G' sin(\omega t) + G'' cos(\omega t) \tag{1.18}$$

where G' and G'' are the *storage modulus* and the *loss modulus*. The first one is related to the elastic component of the fluid while the second to the viscous and dissipative one. Measuring this two quantities allows to better characterise the visco-elastic behaviour of a polymer solution. In figure 1.8 the storage and loss moduli for guar and xanthan gum solutions are shown for different polymer concentrations. If we consider figure 1.8a,

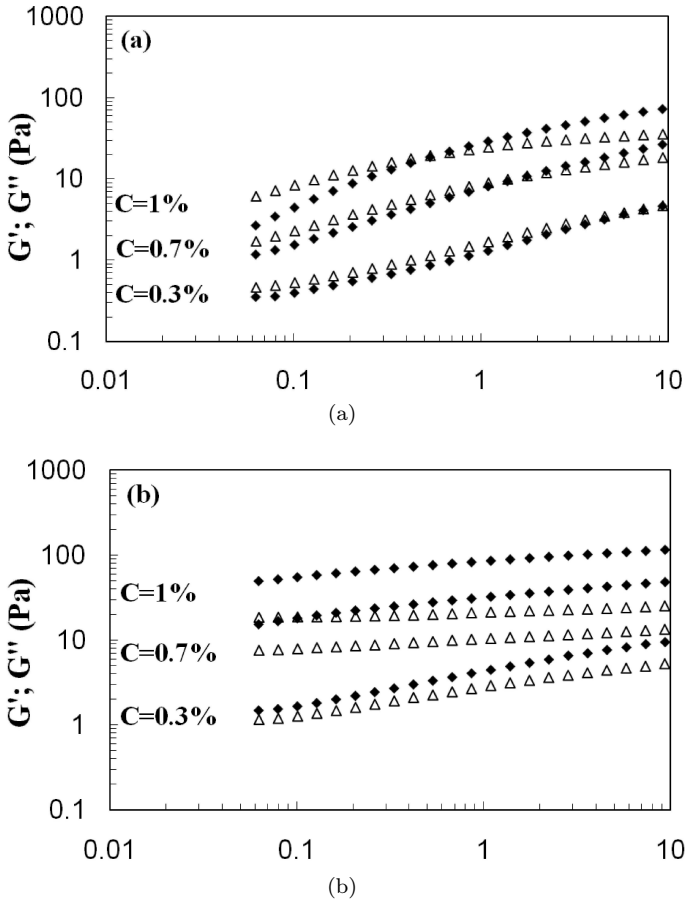

Figure 1.8: Dynamic moduli as a function of frequency for dispersions with different gum concentrations at $20°C$. G': full symbols; G'': open symbols: (a) Guar gum and (b) Xanthan gum. From Moraes [52].

it can be seen that, for a given concentration (e.g. 1%), at low frequency (slow deformation) $G'' > G'$: there is enough time for the polymer chains to slip one respect to the other toward a more favourable energetic state; the fluid behaves like a viscous flow. At high frequencies, the deformation is too quick to allow the chain slippage and the entangled coils form a non

deformable network; $G' > G''$ and the fluid behaves like an elastic solid. It can be noticed that, increasing the polymer concentration, this tendency in more pronounced and the storage modulus overcomes the loss modulus at a lower value of the frequency.

1.2 State of the art in polymer drag reduction

One way to reduce the friction factor in turbulent flows is to add a small amount of polymers to the fluid. A polymer is a macromolecule, with high molecular weight, composed of a huge number of repeating structural units, connected by chemical bonds. Polymers are largely used in many applications and are widely encountered in our life: natural rubber and cellulose are natural polymers; synthetic rubber, Bakelite, neoprene, nylon, PVC, silicone and many others are synthetic ones.

Drag reduction phenomenon is the reduction of the skin friction of a turbulent flow, by additives; it manifests itself as a change in the relation between the mean pressure drop ΔP along the pipe, and the flow rate Q: the flow rate is increased if the pressure drop is kept constant or the pressure drop decreases if the flow rate is held constant. It follows that two definitions of drag reduction can be used

$$DR_Q = \left(1 - \frac{\Delta P_P}{\Delta P_N}\right) \cdot 100\% \tag{1.19}$$

$$DR_{\Delta P} = \left(1 - \frac{Q_N}{Q_P}\right) \cdot 100\% \tag{1.20}$$

where subscript $_P$ stands for polymer solution while $_N$ stands for the Newtonian single phase flow. With respect to the data available in literature, the behaviour of a polymer solution, at increasing Reynolds number, can be depicted as follows: at low Re numbers, where the flow is laminar, the addition of a small amount of polymers, does not influence the shear viscosity of the fluid which follows equation (1.7). After the transition to turbulent, the flow will follow equations (1.8), (1.9) or (1.10) only up to a certain value of Re defined as *"drag reduction onset Reynolds number"*; beyond that point, the friction factor will be lower than that of the solvent alone.

The drag reducing behaviour is influenced by several parameters such as the polymer concentration, the type of solvent, the type of polymer and its characteristics [61] (flexibility, molecular weight, chemical composition) and the pipe diameter. Virk, in 1975 [74], found the existence of a *Maximum Drag Reduction Asymptote (MDR)*: a lower bound for the friction factor exists for each Reynolds number and can be reached irrespective of the type of solvent/additive system used. The expression for the so called *Virk's asymptote* is

$$\frac{1}{\sqrt{f}} = 19.0 \log_{10}\left(\frac{1}{2} Re \sqrt{f}\right) - 32.4 \tag{1.21}$$

Figure 1.9 depicts the possible behaviour of a drag-reducing polymer solution

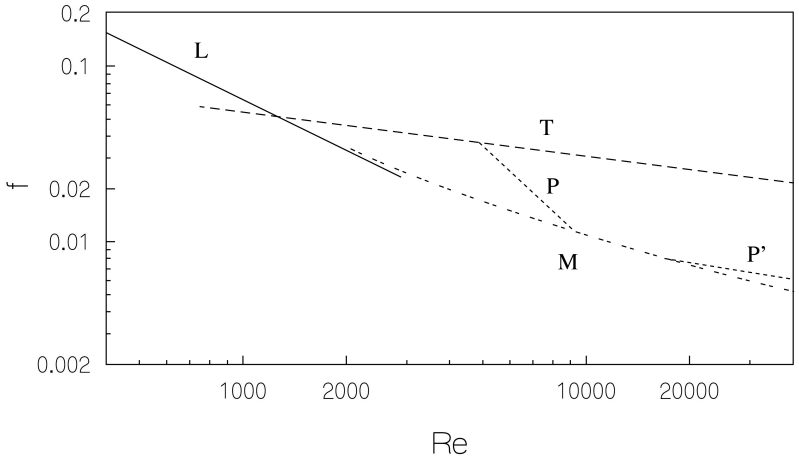

Figure 1.9: The friction factor as a function of the Reynolds number in a pipe flow: possible drag reduction trajectories. L: Eq. (1.7), T: Eq. (1.8), M: Eq. (1.21), P, P': drag reduction lines. From Toonder J. M. [36].

in a pipe. When increasing Re the following trajectories are obtainable: L→T for Newtonian flow while, for drag-reducing polymers: L→T→P→M, L→M, L→M→P'. The position of lines P and P' depends on the parameters listed just above (refer to [61] and [74] among others). Regarding the pattern followed by different polymer solution, it is possible to mention some important results: Wirk & Wagger in 1990 [75] found that linear, high molecular weight polymers, are more effective in reducing drag. Moreover, they showed that initial polymer shape has large influence on the drag reduction. For example, a variation of the salinity of the solvent resulted in the variation of the initial structure of the polymers, from randomly-coiled to extended. For an initially coiled conformation, the most common trajectory is L→T→P→M while, when polymers are already extended, the trajectory was found to be L→M→P'. It is possible to conclude that, in the latter case, there is no drag reduction onset number; the flow becomes drag reduced as soon as it becomes turbulent. Sasaki in 1991 [61], by adding salt to the polymer solution, found that the drag reduction ability decreases when the polymer becomes more flexible.

Analysing more in detail the measurements done by various authors, it is clear that polymer additives have an influence on the mean flow velocity profile: the viscous sublayer, Eq. (1.4), is not changed by the addition of a small quantity of polymers; conversely the buffer layer is thickened leading to an offset of the logarithmic region. This means that the new profile lies above Eq. (1.4), for $y^+ > 30$, which is consistent with drag reduction. Harder & Tiederman (1991) [29], demonstrated that the shift of

the logarithmic profile is not parallel to the universal profile of the turbulent pipe flow, as proposed for example by Virk [74], rather the slope A increases for drag-reduced flows. Moreover, it has been shown that the turbulent shear stress is suppressed by the addition of polymer additives; this implies a decreased correlation between the streamwise and the normal velocity fluctuations [56]. In a fully developed pipe flow, the mean shear stress T is a linear function of the radial coordinate between the zero value and the centreline; in polymer flows, it can be written as the sum of the turbulent shear stress T_r (Reynolds stress), the viscous stress T_s and the polymeric stress T_p

$$T = T_r + T_s + T_p \tag{1.22}$$

In figure 1.10a the behaviour of the Reynolds and viscous stresses are reported for a Newtonian flow; the sum of the two contributions gives the mean shear. In figure 1.10b the contributions to the main shear for a 20 wppm Partially Hydrolysed Polyacrylamide (HPAM) solution are shown: in this case, also the polymer contribution is present and the Reynolds contribution is reduced. If the polymer concentration is increased (see fig. 1.11a) to 103 wppm, the Reynolds contribution is strongly reduced while the polymer one increases: the fact that the sum of the Reynolds and viscous contribution no longer equals the mean shear is called *Reynolds stress deficit*. Increasing the polymer concentration, the main contribution to the total stress comes from polymers (see fig. 1.11b) [56].

Regarding the turbulent energy production, Harder & Tiederman [29] found that it is decreased upon the addition of polymers. Nevertheless, a deeper analysis shows that the turbulent energy in the stream-wise velocity component is increased while the energy of the wall-normal velocity is dumped. Moreover, power spectra indicate that, for the streamwise component, turbulent energy is redistributed from small scales to large scales whereas normal velocity fluctuations are suppressed over all scales. From these evidences it is possible to conclude that polymers change the structure of turbulence, rather than simply attenuating it, and its energy budget, by the appearing of non-Newtonian terms. In figure 1.12a the mean flow energy budget for a water flow is shown with P_u the production of mean flow energy by the imposed pressure gradient, D_u the deformation work and E_s the viscous dissipation by the mean flow (please refer to [56] for details and equations). If this plot is compared with figure 1.12b, where E_p is the dissipation by mean polymeric stresses, it can be seen that in polymeric flows, most of the energy is transferred directly to the polymers rather than to the turbulent structures [56].

As mentioned above, many experiments confirmed that the viscous sublayer has a passive role in the drag reduction phenomenon while polymer molecules seem to interact with the turbulence in an annulus just above the viscous sublayer: $10 < y^+ < 100$ (see Tiedermann *et al.*, 1985 [71]).

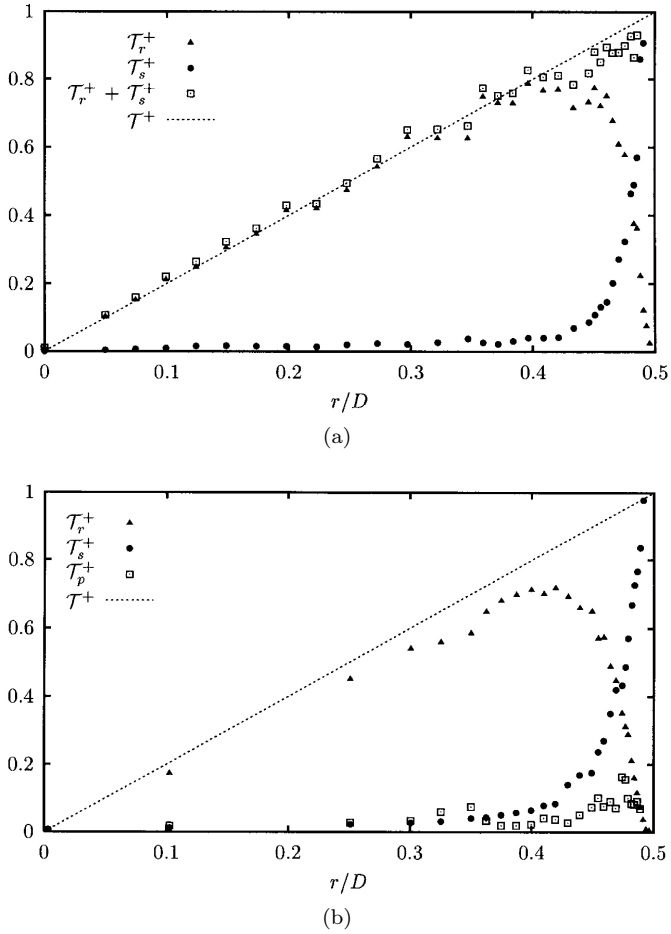

Figure 1.10: (a) The various contributions to the mean shear stress for water as a function of the pipe radius. (b) Contributions to the pipe shear stress for a 20 wppm HPAM solution. From Ptasinski *et al.* [56].

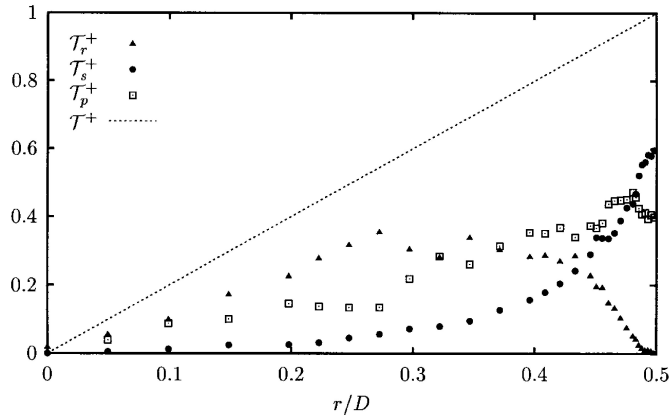

(a)

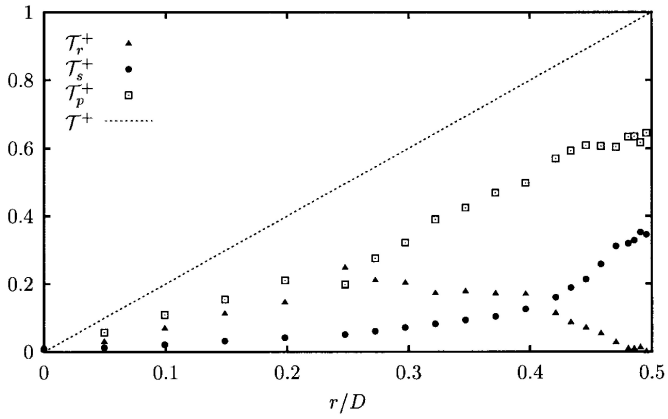

(b)

Figure 1.11: (a) Contributions to the pipe shear stress for a 103 wppm HPAM solution. (b) Contributions to the pipe shear stress for a 435 wppm HPAM solution. From Ptasinski *et al.* [56].

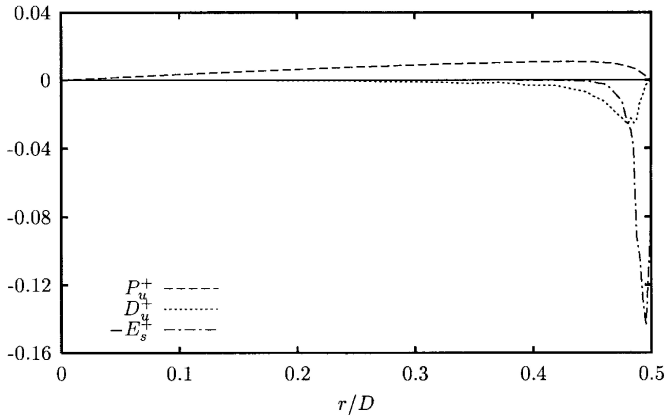

(a)

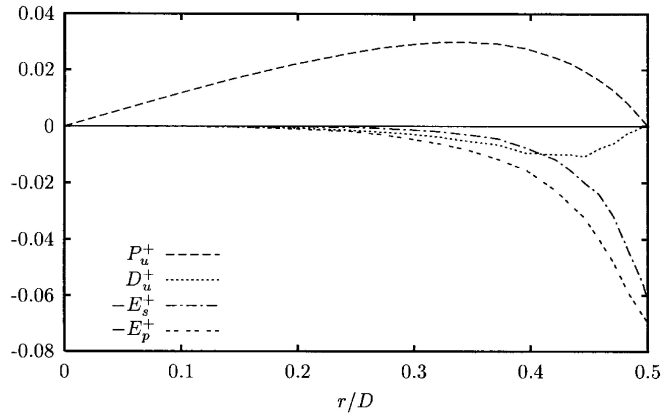

(b)

Figure 1.12: (a) Mean flow energy budget terms for water; $Re \approx 9600$. (b) Mean flow energy budget terms for 175 wppm HPAM solution; $Re_w \approx 9800$. From Ptasinski *et al.* [56].

We may now summarize these evidences as follows:

- drag reduction is bounded between two asymptotes: the von Kármán equation for Newtonian turbulent flows and a maximum drag reduction asymptote (see Eq. (1.9), (1.21) [74]);
- in fully turbulent pipe flow, dilute polymer solutions exhibit three distinct regimes, as the flow rate increases [77]:
    1. a regime without drag reduction: friction factor as von Kármán;
    2. a regime with drag reduction in which the friction factor depends upon the nature of the polymer solution;
    3. an asymptotic regime of maximum possible reduction; the friction factor relation is insensitive to the polymer solution employed.
- the viscous sublayer has a passive role in drag reduction phenomenon [71];
- the buffer layer is thickened, leading to an offset of the logarithmic region [74];
- the slope of the logarithmic mean velocity profile is slightly increased [29];
- the peak of the stream-wise turbulence intensity is increased and shifted away from the wall [56];
- the radial turbulence intensity is decreased throughout the pipe [56];
- the turbulence shear stress is suppressed and shows the so-called "Reynolds stress deficit" [29];
- the measured spectra show that the stream-wise turbulent energy is redistributed from small to large scales [29];
- the radial turbulent kinetic energy is dumped over all scales [29].

1.2.1 Drag reduction mechanism

In this paragraph an outline of the latest studies on the drag reduction mechanism will be presented; the analysis will start from the macroscopic evidences and will then enter more in detail up to the turbulent scales involved in the drag reduction mechanism.

Drag reduction leads to a decrease in the friction factor with respect to that of the solvent alone; analysing more in detail the behaviour of the flow, it was found that the mean velocity profile shows an offset due to the thickening of the buffer layer (see fig. 1.13). The offset of the logarithmic layer was observed both experimentally (see Den Toonder *et al.*, 1997 [37]) and numerically (see Virk [74], Den Toonder *et al.* [37], Dubief *et al.*, 2004

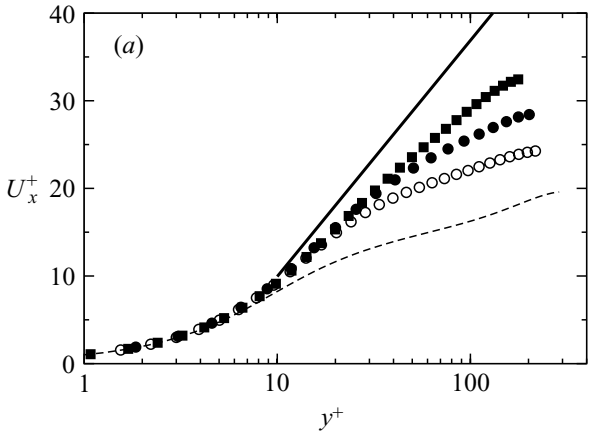

Figure 1.13: Mean velocity profile scaled with inner variables. —— MDR, − − − 0% DR, ∘ 35% DR, • 47% DR, ■ 60% DR. From Dubief *et al.* [15].

[15] among others). Another characteristic of polymer solution is the increase of the streamwise velocity fluctuations and at the same time, the decrease of the wall-normal velocity fluctuations (see fig. 1.14). The consequence of the

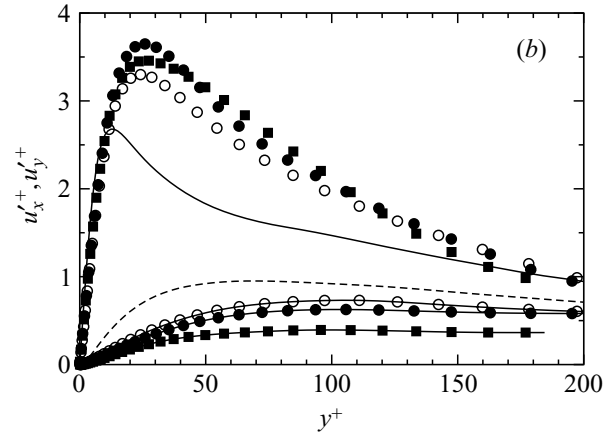

Figure 1.14: RMS of velocity fluctuations scaled with inner variables. Newtonian simulation (DR=0%): ——, $u_x'^+$; − − −, $u_y'^+$. For visco-elastic simulations, symbols are the same as for fig. 1.13; $u_x'^+$ is denoted by symbols only; $u_y'^+$ is indicated by symbols connected by —. From Dubief *et al.* [15].

wall-normal velocity fluctuations reduction is the damping of the Reynolds

shear stress (the mentioned Reynolds stress deficit, see fig. 1.15)

$$\tau_{Re} = \langle u\, v \rangle \tag{1.23}$$

The conclusion is that polymers interact and modify the near-wall turbulence

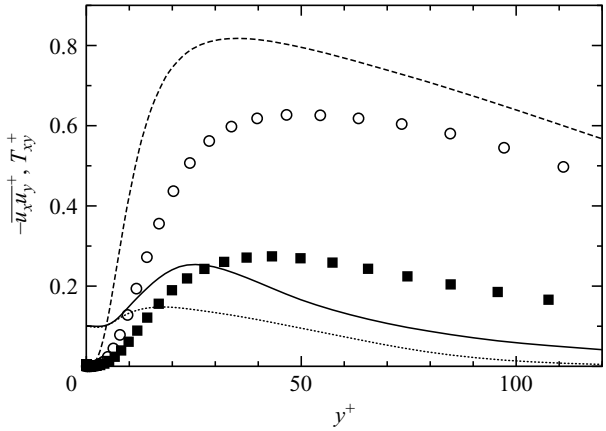

Figure 1.15: Reynolds shear stress (dashed line and symbols as previous figures) and polymer stress ($\cdots$, DR=35%; ——, DR=60%) normalized by u_τ and ν. From Dubief *et al.* [15].

structure. This assumption is confirmed by two evidences: first, the laminar pipe flow of dilute polymer suspensions shows no significant differences in the skin friction with the laminar pipe flow of Newtonian fluids. Second, for a fixed pipe diameter, the Reynolds number at which drag reduction appears depends on the number of monomers in the macromolecule [77]. This implies an interaction since turbulence dynamics depends on Re number and polymer dynamics on the number of monomers.

The first parameter controlling the possibility of turbulence/polymer interaction is the *time criterion* (see Lumley, 1969 [48]): drag reduction may occur if the polymer relaxation time is longer than a representative time scale of the near wall turbulence

$$T_z > \frac{\mu_s}{\rho u_\tau^2} \tag{1.24}$$

where μ_s is the viscosity of the solution, ρ is the density of the solution and u_τ is the friction velocity (see Eq. (1.2)). According to this criterion, drag reduction occurs when the previously mentioned wall-shear *Weissenberg number* is of order unity [66].

In the past, two main theories were proposed trying to explain the drag reduction phenomenon (see review by White & Mungal, 2008 [77]); the first focuses on viscous effects (see Lumley, 1969 [48]), the second on elastic

effects (see Tabor & de Gennes, 1986 [70]). Regarding the viscous effect, the basic explanation is that the stretching of polymers leads to an increase of the effective viscosity[5]. In wall-bounded turbulent shear flow polymers are primarily believed to be stretched in the buffer layer, just outside the viscous sublayer, leading to a large increase in the elongational viscosity[6]. This increase of the effective viscosity causes the suppression of the turbulent fluctuations and the thickening of the buffer layer yielding to a reduced friction factor. It is not straightforward to understand why an increased viscosity of the medium should lead to a reduction in the friction factor but, if we consider a turbulent flow, where turbulent structures are involved in the energy dissipation giving an increase in drag, a growing in the flow viscosity will lead to a reduced production of these structures yielding to a lower friction loss. This approach could be considered as a change in the rheological properties of the medium.

The researchers in favour of the elastic theory [70] conversely suggest that the strain rates, close to the wall, although high, fluctuate both in time and space and can produce only a partial stretching of the polymers and that, if moderately stretched, the polymers produce no measurable change in viscosity. Hence it has been postulated that the major role in drag reduction phenomenon is due to the elastic energy stored by the partially stretched polymers. According to this assumption, this theory predicts that the onset of drag reduction occurs when the cumulative elastic energy stored by the partially stretched polymers becomes comparable with the kinetic energy in the buffer layer at some turbulent length scale larger than the Kolmogorov scale. The well-known Kolmogorov-type energy cascade is then terminated prematurely, and scales below this cut-off scale are believed to behave elastically (see Joseph, 1990 [41]). Hence (see Sreenivasan & White, 1999 [67]), for a given combination of the polymer and the flow, there should exist a turbulent length scale r^* whose time scale τ_{r^*} matches T_z (see fig. 1.16). This time scale is given by the relation

$$r^* = u_{r^*} \cdot T_z \tag{1.25}$$

where the velocity u_{r^*} characteristic of the scale r^*, is given by Kolmogorov (1941) to be

$$u_{r^*} = \left(r^* \langle \epsilon \rangle\right)^{\frac{1}{3}} \tag{1.26}$$

where $\langle \epsilon \rangle$ is the average dissipation rate of the turbulent kinetic energy (see fig. 1.16) [67]. Since r^* depends on the polymer relaxation time, it can be

[5]Effective viscosity relates, in space and time, the average deviatoric stress to the average strain.

[6]Elongational or extensional viscosity is the quotient of the difference between the longitudinal stress (σ_{11}) and the lateral stress (σ_{22}) and the elongational strain rate ($\dot{\gamma_E}$)

$$\eta_E = \frac{\sigma_{11} - \sigma_{22}}{\dot{\gamma_E}}$$

in steady uniaxial flow.

considered as a function of the type of polymer. Polymer molecules can

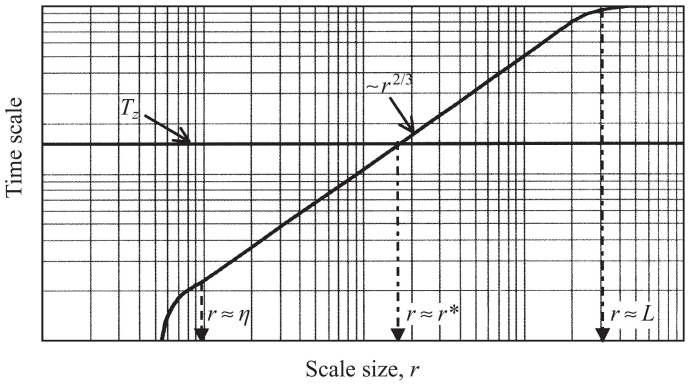

Figure 1.16: A schematic of time scales in homogeneous turbulence and the definition of the length scale r^*. The two-third power law follows from Kolmogorov's (1941) phenomenology in high-Reynolds-number turbulence. This power law is approximately valid between some multiple of the Kolmogorov scale η and a fraction of the large scale L. From Sreenivasan & White [67].

be expected to be stretched by all scales $r < r^*$. Considering now figure 1.17, the elastic theory supposes that in a certain range $r^{**} < r < r^*$, the polymers are stretched a little and so advect without producing a reciprocal effect on the flow: while flow scales smaller than r^* do have an effect on the polymer, all flow scales larger than r^{**} remain unaffected by the polymer. The scale r^{**} is determined by the criterion that the elastic energy stored by the polymer molecules (per unit volume) equals the turbulent energy (per unit volume) at that scale. Turbulent scales finer than r^{**} are strongly affected by the elastic forces with the consequence of obstructing the usual Kolmogorov-type energy cascade.

To proceed with the analysis of the elastic theory we now have to understand *i)* the amount by which the polymer molecule is stretched at any given time scale $r < r^*$ and *ii)* the manner by which the elastic stress depends on the amount of stretching. For the first, the theory suppose that the stretching at any scales follows the power law

$$\lambda(r) = \left(\frac{r^*}{r}\right)^n \tag{1.27}$$

with n depending on the dimensionality of stretching (1 in two dimensions, 2 in three dimensions). Regarding the second point, de Gennes (1990) [12] argued that the elastic energy varies with $\lambda(r)$ as

$$G\,[\lambda(r)]^{\frac{5}{2}} \tag{1.28}$$

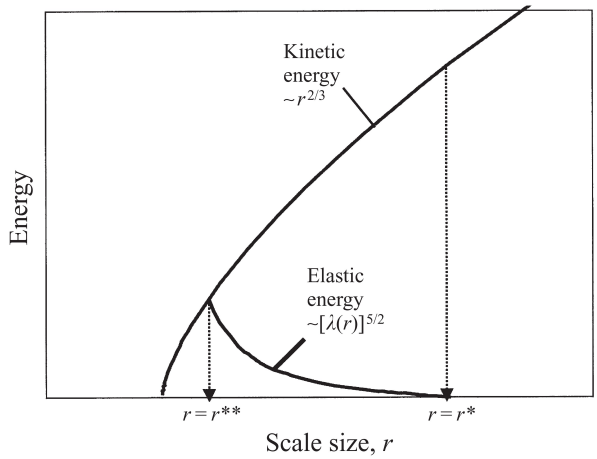

Figure 1.17: A schematic of the turbulent energy (per unit volume) scales, according to the Kolmogorov phenomenology, as $r^{2/3}$ (upper line), while the elastic energy (per unit volume) begins to grow at r^* according to $[\lambda(r)]^{5/2}$ (lower line). The scale at which the two quantities are equal defines r^{**}. The line representing the elastic energy has not been continued below r^{**} because the behaviour in this region is not understood. From Sreenivasan & White [67].

where $G = ckT/N$, c being the concentration of the polymer. It follows that

$$G\left[\lambda(r)\right]^{\frac{5}{2}} = \rho u_{r^{**}}^2 \tag{1.29}$$

the quantity on the right-hand side being the kinetic energy of turbulence at scale r^{**}.

Contrary to the viscous theory, in this case equation (1.29) prescribes the dependence of r^{**} on polymer concentration. For very small concentrations the scale r^{**} will be smaller than η and so the polymer will have no effect on turbulence. There exist a minimum concentration for which $r^{**} = \eta$, at which the polymer's effects will begin just to be felt. This corresponds to the onset of drag reduction. So equation (1.29) not only includes the molecular properties of the polymer but also provides explicit prediction of the threshold concentration in terms of polymer-flow combination. r^{**} is hence a function of the polymer type and its concentration.

If we now adapt this theory to a pipe flow, first of all we can consider that the scales r^* and r^{**} will be functions of the radial position in the pipe; this condition arises through the radial variation of the energy dissipation $\langle\epsilon\rangle$. The radial variations of r^* and r^{**} can be calculated, from equations (1.25), (1.26), (1.27) and (1.29); refer to [67] for details. Figure 1.18 depicts the overall behaviours of r^* and r^{**} as a function of the radial distance from the wall. The polymer action is different for different radial positions. Lets

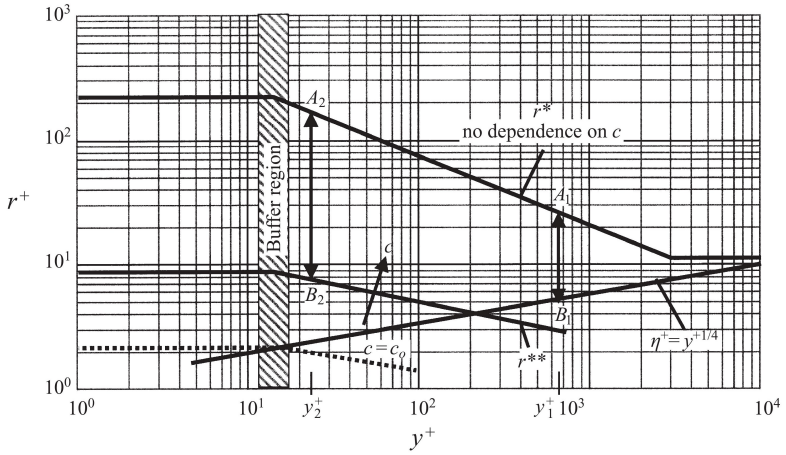

Figure 1.18: A schematic of the variation of length the scales r^* and r^{**} in a pipe flow. Also shown is the Kolmogorov scale. All scales are normalized by the wall variables u_τ and ν. The dotted line for $c = c_0$ corresponds to the onset of drag reduction. From Sreenivasan & White [67].

consider the behaviours at radial position y_1 and y_2. At y_1 the polymer molecules are stretched between the scales marked A_1 and B_1; even if the stretching continues up to the Kolmogorov scale, the stored elastic energy remains smaller than the turbulent energy at any flow scale so the polymer will have no effect on the flow (refer to fig. 1.17). At y_2 the stretching occurs between A_2 and B_2 (which means scale r^{**} at y_2); at this radial position the elastic energy equals the turbulent energy and all scales at y_2 smaller than B_2 (smaller than r^{**}) will be affected by the polymer. The intersection point of the lines η^+ and r^{**+} identifies a value of y^+_{lim}; in the area enclosed by these two lines, at values of $y^+ < y^+_{lim}$ the polymer can absorb elastic energy before viscous dissipation at Kolmogorv scale occurs.

As mentioned above, the viscous sublayer plays an irrelevant role in the drag reduction phenomenon; the main effects are felt within the buffer layer: polymers are most effective when they reach this region. For very low concentrations of the polymer, the intersection between the Kolmogorov's η^+ line and the r^{**+} line occurs below the buffer region (see fig. 1.18): the polymer has non effect on any part of the flow. At minimum concentration c_0 the intersection point occurs within the buffer region, this corresponds to the *onset* of drag reduction.

Consequence of the polymer action is a thickened buffer layer and consequently, drag reduction. As already stated this approach includes also the polymer concentration in its onset criterion since the cumulative elastic energy of the polymers is a function of the concentration. This theory was numerically verified. Opposite to the viscous effect, this mechanism could

be considered as an energetic approach.

Both theories are strictly related to polymer stretch and coil transition which has been investigated by many authors [62, 65, 66]. A polymer in elongational flow begin to deform when the force due to the hydrodynamic friction across the molecule exceeds the entropic elasticity that tends to coil it. As mentioned above, two time scales can be defined: first, the polymer relaxation time, second the time scale, $1/\dot{\epsilon}$, which is set by the strain rate ($\dot{\epsilon} = d\epsilon/dt$) of the applied flow. Where the strain rate is due to the velocity gradient $\partial u_y/\partial y = \dot{\epsilon}$ along the y direction of the flow. Polymer stretching is not a steady state condition: large fluctuations in the extension due to an end-over-end tumbling of the molecule have been observed in some simulations and experiments. These fluctuations presumably occur because the stretched state is destabilized by the rotational component of the shear flow [62]. Even at low *We* numbers there are large fluctuations in the extension of the molecule; as *We* is increased, the molecule fluctuates more rapidly and reaches larger extensions. The amount of extension increases as *We* is increased because the velocity gradient and hence the hydrodynamic forces acting across the molecule, increase. Fluorescence microscopy on DNA molecules revealed that individual polymers never reach a steady state extension in shear flow because they continually undergo end-over-end tumbling motion [62]. Therefore, polymer extension may undergo a variety of stretching and coiling events that may have a broad distribution of time scales. In figure 1.19 a descriptive cycle for the motion of polymers in strong shear flow is presented. Cycle begins where polymer orientation angle θ_1 is positive. At this stage, ${\delta_2}^7$ is generally larger than equilibrium values which implies a substantial velocity gradient across the molecule, leading to polymer stretching. After the stretch phase, the orientation angle is small but positive ($\theta_2 > 0$). A polymer may now align in the flow direction such that $\theta_3 \approx 0$, leading to small differences in fluid velocity across the molecule and hence small hydrodynamic forces exerted on the chain. A Brownian fluctuation causes the polymer orientation angle to become negative ($\theta_4 > 0$) and leads to polymer collapse ($\theta_5 << 0$). Finally, the polymer tumbles, θ changes sign from negative to positive and the cycle begins again.

Before concluding with a more detailed analysis of the interaction of turbulence and polymers and turbulence attenuation, another important behaviour of the polymer suspensions must be underlined: the maximum drag reduction asymptote. The mathematical definition of this phenomenon is given in section 1.2 by Eq. (1.21), thus its physical behaviour will be here described. With reference to figure 1.20, the onset of drag reduction can be determined as the point of departure from the von Kármán law. After the onset, for a given *Re*, drag reduction increases with polymer concentration but saturates beyond a certain value (dashed line in fig. 1.20).

[7] δ_2: gradient-direction polymer thickness; a microscopic quantity directly related to bulk shear viscosity [62].

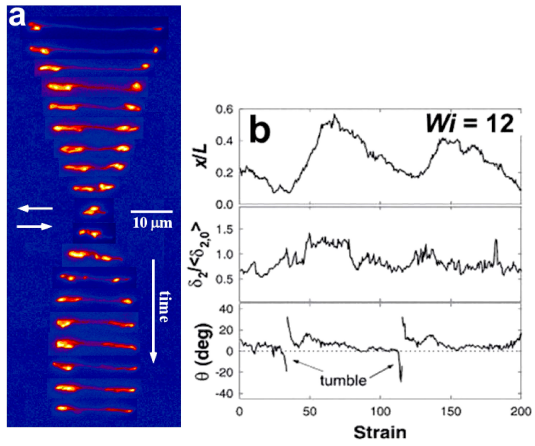

(a)

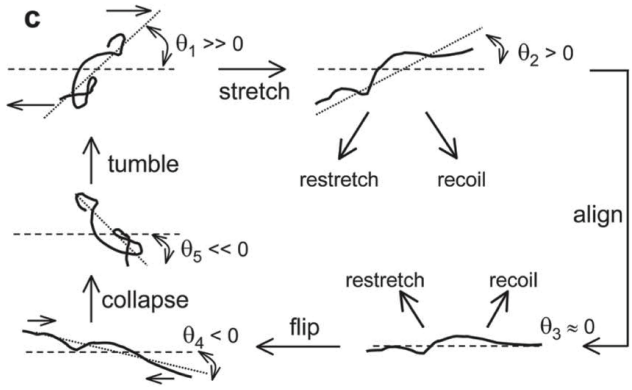

(b)

Figure 1.19: Dynamics of DNA in steady, unbound shear flow. (a) Time sequence of images of fluorescent DNA ($L = 80\mu m$) at $We = 109$ in shear flow clearly illustrating end-over-end tumbling motion. Time between image is $\approx 10s$. (b) Trajectories of fractional polymer extension x/L, gradient direction thickness δ_2 and polymer orientation angle θ for lambda DNA at $We = 12$. (c) Descriptive cycle of periodic polymer motion in shear flow. From Schroeder *et al.* [62].

The upper bound of drag reduction is the so-called Virk's asymptote (see section 1.2). Similarly, for a given polymer concentration, with increasing *Re*, the drag reduction increases along a unique trajectory, that depends on the concentration (so-called slope increase [74]) but abruptly changes trajectory at a certain *Re* (dotted line in fig. 1.20). The change in trajectory indicates the merge of the drag-reduction curve with MDR asymptote. The explanation of this unique bounding mechanism is still largely empirical. Two possible explanations are the following: *(a)* MDR occurs when the effects of polymers are felt over all flow scales, causing the buffer layer thickness to extend across the entire boundary layer (Sreenivasan & White, 2000 [68]; Virk, 1975 [74]); *(b)* MDR occurs when the Reynolds stresses are strongly diminished and the mechanisms that sustain turbulence are primarily driven by the fluctuating polymer stresses (Ptasinski *et al.* [56]).

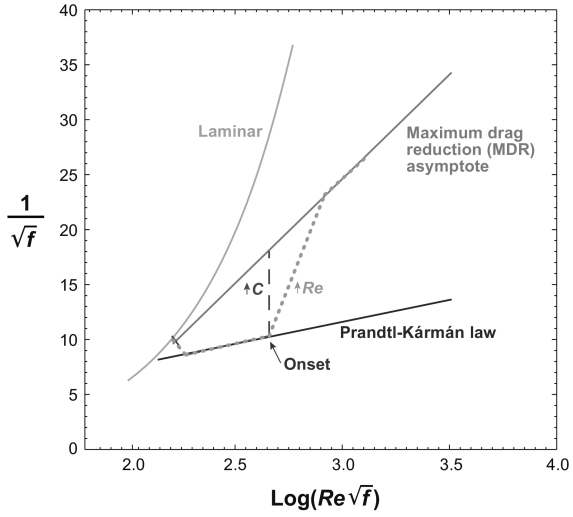

Figure 1.20: Schematic illustrating onset and different trajectories of polymer drag reduction. From White & Mungal [77].

To conclude this section, an analysis of the interaction between polymers and near-wall structures will be outlined. The prevalent structure of wall-bounded turbulent shear flows are stream-wise velocity streaks and quasi-streamwise vortices. In the self sustaining cycle of wall turbulence, quasi-stream-wise vortices extract energy from the mean flow and create streamwise streaks; in turn, an instability of the streaks gives rise to the quasi-streamwise vortices (see fig. 1.21). A fundamental principle of the drag reduction phenomenon is to disrupt the turbulence regeneration cycle. The polymers added to the solvent will interact with the near-wall turbulent structures reducing the strength and the number of the quasi-streamwise vortices and stabilizing and thickening, the stream-wise velocity streaks (see fig. 1.22).

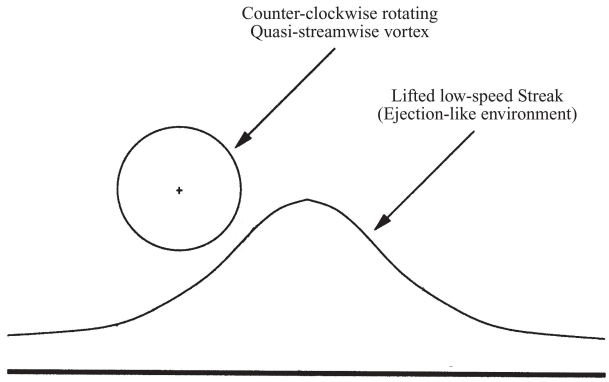

Figure 1.21: Near-wall structures: low speed streak and quasi-streamwise vortices. From Marchioli [49].

The stabilization of the velocity streaks will lead to a weakening of the

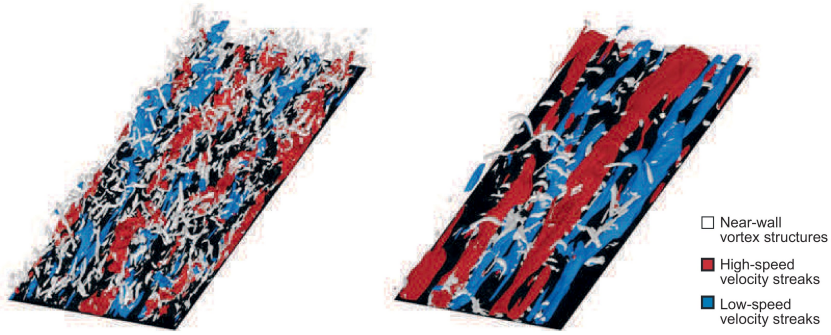

Figure 1.22: Instantaneous visualizations of the velocity gradient tensor, high-speed velocity streaks and low-speed velocity streaks for (*left*) Newtonian fluid and drag reduction of 60% (*right*). Flow is from bottom left to top right. From White & Mungal [77].

quasi-streamwise vortices and to a consequent damping of the wall-normal fluctuations.

Numerical simulations investigating the interactions between polymer and the near-wall turbulent structures show that: *(a)* polymers are stretched primarily in the near-wall region of the flow and *(b)* polymer directly interact with and damp, the quasi-streamwise vortices. This interaction leads to the weakening of the vortices due to the polymer body force which opposes the motion of the vortices (see Dubief *et al.*, 2005 [14]) and in turn polymer stress work transfers energy from the vortices to the polymers. Polymer work is a component of the Reynolds stress equation and represents the

relation between polymers and turbulence structure. Polymer work E_α is defined as the product of the velocity and polymer body force and can dampen ($E_\alpha < 0$) or enhance ($E_\alpha > 0$) the energy carried by velocity fluctuations. The extraction of energy from near-wall vortices by polymers occurs as polymers are pulled around the vortices, either by upwash or downwash flows; due to this mechanism polymers experience significant straining around vortices, leading to large stretching. In figure 1.23 the interaction between polymers and near-wall turbulent structures is depicted; in figure 1.23a it could be seen the work done by the vortices on the polymers, in the buffer layer ($E_\alpha < 0$), dampening the wall-normal fluctuation, and the work released by the polymer to the streamwise streaks enhancing the stream-wise turbulent energy ($E_x > 0$).

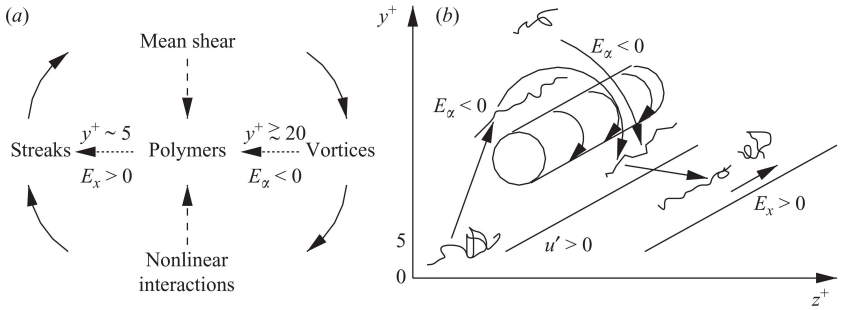

Figure 1.23: (a) Sketch of the cycle of wall turbulence regeneration with energy transfer from the polymers to the flow and vice versa, ····· denotes the action of polymers on turbulence, − − − the main action of stretching. (b) Vortex pumping fluid from the near-wall region and creating turbulence-damping polymer work and re-injecting stretched polymers into near-wall region, thereby generating turbulence-enhancing polymer work. From Dubief [15].

1.2.2 Polymer mechanical degradation

In the previous section we have seen that an upper bound is expected for drag reduction, being the maximum drag reduction asymptote. According to Virk [74], to reach the MDR condition, it is sufficient to keep increasing the polymer concentration. If we consider the practical application of polymer drag reduction, two main limitations to this assumption arise: *i)* cost considerations and *ii)* high molecular weight polymers undergo chain scission at the high Reynolds numbers characteristic of practical turbulent flows. The latter implies that the capability of the polymer chains to reduce drag is lowered and therefore limits the amount of drag reduction that can be achieved. High molecular weight polymers are the most effective in reducing drag but are more easily subject to chain break, typically at its midpoint

(polymer drag degradation has been reported by different authors: refer to Sung *et al.*, 2004 [69], Vanapalli *et al.*, 2005 [72] and Elbing *et al.*, 2009 [17] among others).

Two main conditions influence polymer degradation: entrance effects and turbulent intensity of the flow. Vanapalli *et al.* in 2005 [72] performed experiments to assess both the aforementioned effects. Figure 1.24 depicts how the %DR (percent drag reduction) diminishes as a consequence of the polymer chain breakage which reduces the initial value of the molecular weight (see fig. 1.25). It can be noticed that after a certain number of passages, the molecular weight reaches a steady state value: all the chains susceptible to breakage have undergone scission, no further changes in the molar mass distribution occur and the friction drag behaviour attains a steady state value (see fig. 1.26).

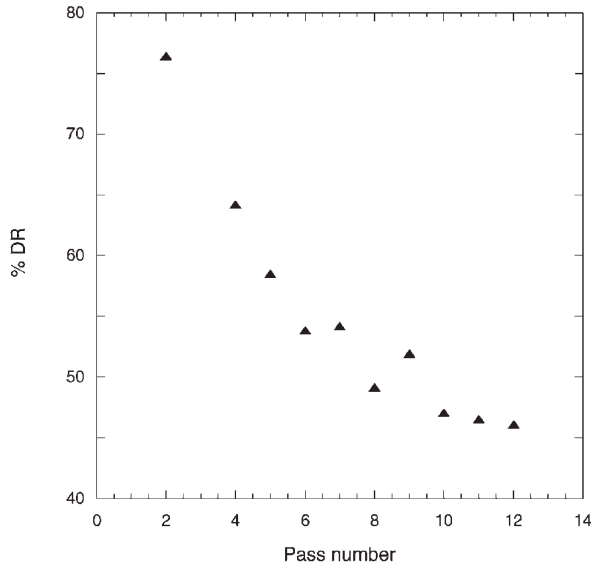

Figure 1.24: Change in %DR for a 100 ppm PEO solution as a function of the number of passes through a 3 m long pipe, 10.9 mm ID. From Vanapalli *et al.* [72].

Entrance effects are almost always present in practical application, for example the polymer injection in a pipe flow can already represent a site of degradation. Vanapalli *et al.* showed that entrance effects play a major role in polymer degradation; this implies that reasonably, polymers are already degraded before experiencing the fully developed flow, where they are expected to act as drag reducing agents.

Starting from Virk's phenomenology, they attempted to provide a theoretical tool to predict the effective bound on polymer drag reduction due to

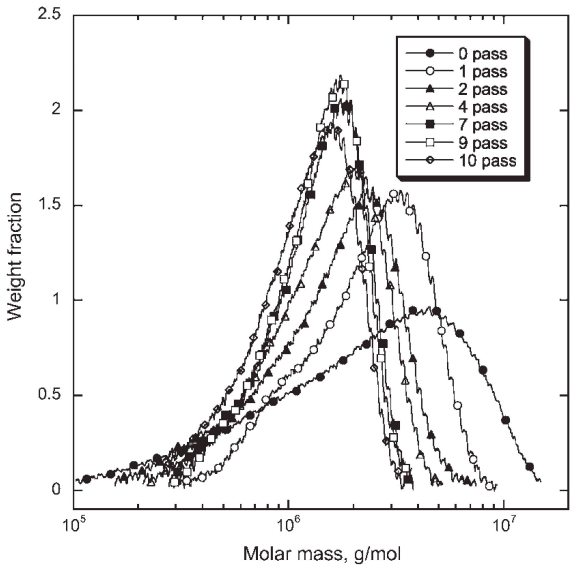

Figure 1.25: Evolution of the molar mass distribution with the number of passes (3 m pipe, 10.9 mm ID) at $Re \sim 1.2 \cdot 10^5$ and wall shear rate $\dot{\gamma} \sim 1.45 \cdot 10^5 s^{-1}$. From Vanapalli *et al.* [72].

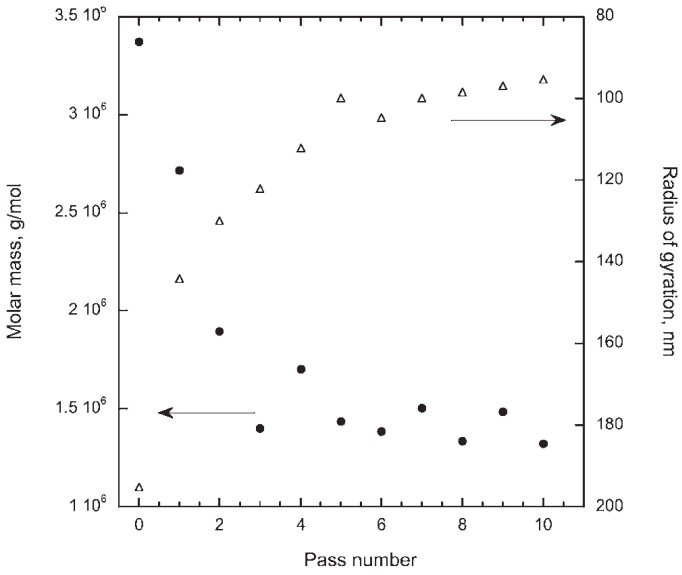

Figure 1.26: Corresponding weight-average molar mass and radius of gyration as a function of number of passes. From Vanapalli *et al.* [72].

chain scission; trying to relate the polymer characteristics (such as molecular weight and concentration) to the flow conditions. As previously mentioned, for drag reduction to begin, a specific onset shear rate is needed; this can be expressed, as a function of the molecular weight as

$$\dot{\gamma}_w^* = 3.35 \cdot 10^9 M_w^{-1} \tag{1.30}$$

Where * identifies the onset condition. Beyond this value of the shear rate, the friction factor decreases with increasing Reynolds number; this condition can be expressed as

$$\frac{1}{\sqrt{f}} = (4.0 + \delta) \log_{10} \left(Re\sqrt{f} \right) - 0.4 - \delta \log_{10} \left[\left(Re\sqrt{f} \right)^* \right] \tag{1.31}$$

Where $\left(Re\sqrt{f} \right)^* = \sqrt{2} Re_\tau^*$ and δ is the slope increment which can be express as a function of the polymer concentration and molecular weight

$$\delta = 1.242 \cdot 10^{-6} c^{0.5} M_w \tag{1.32}$$

In figure 1.27 the scission bounds are shown together with three other curves

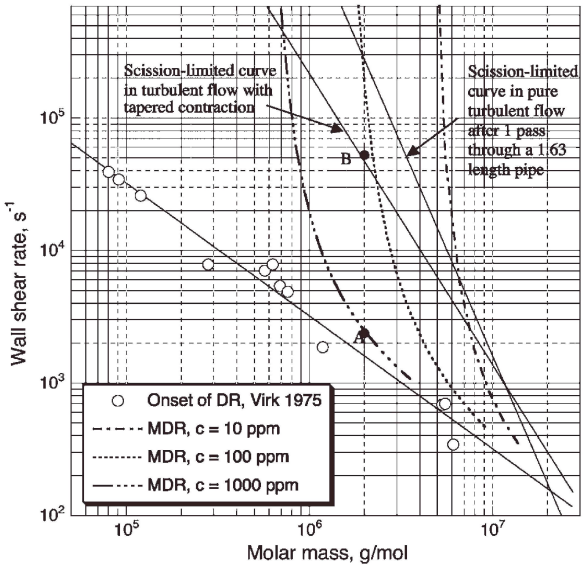

Figure 1.27: Bounds on polymer drag reduction for PEO due to chain scission on a wall shear rate basis. From Vanapalli *et al.* [72].

representing the locus of intersection of the polymeric regime and the MDR asymptote for a given polymer concentration and pipe diameter (in this case 10.9 mm). These curves were obtained solving equations (1.31) and (1.21) for different M_w and a specific polymer concentration c (see [72] for

details). What is interesting to notice is that the intersection of these curves with those of the scission bounds identifies certain regions in concentration, molar mass and wall shear rate space for which drag reduction due to PEO molecules will be ultimately limited by scission dynamics rather than MDR asymptote. For example, considering a PEO solution of $M_w = 2 \cdot 10^6 g/mol$ at 1000 ppm, this polymeric solution reaches MDR at $\dot{\gamma} \sim 2000\, s^{-1}$ (point A in fig. 1.27). But, if we consider a concentration of 100 ppm, molecules breakage will happen at $\dot{\gamma} \sim 50\,000\, s^{-1}$ before the MDR could be reached (point B): the scission curved is encountered before reaching the MDR asymptote. This represent the maximum value of drag reduction attainable for this concentration. Hence figure 1.27 gives quantitative practical limits on maximum drag reduction achievable for a given polymer, taking into account the polymer parameters (molecular weight and concentration) and the operating conditions (pipe diameter, *Re* and wall shear rates). In figure 1.28a the scission curves are drawn for a 10 ppm PEO solution along with the expected slope increment for different molecular weights: at this concentration and for the depicted range of M_w the MDR is never reached, chain breakage represents the ultimate upper limit for drag reduction. As the molecular weight increases, the onset value of the friction Reynolds number decreases. The proposed theory have been verified comparing the theoretical predictions with experimental results and good agreement has been found (see fig. 1.28b).

This theory represents an interesting possibility for the drag reduction prediction in industrial applications since it is feasible to easily adapt it to the specific polymer characteristics and operational conditions. The knowledge of the effective upper bound is a fundamental information for the correct choice of the polymer type and concentration, related to the particular application.

1.2.3 Drag reduction prediction

In this section a brief introduction to the drag reduction prediction will be given. Some efforts have been done in the recent years to develop practical tools to predict the drag reduction efficiency as a function of several parameters such as polymer characteristics, flow regime and pipe diameter among others. Starting from DNS simulations, Housiadas & Beris (2013) [31], developed an approximate relation for the skin friction coefficient for visco-elastic turbulent flows.

First of all they introduce a new parameter called *zero shear-rate elasticity*

$$El_0 = \frac{\lambda \nu_0}{h^2} = \frac{We_{\tau 0}}{Re_{\tau 0}^2} = \frac{1}{\mu_w} \frac{We_\tau}{Re_\tau^2} \tag{1.33}$$

which can be considered as a dimensionless relaxation time characterizing the memory effects of the material; it can be considered as a property of the chosen polymer type and pipe geometry. In principle an estimate of

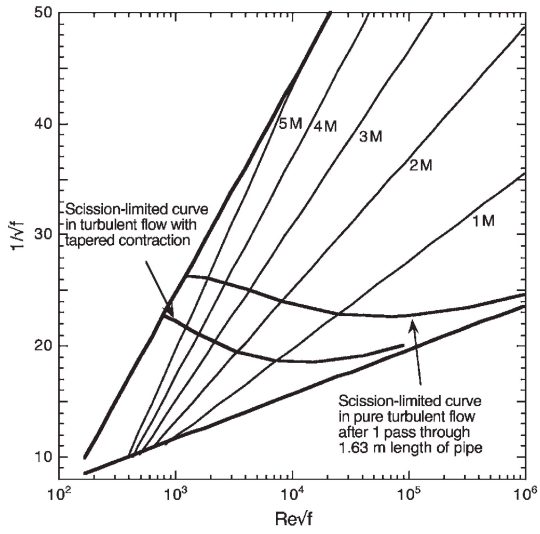

(a)

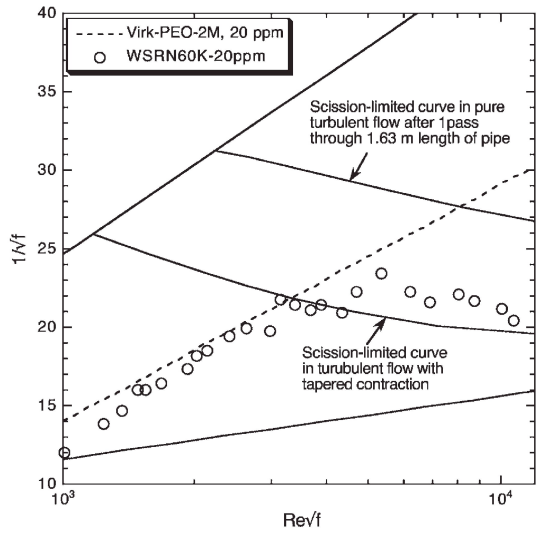

(b)

Figure 1.28: (a) Bounds on polymer drag reduction for PEO due to chain scission on a Prandtl-Kármán plot. The scission curves are drawn for c=10 ppm. The unit M denotes $1 \cdot 10^6 g/mol$. (b) Exprimental verification of the bounds on PEO drag reduction due to chain scission. Hollow circles represent friction data collected for 20 ppm of WSR-N60K ($M_w \sim 2 \cdot 10^6 g/mol$). The dotted line represents the estimated slope increment. From Vanapalli *et al.* [72].

this parameter requires an evaluation of the polymer relaxation time but, as will be explained later on, this procedure can be avoided by knowing the onset We number. In equation (1.33) λ is the polymer relaxation time, ν_0 is the kinematic viscosity at zero shear-rate and h is half channel height (pipe radius in pipe flows). The viscosity at the wall can be approximate with the zero shear-rate viscosity when no significant shear-thinning effects are expected. The advantage of using the elasticity parameter, instead of the We number, is that it does not involve the flow velocity and so it is a material parameter.

To take into account for the polymer concentration, they chose the *limiting drag reduction (LDR)* parameter which is the asymptotic value of %DR at high We numbers (see fig. 1.29). This parameter is used to scale

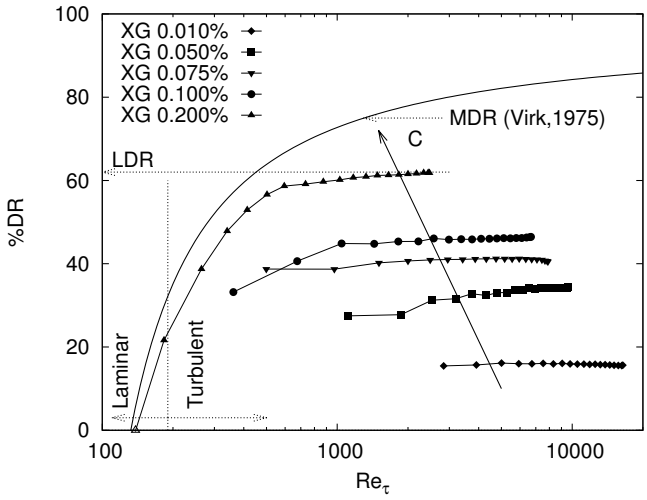

Figure 1.29: Percent drag reduction for aqueous solutions at different XG concentrations as a function of friction Reynolds number. Adapted from Campolo *et al.* [4].

the DR results as shown in figure 1.30 where the fitting has been done as

$$\frac{DR}{LDR} = \begin{cases} 0, & We_\tau < We_\tau^{(onset)} \\ 1 - \frac{2}{1+exp\left(\frac{We_\tau - We_\tau^{(onset)}}{\Delta We_\tau}\right)}, & We_\tau \geqslant We_\tau^{(onset)} \end{cases} \tag{1.34}$$

there $We_\tau^{(onset)}$ represents the Weissemberg number for the onset of drag reduction; from the fitting of their DNS results, they propose that: $We_\tau^{(onset)} \approx 6$ and $\Delta We_\tau \approx 25$. Assuming this value for the onset We number allows to calculate the polymer relaxation time from equation (1.33).

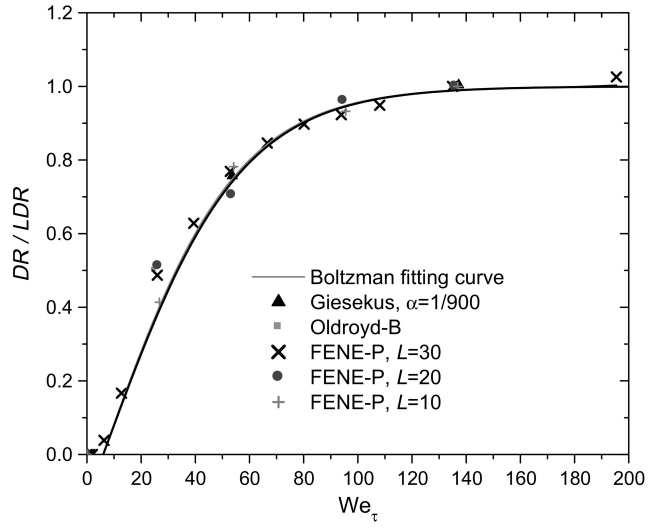

Figure 1.30: The universal fitting curve fort the ratio of drag reduction together with the results obtained by DNS of visco-elastic turbulent channel flow. From Housiadas & Beris [31].

Once the El_0 and LDR parameters are known, assuming the onset We number equal to 6, one can follow the procedure explained in [31] and obtain the values of $Re\sqrt{f}; 1/\sqrt{f}$. The result is the possibility to predict the behaviour of drag reduction given the polymer characteristics and the operating conditions. For example, in figure 1.31 (where $C_f \equiv f$) the effect of the limiting drag reduction and so the polymer concentration, is examined keeping constant the elasticity (polymer type). The interesting potential is to perform experiments in small laboratory-scale facilities and then use the model to predict the drag reduction behaviour in industrial applications; for example for the same polymer and concentration, and varying the pipe diameter to assess DR efficiency in larger pipes. Another possibility is to keep constant the pipe diameter and polymer type and change the polymer concentration to verify the more convenient operational condition.

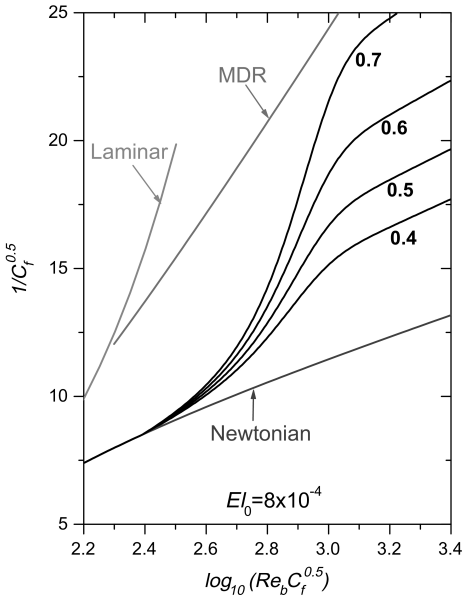

Figure 1.31: The effect of the limiting drag reduction parameter, LDR in Prandtl-von Kármán plot for pipe flow. Results are shown for LDR=0.4, 0.5, 0.6 and 0.7. $C_f \equiv f$. From Housiadas & Beris [31].

1.3 State of the art in fibres drag reduction

1.3.1 Fibre suspension flow

A fibre suspended in a flow interacts with all other fibres within approximately one fibre length L of its centre. The spherical volume circumscribing a fibre scales like nL^3, where n is the number of fibres per unit volume and is referred to as the *interaction volume*, because fibres within this volume interact hydrodynamically. With respect to this parameter and the volume fraction of fibres material $\phi = nV_f$, with $V_f \sim Ld^2$ (d fibre diameter)[8], the fibre suspension flows may be divided into three categories: dilute suspension, semi-dilute suspension and concentrated suspension (Batchelor, 1971 [2]; Koch & Shaqfeh, 1990 [45]). The addition of fibres (rod-shape particles) in different concentrations leads to different effect on the viscosity and flow behaviour of the suspending fluid.

The limit of dilute suspension is $nL^3 \ll 1$: in this case, particles are sufficiently far apart from each other so the relative motion of the fluid near one particle in unaffected by the presence of the others. In the regime $nL^3 \gg 1 \,\&\, \phi \ll 1$ a semi dilute suspension exists: in this regime the distance between fibres h is $R \ll h \ll L$ so the fibres are not free to rotate end-over-end and they interact with each other. Regarding the concentrated suspension no strict definition is proposed; anyway, for this category, it is generally believed that $\phi > 0.1$.

Beside the characterization of the suspensions, categories of particle concentration may be defined: low particle concentration, intermediate particle concentration and concentrated particle concentration. The upper limit for low particle concentration is defined as

$$\phi r^2 < 1.5 \tag{1.35}$$

where ϕ is the volume concentration of the particle and $r = L/d$ is the particle aspect ratio. Defining the number of particle per unit volume as

$$n = \frac{\phi}{\left(\frac{\pi}{4}\right) Ld^2} \tag{1.36}$$

equation (1.35) can be expressed as

$$\frac{\pi}{4}\left(nL^3\right) < 1.5 \tag{1.37}$$

Equation (1.35) represents the condition at which particle collisions are negligible. Above this limit, a sharp increase in the effective viscosity occurs while, at lower concentrations, the suspension exhibit a Newtonian increase

[8] For cylindrical fibres $V_f = \frac{\pi d^2}{4} L$ so $\phi = \frac{\pi}{4} n d^2 L = \frac{\pi}{4} n \frac{L^3}{r^2}$ where $r = L/d$ is the fibre aspect ratio.

in viscosity. For the intermediate particle concentration, an upper limit could be established as

$$\frac{\phi r}{3(\ln(2r) - 1.80)} \approx 0.18 \tag{1.38}$$

and

$$\ln(2r) \gg 1.80 \tag{1.39}$$

Beyond this limit, the suspension viscosity increases considerably to a value corresponding to the category of large particle concentration. In table 1.1 a summary of these conditions is presented.

Dilute/low particle concentration	Semi-dilute/intermediate particle concentration	Concentrated/large particle concentration
$nL^3 \ll 1$	$nL^3 \gg 1$ and $\phi \ll 1$	$\phi \geq 0.1$
$\frac{\pi}{4}\left(nL^3\right) < 1.5$	$\frac{\phi r}{3(\ln(2r)-1.80)} \approx 0.18$ and $\ln(2r) \gg 1.80$	$\frac{\phi r}{3(\ln(2r)-1.80)} > 0.18$

Table 1.1: Fibre concentration ranges for different categories of fibre suspensions. From Xu [80].

1.3.2 Rheological properties of fibre suspension

Rheological properties of suspensions in extensional flows are of significance in the turbulent drag reduction process. Batchelor in 1971 [2] found that, the suspension of straight elongated rigid particles has the property that, when subject to steady pure straining motion, all the particles take up the orientation in which they individually make their greatest contribution to the bulk stress. If the suspension is dilute, each particle of length L makes contribution, to the bulk stress, which is roughly the same order as that due to a rigid sphere of radius $l = L/2$.

The addition of particles to the suspension will affect the velocity profile and the turbulence intensity of suspension flow. Experiments confirmed that the streamwise particle mean velocity profile is flatter than the corresponding fluid velocity profile, with particles leading the flow near the wall and lagging the flow in the core. Moreover, particles have been found both to raise and to lower the pressure drop, and there are no reliable means of predicting either the direction or the magnitude of the change based on particle and flow properties. Gore & Crowe (1991) [28] showed that whether given particles increase or decrease turbulence intensity depends on the ratio of particle diameter to a characteristic eddy diameter of turbulence. Also for

fibre suspension flows attenuation in the turbulence has been reported; the attenuation increases with particle Stokes number, particle mass loading and distance from the wall.

1.3.3 Regimes of fibre suspension flow

In 1958, Daily & Bugliarello [9] performed an extensive experimental campaign obtaining a large amount of friction factor-Reynolds number correlations, both for synthetic and wood fibres. As shown in figure 1.32, three main regimes can be highlight (see Robertson & Mason, 1967 [59]) *plug flow*, *mixed flow* and *turbulent flow*. In plug flow a plug region exists in which

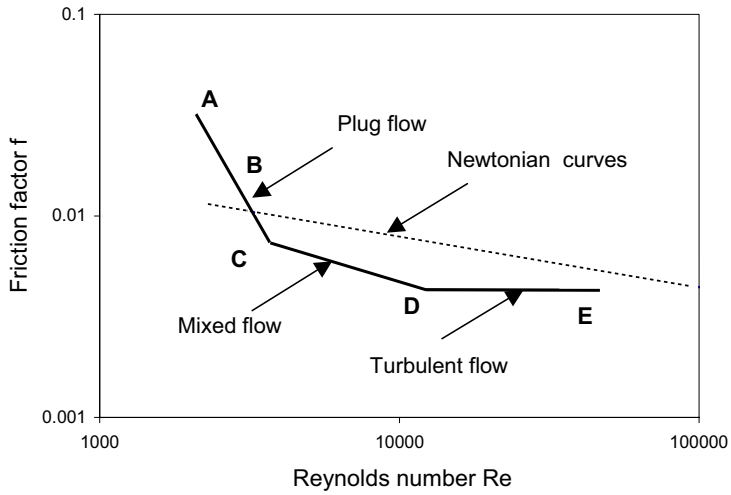

Figure 1.32: Schematic representation of friction loss curve with fibre suspension flow. From Robertson & Mason [59].

the core is composed by a coherent fibre network. There is no movement of fibres relative to one another within the networks and the velocity gradient is confined to fibre-free solvent annulus near the wall. The thickness of this annulus increases with flow rate and varies with fibre properties and concentrations. In this regime, pressure losses in pipe flow are grater than that of the solvent alone. In mixed flow, after the transition point C in figure 1.32, the flow in the solvent annulus becomes unstable and an increasingly turbulent pure solvent layer forms around the plug. Further increases in flow rate produce turbulent stresses which cause the progressive disintegration of the plug until it disappears at point D. The pressure loss becomes less than that of the solvent alone. After the transition point D, the flow becomes turbulent across the entire cross section and the friction factor is practically constant over a broad range of Reynolds number. Several

experiments showed that, the higher the coherence of a fibre network the grater the suppression of the turbulence and hence the lower the friction factor.

Lee & Duffy (1976) [46] suggested that a significant portion of the momentum transfer in turbulent fibre suspension is the result of radial movement of fibre flocs. Shear in turbulent fibre suspensions is restricted to a small volume of solvent between adjacent flocs. Consequently, the relative velocity between adjacent eddies is less than that of the pure solvent. Moreover, the possibility of direct contact between flocs will further restrict relative motion. It is possible to state that fibre networks can transmit forces from one point to another within their structures and can enhance momentum transfer by providing a solid link between adjacent fluid layers. Concluding, fibre flocs affect momentum transfer in two ways: they tend to lower it by damping the turbulence of the suspending phase and also tend to enhance the momentum transfer by providing a solid link between adjacent fluid layers.

Gore [28] discovered that a critical parameter is the ratio of equivalent particle diameter to a turbulent length scale d_p/l_c. The length scale is the integral length scale or the characteristic length of the most energetic eddy, when only one phase is present. The critical demarcation value of $d_p/l_c \approx 0.1$ caused the turbulent intensity of the carried phase to either increase or decrease with the addition of particles. For values grater than 0.1 the addition of particles caused an increase in the carrier-phase turbulent intensity. Moreover, at low Reynolds number the streamwise fluctuation decreases, with respect to the pure solvent turbulent flow, while the tangential component is increased. Conversely, at high Reynolds number, the streamwise fluctuation was found to be increased.

1.3.4 Drag reduction mechanism

It has been verified that the addition of fibres to a turbulent flow produces a reduction of the longitudinal pressure gradient with respect to the solvent alone at the same flow rate. The effectiveness of fibres as drag-reducers increases as their aspect ratio increases; in particular, Radin & Patterson (1975) [58], established that drag reduction could always be obtained with fibrous additives having aspect ratios of about 30. Vaseleski & Metzner (1974) [73] reported that, for fibre suspensions in pipe flows, the presence of fibres in the turbulent core region is a key point to obtain drag reduction.

Lee & Duffy (1976) [46] proposed a mechanism to explain the drag reduction process in mixed flow regime; with respect to figure 1.33 they outlined the following behaviour of the suspension friction curve: mixed flow begins at bulk velocities lower than point A. Drag reduction reaches a maximum in B. In the regime between B and C, friction factor value is approximately independent on the bulk velocity and the curve of the suspension approaches the solvent one. After point C, the friction factor

decreases as bulk velocity is increased. The difference between the curves of the pure solvent and the suspension increases as the fibres concentration is increased. The mechanism they proposed is based on the assumption that, at

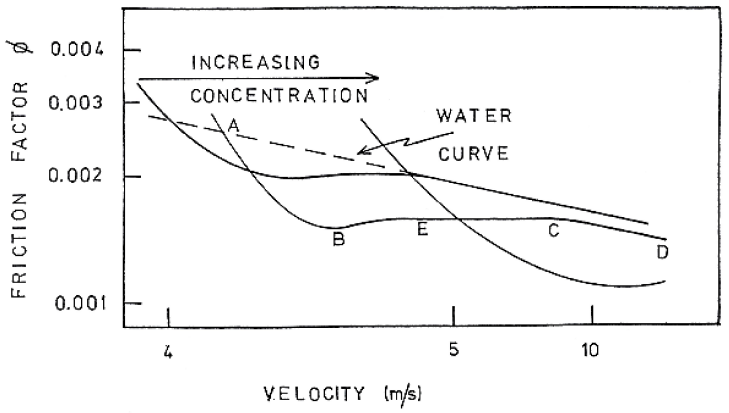

Figure 1.33: Curves of friction factor versus velocity for wood fibres suspensions. From Lee & Duffy [46].

any flow rate, there is a state of equilibrium in which both the formation and the disruption of flocs are occurring simultaneously [59]. Moreover, there is a distribution of floc size from the surface of the plug to the region near the wall. As mentioned before, fibres and flocs affect the momentum transfer in two different ways; at low intensities of turbulence, the predominant effect in momentum transfer in the turbulent fibre-solvent annulus, is due to the large flocs providing a solid link between adjacent water layers. In these conditions, increasing the intensity of turbulence by means of increasing the flow rate, decreases the average floc size in the turbulent annulus; this will lead to a decrease in the momentum transfer with a consequent increasing of mean velocity gradients and a rise in drag reduction. At regimes higher than the maximum drag reduction regime, the average floc size is sufficiently small that they may interact with the smaller turbulent scales, suppressing radial turbulence. Hence, the decrease in floc size along with an increase in flow rate, yield to a decreasing drag reduction. The magnitude of maximum drag reduction is expected to be a function of the fibre and suspension properties.

More recently, Xu (2003) [80], distinguished five types of fibres suspension regimes with respect to the local distribution of the dispersed phase inside the pipe (see fig. 1.34). The results obtained by Xu [80] investigating the effects of the Reynolds number and the fibre concentration, show that apart from really high Reynolds numbers, as Re decreases, the turbulence intensity increases while it is reduced if the concentration grows. Paschkewitz *et al.* [53] in 2004 proposed a different mechanism for the drag reduction process, similar to that of polymer additives: fibres interact with vortex

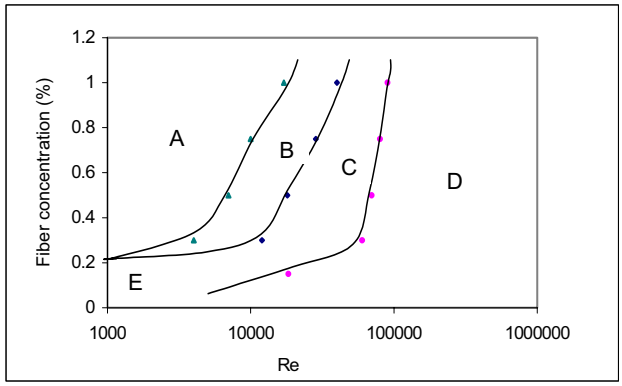

Figure 1.34: Different regimes of fibre suspension flow. (A) Plug flow + mixed flow; (B) Fibre-floc enhanced turbulent flow; (C) Fibre-floc damped turbulent flow; (D) Newtonian turbulent flow; (E) Laminar flow. From Xu [80].

structures and weaken them by means of their induced stress. After that, fibres are re-oriented in the flow direction and a reduction in the local fibre stress allows the vortex to re-emerge and turbulence is sustained in a weakened state (see fig. 1.35). Also this mechanism, as seen in section 1.2.1, can be presented as energetic since it alters the energy balance of the fibre suspension. From Paschkewitz *et al.* [53] numerical simulations, the following values of drag reduction emerge (see tables 1.2 and 1.3).

nL^3	μ_{eff}	Re_{eff}	Drag reduction [%]
5	1.01	7425	7.4
9	1.03	4301	13.2
18	1.06	7100	18.5
36	1.12	6707	26.2

Table 1.2: Effect of concentration on drag reduction. $Pe = 1000$ and $r = 100$. From Paschkewitz *et al.* [53].

In table 1.2 μ_{eff} is the effective viscosity at the wall and Re_{eff} the Reynolds number.

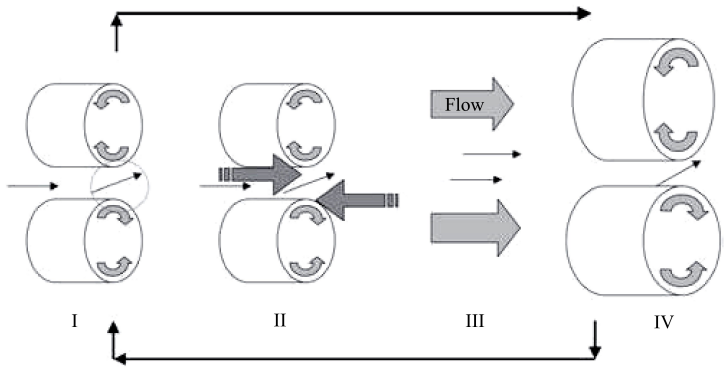

Figure 1.35: Schematic of mechanism for fibre-induced drag reduction. I. Fibres align in inter-vortex regions. II. Fibres generate large stresses and body forces that oppose vortex motion. III. Vortex structures are dissipated and fibres realign in flow direction. IV. Vortex structures re-emerge and cycle repeats. From Paschkewitz *et al.* [53].

r	ϕ	μ_{eff}	Re_{eff}	Drag reduction [%]
30	0.08	1.34	5597	10.8
50	0.03	1.15	6521	11.7
75	0.0135	1.08	6944	15.1
100	0.0075	1.06	7100	18.5

Table 1.3: Effect of fibre aspect ratio on drag reduction. $nL^3 = 18$ and $Pe = 1000$. From Paschkewitz *et al.* [53].

1.4 Polymer/fibres comparison

To conclude this chapter, an outline of the differences reported between polymer an fibres can be presented:

- fibre reduce drag primarily by opposing extensional motions in the inter-vortex regions while polymers act in these regions as well as around vortices. As drag reduction level is increased these extensional regions become weaker and rare, ultimately limiting the effectiveness of the fibre additives [53];
- the dynamics of rod-like polymers (fibres) and flexible polymers are different: the former simply need to align to generate stresses while the latter need both to align and stretch, process that requires more time and therefore, longer distances to complete [53];

- polymers can be more effective than fibres in changing the fluid stress and thus enhancing drag reduction because, as they can be stretched by the flow, their aspect ratio can become much longer than that of regular fibres [36];
- in fibre suspensions the drag reduction mechanism seems to act in the core region of the flow while, in polymer suspensions it acts close to the wall [73], [74];
- for both polymers and fibres there is a lacking in reliable correlations to predict the friction factor behaviour, in pipe flows, depending on different variables such as pipe geometry, flow conditions and additive's concentration.

1.5 Objectives of the project

The object of this work is to build a self consistent data set investigating turbulent drag reduction in different pipes (30, 50 and 100 mm ID) with the final aim of:

- experimentally study the drag reduction phenomenon in large pipes, close to the industrial application, and compare the results with the data available in literature (often obtained in very small pipes);
- compare the effects of synthetic and bio-polymers;
- validate the new theoretical relations to predict the drag reduction in different pipe diameters and taking into account the polymer mechanical degradation;
- evaluate the cost effectiveness of polymer drag reduction;
- asses the polymer efficiency in more complex flows (like fibres suspensions).

2

Experiments

2.1 Experimental facilities

In this chapter the experimental facility will be described. Three test rigs have been used during this project:

- 100 mm internal diameter zinc-coated pipe, 35 m long (350D);
- 50 mm ID Plexiglass pipe, 12 m long (240D);
- 30 mm ID Plexiglass pipe, 8 m long (267D).

The first one is composed by two horizontal parallel zinc-coated pipes joined by a 180° bend (see fig. 2.1). The rig is installed along the laboratory side walk in a vertical plane onto the laboratory wall. There is a height difference of 2.4 m, equal to the bend diameter, between the lower and upper part of the rig. The total length of the pipe is about 35 m; a 2 m long section, made of Plexiglass, is also present to allow flow visualisation. The water

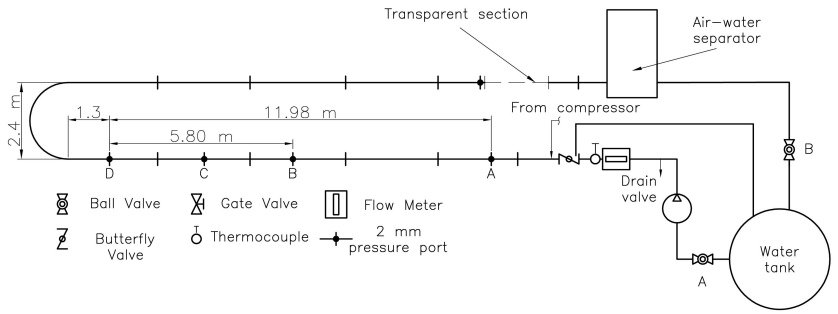

Figure 2.1: Experimental rig.

is stored in a 3000 litres tank from which it is pumped to the test section; the tank is equipped with a vortex breaker to avoid vortex formation at high flow rates. The pumping device[1] is a *KSB Sewabloc* 22 kW centrifugal pump with 120 m^3/h maximum flow rate. Downstream the pump, the flow

[1]See Appendix A for instruments specifications.

moves through a *Toshiba Tosmac* electromagnetic flowmeter whose signal is recorded by a *National Instruments NI-USB 6210* acquisition device. Then the fluid enters the test section; the first pressure port is placed $5.83\,m$ downstream the flow meter (corresponding to 58.3 diameters); four $2\,mm$ pressure ports are present and each of them was carefully machined to avoid visco-elastic hole pressure errors. Pressure ports are located on the bottom half of the pipe to prevent air entrainment into the piping connecting the port to the pressure transducer. The pressure measurements have been performed on the lower pipe, the distance from the pressure ports being 11.98 meters. A $2\,m$ long transparent section is provided at the end of the test loop to allow flow visualisation. The pipe ends into an air-water separator; this component is not critical in our experiments; nevertheless it is used as auxiliary water discharge tank whose water level can be regulated to keep always the pipe filled with water, whichever the flow rate. A ball valve installed between the air-water separator and the main storage tank is used to keep the water level in the separator almost constant. A general purpose *K type* thermocouple is placed upstream the measuring section ($1.10\,m$ after the flow meter) and it is used to monitor the fluid temperature during the experiments. Density and viscosity of the solvent can be evaluate at test temperature conditions.

The two other pipes are part of the same rig (see fig. 2.2) which is composed by two horizontal Plexiglass pipes, placed on a vertical plane. The water is stored in a 300 litres tank placed at a higher level than the *Pedrollo NGAm-1A* centrifugal pump with maximum flowrate of $21\,m^3/h$. After the pump, the fluid passes through an *Endress&Hauser* electromagnetic flowmeter and reaches a fork junction from where, with two ball valves, the 30 or 50 mm pipe can be chosen. Before reaching the junction the flow passes through a grid mixer which has been placed just after the polymer injection point to enhance the mixing with the solvent. Just after the two ball valves, fluid straighteners have been placed to reduce the effects of the bends. Carefully machined $2\,mm$ pressure ports are present along both pipes to allow pressure measurements in different locations along the line. A general purpose *K type* thermocouple is placed downstream the pump to monitor the fluid temperature. The signal from the flowmeter is collected by a *National Instruments NI-USB 6210* acquisition device.

For both rigs, differential pressure data were collected during the experiments by means of two *Müeller MHDS* differential pressure transmitters. The full measuring scale of the instrument is $700\,mbar$ with the possibility to adjust the span to enhance the accuracy of the measure. The accuracy of the instrument is $0.075\,\%$ of the span; different values of the full scale were adopted for the three pipes yielding three different accuracies: $0.1\,mbar$ for the bigger pipe, 0.05 and 0.075 *mbar* for the 30 and 50 mm pipes respectively. The transmitters are powered by a *National Instrument FP-2000/FP-AI-110* card which allows also data collection.

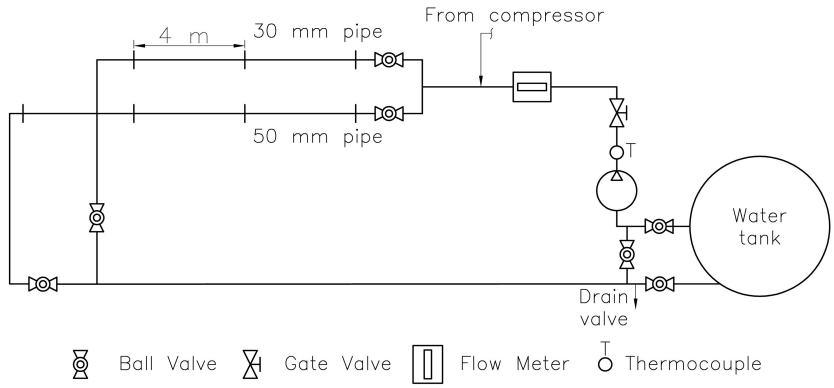

Figure 2.2: New experimental rig.

Data from the flowmeters and the pressure transducers were recorded by means of a home made *Labview* program.

2.2 Working fluids

2.2.1 Polymers

Polymers are largely used in many industrial applications such as food additives, flocculants, drilling fluids for enhanced oil recovery and drag reducers. Three kind of polymers have been used in this study:

- Xhantan Gum (XG);
- Polyethylene Oxide (PEO);
- Partially Hydrolysed Polyacrylamide (HPAM).

They have been chosen for different reasons: to compare a bio-polymer (XG) with synthetic ones (PEO and HPAM), to compare two synthetic polymers (PEO and HPAM) and to assess the dependence on molecular weight (PEO 301 and PEO 308).

2.2.2 Characterization of polymer solutions

Xantham Gum (XG here after) is a natural polysaccharide. It was discovered in the late fifties in the research laboratories of the US Department of Agriculture during research work on the industrial applications of microbial bio-polymers. Extensive research revealed that the bacterium *Xanthomonas campestris* found on cabbage plants produces a high molecular weight polysaccharide which protects the bacterium. This polysaccharide, called xanthan

gum, proved to have technically and economically interesting properties. The industrial importance of XG is based upon its exceptional qualities as a rheology control agent in aqueous systems and as a stabiliser for emulsions and suspensions. The tested polymer was produced by *CP Kelco, California* and supplied by Giusto Faravelli, Milan and consists in a fine white powder (powder size less than $75\,\mu m$). Its density is $1200\,kg/m^3$ and its molecular weight, as reported in literature, is between $4 \div 12 \cdot 10^6 g/mol$; accurate determination of the molecular weight is difficult for several reasons like: *i)* the very high molecular weight, *ii)* the stiffness of the molecule and *iii)* the presence of aggregates. Moreover, the variations in the fermentation conditions used in production are factors that can influence the molecular weight of xanthan (see Garcia-Ochoa, 2000 [24]). Once added to water it tends to aggregate and form large flocks (depending on the concentration). After strong and long lasting mixing, a homogeneous more viscous aqueous solution is obtained; the viscosity of xanthan solutions increases strongly with increasing concentration of the polymer: this behaviour is attributed to the intermolecular interaction or entanglement, increasing the effective macromolecule dimensions and molecular weight. In figure 2.3 the viscosity of xanthan gum solutions is shown for different polymer concentrations: with increasing the polymer concentration the shear-thinning effects increases. The measured results are fitted with the Cross model:

$$\eta = \eta_\infty + \frac{\eta_0 - \eta_\infty}{1 + (K\dot{\gamma})^m} \tag{2.1}$$

where η_0 is the zero shear rate viscosity, η_∞ is the infinite shear rate viscosity, K is the characteristic time of the solution which represents the beginning of the shear-thinning and m is the power law index which accounts for the shear-thinning behaviour. As can be noticed, after a Newtonian plateau, increasing the shear rate, a shear-thinning behaviour appears: this is due to the disentanglements of the polymer coils in solution and their increased orientation in the direction of the flow. In figure 2.3b the zero shear rate viscosity (see section 1.1.3) is presented as a function of polymer concentration. The visco-elastic characteristic of the polymer solution can be assessed by oscillatory rheology tests: dynamic storage G' and loss G'' moduli can provide additional information on the visco-elastic nature of xanthan gum solution. In particular G' is a measure of the reversible elastic energy while G'' is a measure of the viscous dissipation. In figures 2.4a and 2.4b the results of oscillatory tests in the different concentration regimes are presented. In the dilute limit the storage modulus G' tends to zero (Newtonian fluid behaviour) as the concentration decreases (fig. 2.4b). As the polymer concentration is increased, a crossover in G' and G'' is observed (fig. 2.4a): this signifies the passage from more liquid like to more elastic behaviour. The inverse of the crossover frequency is related to the relaxation time of the polymer. The quality of the solvent may affect the conformation of the polymer molecule and hence the rheological properties of the solution [79].

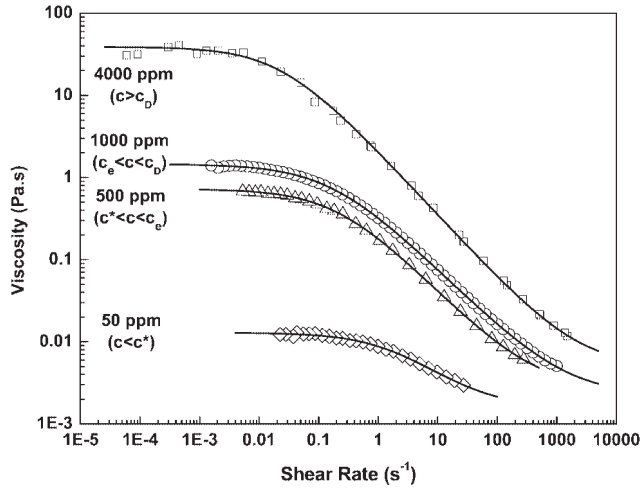

(a)

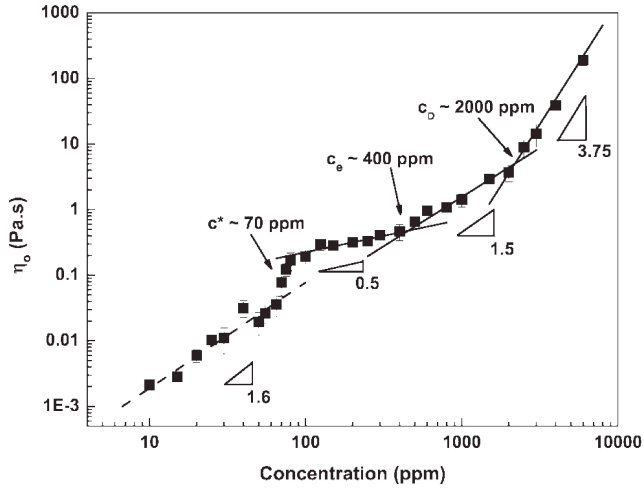

(b)

Figure 2.3: (a) Xanthan gum viscosity as a function of shear rate for several xanthan concentrations in salt-free solutions. Solid lines are Cross model fits to the measured points. (b) Zero shear rate viscosity scaling as a function of xanthan concentration in salt-free solution. Solid lines indicate theoretical scaling for $c > c^*$ and dashed lines presents power law fit below c^*. $M_w \approx 2 \cdot 10^6 g/mol$. From Wyatt & Liberatore, 2009 [79].

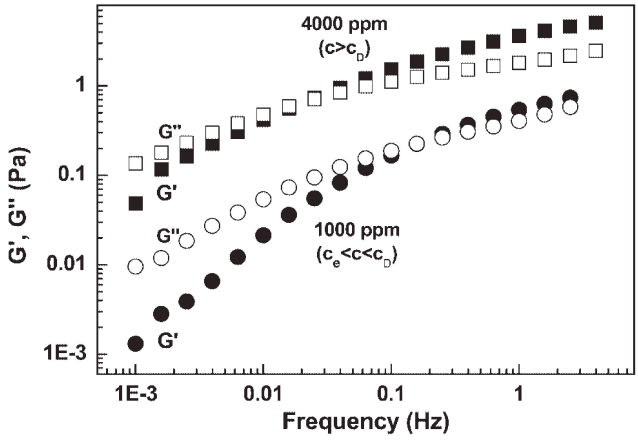

(a)

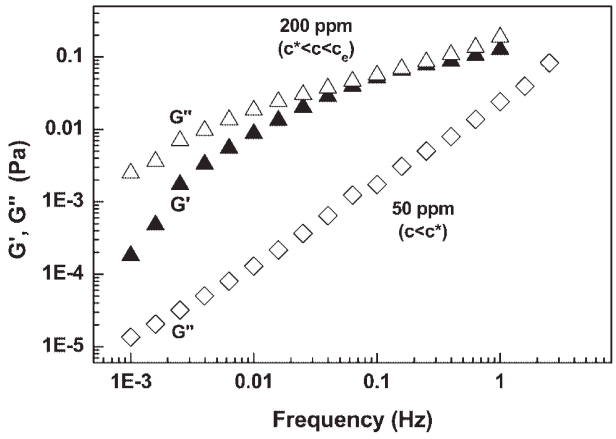

(b)

Figure 2.4: Dynamic mechanical properties (G' filled, G'' open) as a function of frequency for (a) one concentration above c_D and one concentration in the semi-dilute entangled regime and (b) one concentration in the semi-dilute unentangled regime and one in the dilute regime in salt-free solution. From Wyatt & Liberatore [79].

XG is a rod-like polymer (polyelectrolyte) and it has been used in many drag reduction studies (see Escudier, 1999 [19], Sasaki, 1991 [61]).

Polyethylene Oxide (PEO here after) is a flexible, non-ionic water-soluble polymer used in a variety of applications, depending on the molecular weight, starting from pharmaceutical to oil industries. If figure 4.2a the variation of the viscosity with the shear rate is reported for different mass concentrations: also in this case a shear-thinning behaviour can be noticed and the Cross model fits well the experimental results. Two critical shear rates have been highlighted: the onset of the Newtonian plateau $\dot{\gamma}_{c1}$ and the onset of the shear-thinning behaviour, $\dot{\gamma}_{c2}$. As mentioned above, $\dot{\gamma}_{c2} = 1/K$ where K is the time constant present in the Cross model. In figure 2.5b the loss and storage moduli are plotted as a function of the polymer concentration for three different frequencies. At low frequencies, for all PEO solutions, G'' is greater than G': this can be explained by the fact that the deformation takes place for longer time at low frequencies and consequently the major part of the energy is dissipated by viscous flow [16]. This means that the polymer chains have enough time to avoid the external imposed deformation by relaxing to an energetically more favourable state; the relaxation takes place by slippage of the entangled chains. When the frequency is increased the rheological behaviour changes from a dominantly viscous fluid ($G'' > G'$) to a dominantly elastic material ($G' > G''$): at high frequencies the relaxation time declines since the polymer chains can non longer slip one past one other and the entangled points act like fixed network junctions. The ability of this polymer network to store the temporarily imposed energy increases, leading to an elastic solid-like behaviour.

The polymers used in the present study were produced by *DOW Chemical*, supplied by Chempoint and are respectively WSR-301, with a molecular weight of $4 \cdot 10^6 g/mol$ and WSR-308, with molecular weight of $8 \cdot 10^6 g/mol$.

Partially Hydrolysed Polyacrylamide (HPAM here after) is a water soluble anionic polyelectrolyte and is a co-polymer of polyacrylamide and sodium acrylate. The shear viscosity of three different solutions is shown in figure 2.6: also in this case a shear-thinning behaviour is evident. During the experimental campaign, HPAM has proven to be more resistant to mechanical degradation than PEO.

The polymer used in this study is *Magnafloc 1011* and has been purchased from *BASF Chemical*.

2.2.3 Preparation of working fluids

Different procedures have been used to prepare the polymer solutions depending on the polymer used and the type of experiment conducted. In al the cases, tap water has been used. For the tests performed with the Xanthan Gum (see chapter 3), an homogeneous solution has been used: the polymer has been directly added to the solvent tank, to achieved the desired concentration, and then the solution has been recirculated to achieve

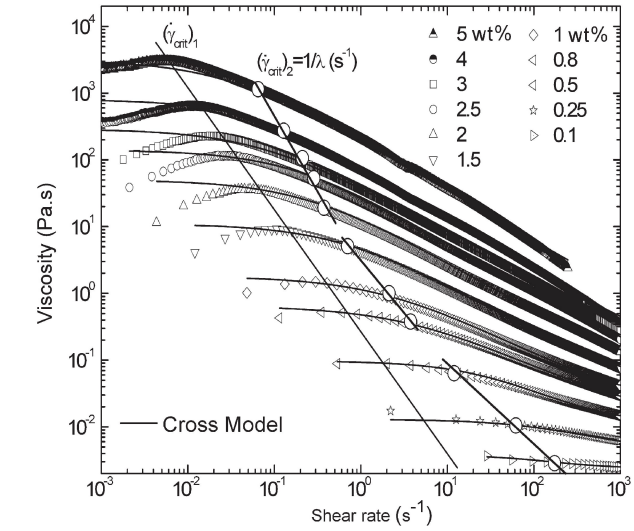

(a)

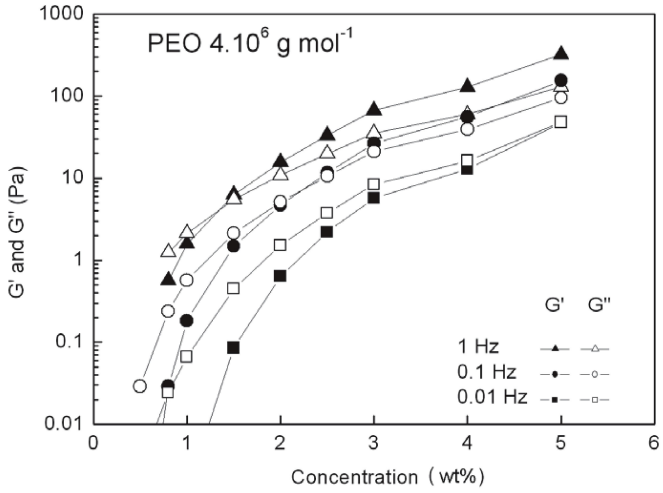

(b)

Figure 2.5: (a) Viscosity as a function of shear rate of PEO solutions of molecular weight $4 \cdot 10^6 g/mol$ at different mass concentrations. (b) Variation of loss and storage moduli as functions of PEO mass concentration at different frequencies ($M_w = 4 \cdot 10^6 g/mol$). From Ebagninin *et al.*, 2009 [16].

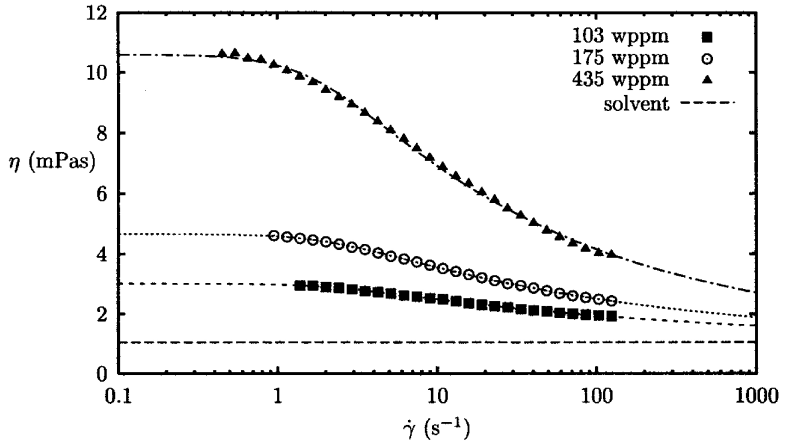

Figure 2.6: Shear viscosity of three different HPAM solutions with $M_w \approx 6 \div 8 \cdot 10^6 g/mol$. From Ptasinski [56].

homogenization. Conversely, for the PEO and HPAM tests, a master solution of 2000 ppm has been prepared slowly adding the polymer powder to the stirred solvent, leaving the polymer to homogenise under the action of the stirrer and then leave the solution to rest to completely hydrolyse. The master solution has been then injected to the pure solvent flow, at a specific flow rate, depending on the desired *in-situ* concentration. The injection has been done at the pipe wall by means of a *Medrad EnVision CT* injector system which consists in an injection syringe of volume $200\,ml$ actuated by an electrical motor; the injection flow rate can be controlled in the range $0.1 \div 9.9\,ml/s$. The injected flow rate has been calculated depending on: the master solution concentration, the desired final concentration and the solvent flow rate. For a given desired concentration, the maximum achievable flow rate was limited by the volume of the syringe.

2.3 Nylon fibres

Nylon fibres used in this project are made of *Polyamide 6.6* (PA here after) and were supplied by *Flock Depot GmbH, Germany.* The density of the fibres relative to water is 1.14 and they can be considered as rod-like particles. Fibres characteristic parameters are presented in table 2.1 where *dtex* is the weigh, expressed in grams, of a 10 000 m length wire[2].

[2]It is a typical measurement unit used in the textile industry.

dtex	d	L	L/d
[–]	[μm]	[mm]	[–]
0.9	10	1.2	120

Table 2.1: Fibres characteristic parameters.

2.4 Test conditions

The range of flow rates used during the tests depends on the rig in use. In table 2.2 the characteristic flow parameters are shown for each pipe, based on the pure solvent flow. In tables 2.4, 2.3 and 2.5 the tests matrices of the experimental campaign are presented.

D	Q_{min}	Q_{max}	q_{min}	q_{max}	$u_{b_{min}}$	$u_{b_{max}}$	Re_{min}	Re_{max}
[mm]	[m^3/h]	[m^3/h]	[l/s]	[l/s]	[m/s]	[m/s]	[–]	[–]
30	1.07	12.96	0.30	3.60	0.40	5.5	13 205	159 910
50	1.08	18.36	0.30	5.10	0.15	2.9	8479	158 580
100	9.0	108	2.5	30	0.4	3.8	35 307	392 783

Table 2.2: Flow conditions.

XG	D=100 mm				
C [%]	0.010	0.050	0.075	0.1	0.2
C [ppm]	100	500	750	1000	2000

Table 2.3: Bio-polymer tests matrix.

C \ D	30	50	100
[ppm]	[mm]	[mm]	[mm]
0.25	PEO 301 PEO 308 HPAM	PEO 301 PEO 308 HPAM	
0.5	PEO 301 PEO 308 HPAM	PEO 301 PEO 308 HPAM	PEO 308
1	PEO 301 PEO 308 HPAM	PEO 301 PEO 308 HPAM	PEO 308
5	PEO 301 PEO 308 HPAM	PEO 301 PEO 308 HPAM	
10	PEO 301 PEO 308		

Table 2.4: Synthetic polymers tests matrix.

C \ D	30	50
[%]	[mm]	[mm]
0.25		
0.5	PEO 308 0.25, 0.5, 1 ppm	PEO 308 0.25, 0.5, 1 ppm
0.75		

Table 2.5: Fibres tests matrix.

3

Drag reduction by bio-polymers

In this chapter the results presented in Campolo *et al.* [4] are collected. The focus has been placed on a semi-rigid bio-polymer, Xanthan Gum (XG), used as flow enhancer both in process and food industry, running a series of tests to measure drag reduction of aqueous solutions of the polymer at different concentrations (0.01, 0.05, 0.075, 0.1 and 0.2% w/w XG). Specifically, for each XG concentration, we measure the steady state shear viscosity and friction factor in a wide range of Reynolds numbers (from 758 to 297 000). We validate our data set against data gathered at the same scale by [19]. We evaluate and discuss the predictive ability of one empirical scaling [34] based on drag reduction data collected in laboratory scale test rigs (pipe diameter equal to 3, 5 and 6 mm, in [3]; 10, 25 and 50 mm in [63]; 2, 5, 10, 20 and 52 mm in [27]). We evaluate also changes in drag reduction expected when pipes with different cross section are used based on drag reduction data obtained for pipes with rectangular and annular cross sections [19, 38, 39]. We use our data to corroborate the relationship proposed in [31] demonstrating the capability of that model to scale up (or scale down) our drag reduction data to any larger (smaller) scale of interest. Finally, we explore the potential practical use of the correlation for the cost-effective optimization of industrial systems.

3.1 Methodology

3.1.1 Flow loop

The flow loop used for the experiments (already described in [13]) has a sightly different configuration respect to the one described in section 2.1. The centrifugal pump used in this experiments is a CALPEDA NM 65/16 AE (maximum flow rate 120 m^3/h); the fluid flow rate could be varied in the range $10 \div 81$ m^3/h changing the frequency of the inverter (SILCOVERT SVTSplus, AsiRobicon) which controls the pump.

In this work, the measuring section is limited to the last portion of the lower branch of the rig (140 D long); a general purpose resistance

thermocouple (K type) is placed upstream the measuring section and is used to monitor the fluid temperature (accuracy $\pm 1^oC$). A Yokogawa electromagnetic flow-meter (model SE200ME/NE, span 100 m^3/h, accuracy 0.5% of span for $u = [0.3 \div 1\ m/s]$, 0.25% of span for $u > 1\ m/s$) is used to measure flow rate data. High quality pressure tap holes (2 mm diameter), carefully machined to avoid visco-elastic hole pressure errors, are present at 4 positions along the measuring section (interdistance equal to 3 m); they are connected with 6 mm internal diameter clear vinyl tubing to a capacitive differential pressure transmitter (MHDS by Müller Industrie Elektronik). The accuracy on pressure drop measured by the transducer is estimated to be higher than 0.1 mbar (0.075% of Full Scale, 120 mbar). Fluid temperature was manually recorded for each flow rate acquisition and at the beginning and at the end of each test run. In house software was written (National Instrument Labview) to record flow rate and pressure drop readings during the tests.

A small stirred tank (200 L capacity, stirred by Protool MXP1202 E EF, 150-360 rpm, 1200 W, equipped with a triple spiral HS3R impeller) is provided to prepare a concentrated master solution of polymer powder and solvent (tap water). The solution is prepared according to instructions of the product data sheet: adding carefully the powder to well stirred water and continuing stirring until a smooth, clear solution is obtained. The last step to prepare the test solution is diluting the master solution with additional water to reach the desired polymer concentration inside the feeding tank. Final homogenization of the polymer solution in the tank is obtained by circulating the fluid through the short return loop (3 m length overall, not shown in fig. 2.1).

For visco-elastic fluids the entry length can be significantly larger than for a Newtonian fluid in both laminar [54] and turbulent flow conditions [26]. Therefore, a number of preliminary tests was performed to identify the best pair of pressure ports to be used to collect accurate measurements of differential pressure readings. The objective of these tests, performed using tap water and 0.2% XG solution as test fluids, was threefold: *i)* verify that, for each fluid, the flow was fully developed in the measuring section in the range of Reynolds number tested (i.e. the specific pressure drop was independent from location and inter-distance of pressure taps); *ii)* choose the pair of pressure taps for which the error on differential pressure can be minimized; *iii)* gather data for the reference pressure drop measured along the pipe when pure solvent is flowing. Tests results showed that difference in pressure loss per unit length of pipe measured using ports B-C and B-D (see fig. 2.1) for both water and 0.2% XG was less than 1%, indicating fully developed flow in the measurement section. Pressure taps B and D were finally selected to measure pressure loss to maximize the accuracy of $\Delta p/L$ values. Ports B and D are almost 6 m apart (60 D), with tap B 6 m (60 D) downstream the flow meter and tap D 1 m (10 D) upstream the inlet of the return bend.

3.1.2 Test fluid characterization

The fluids used in the present work are aqueous solutions of Xanthan Gum, a pharmaceutical grade supplied by CP-Kelco (commercial name Xantural 75). The complete rheological characterization of the XG solutions should be based on continuous shear experiments to evaluate shear viscosity and first normal stress difference [22, 79], oscillatory shear experiments to evaluate storage and loss moduli [6], extensional flow tests to evaluate extensional viscosity [39] and dynamic light scattering analysis to highlight any change in the polymer chain conformation as a function of concentration, temperature and solvent type [60]. Such a complete rheological characterization is beyond the scope of this work and we decided to focus only on a subset of relevant rheological quantities. As discussed by [31], the minimal set of parameters required to develop predictive correlations includes the viscosity of the solution at the wall and a time scale (polymer relaxation time) representative of the response of the polymer under extensional deformation encountered in turbulent flows. Therefore, we performed steady state shear viscosity tests to define a rheological constitutive equation predicting fluid viscosity at the wall, and we decided to rely on the *a posteriori* evaluation of an effective polymer relaxation time directly from drag reduction data.

The steady shear viscosity of the test fluids was determined using a stress controlled rheometer (Haake RS150) equipped with cone and plate geometry ($C60/1^o$). Temperature control of the solution during testing was done using a refrigerated water bath (Thermo/Haake F6). Each test for the rheological characterization of the fluid was performed according to the following procedure: a mild shear condition (constant shear rate 100 s^{-1}, corresponding to shear stress values in the range $0.1 \div 3.7$ Pa, maintained for 120 s) was imposed to the sample to cancel any effect of the previous rheological history and followed by a stepwise sequence of ascending shear stress values (10 per decade and logarithmically spaced in the range $0.02 \div 20$ Pa). The duration of each constant stress segment was 90 s or shorter if the steady state response of the fluid was attained or approached with a preset approximation. The wide shear rate interval explored in the experimental tests covers quite different structural conditions, ranging from an almost unperturbed polymer configuration to stretched and oriented chain conformations, expected when the fluid is circulated inside the experimental loop.

Figure 3.1 shows the results of rheological tests performed at $T = 20^oC$ for the characterization of the five polymeric solutions. Additional measurements were made also at 15^oC and 25^oC (not shown). Figure 3.1a shows shear stress versus shear rate measured by the rheometer for the various XG solutions (solid symbols). The solid line represents the linear relationship between shear stress and shear rate for tap water, our reference Newtonian fluid. The range of shear stress values investigated is wider than that expected for water moving at different flow rates inside the experimental loop, shown by

the dashed horizontal lines labelled as Min and Max $\tau_{w,water}$. Figure 3.1b shows viscosity variation versus shear rate.

The Carreau-Yasuda constitutive equation [81] was used to fit the data corresponding to each polymer concentration

$$\frac{\eta - \eta_\infty}{\eta_0 - \eta_\infty} = \frac{1}{[1 + (\lambda\dot{\gamma})^a]^{n/a}} \tag{3.1}$$

In Eq. (3.1), η is the shear viscosity, η_0 and η_∞ are viscosity at the zero-shear and infinite-shear plateaus while λ, n and a represent the inverse shear rate at the onset of shear thinning, the power law index and the parameter introduced by [81]. Table 3.1 summarizes the values of fitting parameters evaluated using the methodology outlined in [21]. The corresponding curves are shown as dotted lines on the graph.

Figure 3.1b shows also the rheological characterization of two 0.2% XG solutions: the former (Kelco Division of Merck and Co.) used by [20] to perform drag reduction experiments in their 100 mm diameter pipe and the latter (Keltrol TF, Kelco Division of Merck and Co.) used by [39] to perform drag reduction experiments in an annular pipe. Both curves, drawn based on the values of the fitting parameters reported in table 3.1, indicate that large deviations can exist between viscosity values measured for nominally identical XG solutions. Since we will compare directly our drag reduction data with those of [20], we believe important to assesss how large these differences can be. The relative difference between our and [20] viscosity data indicates up to 20% overestimation in the low shear rate range and up to 15% underestimation in the high shear rate range. Our shear viscosity data are 30% lower than those by [39] in the low shear rate range to 20% lower in the high shear rate range.

We processed further our rheological data to derive a model equation predicting viscosity variation for XG solutions as a function of both polymer concentration and shear rate. Details are given in section 3.1.3.

3.1.3 Model equation to predict viscosity of XG solutions

Figure 3.2a shows the log-log plot of zero-shear viscosity versus concentration obtained for our data (solid circles) and for XG data available from the literature (open triangles, data from [39]; open circle, data from [20]). The two solid lines represent power law equations of the type $\eta_0(C) = K_H \cdot C^{n'}$ fitting the experimental data in the dilute (smaller slope) and semi-dilute (larger slope) polymer concentration region. Present data indicate a critical overlap concentration at about 0.05%, which is in agreement with data found in the literature (0.067% in [39]; 0.08% in [79]). Values of fitting parameters are $K_H = 0.066$ and $n' = 0.8446$ in the dilute region and $K_H = 1073.83$, $n' = 4.08$ in the semi-dilute region. According to [39], $\eta_0 \propto C^{1.56}$ and

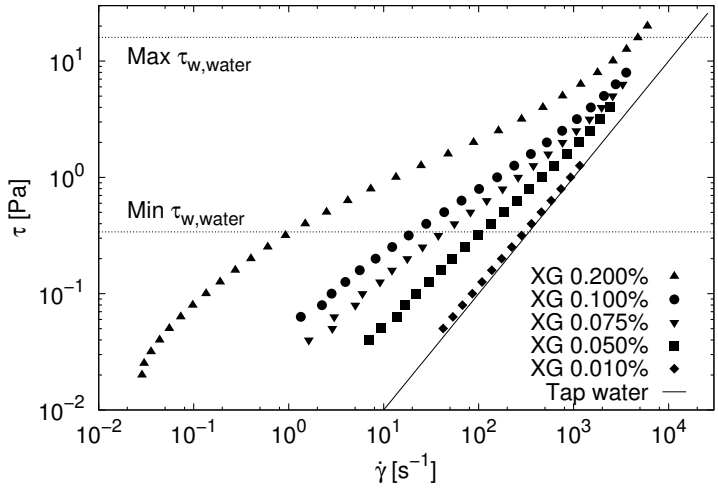

(a)

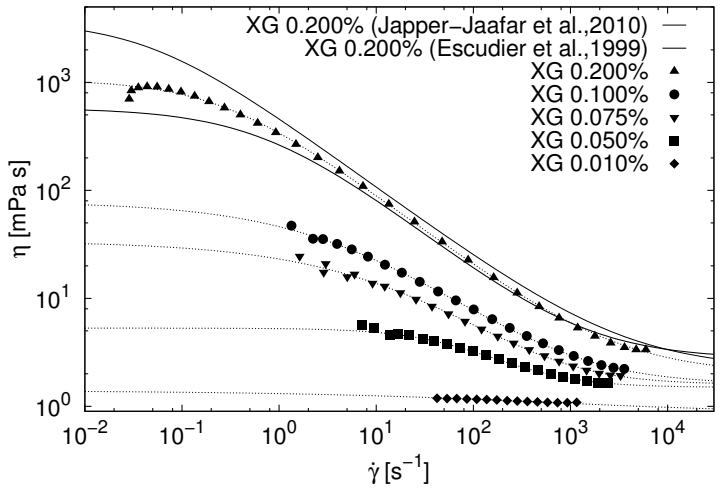

(b)

Figure 3.1: Results of rheological characterization: (a) shear stress, τ, versus shear rate, $\dot{\gamma}$ measured in rheometer for various XG concentrations (symbols) and reference curve for water (solid line); shear stress is in the range $[0.02 \div 20\ Pa]$, dashed lines indicate range of variation of shear stress at pipe wall, τ_w in the hydraulic loop; (b) viscosimetric data for various Xanthan Gum concentrations together with the Carreau-Yasuda fits (dotted lines) [81]. Data for XG 0.2% from [20] are shown by a thick solid line. Data for XG 0.2% from [39] are shown by a thin solid line.

Carreau-Yasuda model parameters for XG at 20^oC					
C	η_0	η_∞	λ	a	n
$[\%]$	$[mPa \cdot s]$	$[mPa \cdot s]$	$[s]$	$[-]$	$[-]$
0.01	1.36	0.94	0.00002	0.271	1.00
0.05	5.29	1.54	0.01124	0.940	1.00
0.075	33.88	1.63	0.02454	0.437	1.00
0.1	78.45	1.65	0.21557	0.510	0.73
0.2	1062.43	1.95	3.68927	0.796	0.68
0.2[1]	578.	2.76	1.30	0.724	0.724
0.2[2]	3680.	2.24	21.5	0.81	0.66

[1] Fitting parameters from [20].
[2] Fitting parameters from [39].

Table 3.1: Fitting parameters of Carreau-Yasuda model for XG solutions: η_0 and η_∞ are viscosity at the zero-shear and infinite-shear plateaus, λ, n and a are inverse shear rate at onset of shear thinning, power law index and the parameter introduced by [81].

$\propto C^{4.66}$ in the dilute and semi-dilute region. According to [79], $\eta_0 \propto C^{2.0}$ and $\propto C^{4.67}$ in the dilute and semi-dilute region.

Figure 3.2b shows the variation of viscosity versus XG concentration calculated from the Carreau-Yasuda model fit to our experimental data. Symbols represent different values of shear rate whereas each solid line is a power law fit made only for points at constant shear rate in the semi-dilute range of polymer concentration. For clarity of presentation, only values of shear rate in the range $[10^{-1} \div 10^4]$ are shown. For each value of shear rate, the fitting equation can be written as

$$\eta(C, \dot{\gamma}) = K'_H(\dot{\gamma}) \cdot C^{n''(\dot{\gamma})} \tag{3.2}$$

This equation can be used to predict changes in viscosity as a function of shear rate and XG concentration if the functional relationships $K'_H(\dot{\gamma})$ and $n''(\dot{\gamma})$ are known. Figure 3.2c summarizes the value of parameters $K'_H(\dot{\gamma})$ and $n''(\dot{\gamma})$ derived from the fitting procedure. This graph can be used to estimate the viscosity of XG solutions for which the direct rheological characterization is not available.

3.1.4 Evaluation of drag reduction: testing protocol

We gathered differential pressure and flow rate data for a number of different flow rates (from 10 to 81 m^3/h for tap water) increasing stepwise the frequency of the inverter in the range 13-50 Hz (step 2 Hz). After each change of inverter frequency, we monitored in time the flow rate variation to identify the length of the transient necessary to reach steady state conditions inside the flow loop (about 5 min at the smaller flow rates and about 1 min

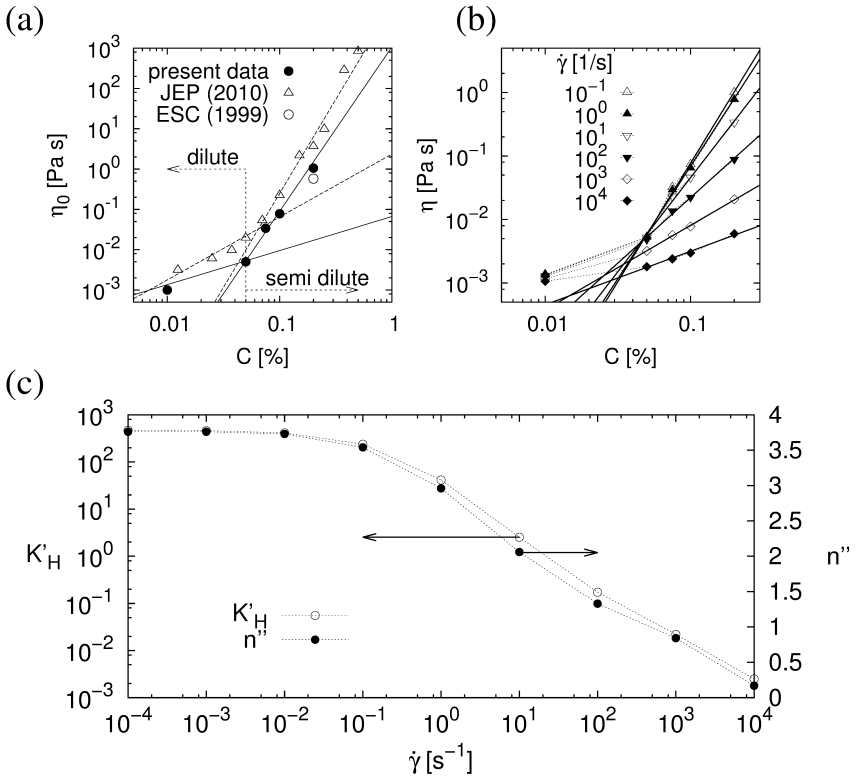

Figure 3.2: Results of rheological data processing: (a) variation of zero-shear viscosity versus concentration; present data (solid circle); ESC (1999) data [20] (open circle); JEP (2010) data [39] (open triangle); power law fitting of data in the dilute and semi-dilute concentration range (solid line, present data; dashed line, JEP data); (b) variation of viscosity versus concentration: symbols identify different values of shear rate, $\dot{\gamma}$, solid lines are power law fit, $\eta = K'_H \cdot C^{n''}$, for concentration values larger than 0.01%; (c) value of fitting parameters K'_H and n'' as a function of shear rate, $\dot{\gamma}$.

at the larger flow rates). From this time on, we sampled data for a time period of 2 minutes (data acquisition rate of 5 Hz). Statistics calculated from sampled data were used to *i)* identify average values of $Q, \Delta p$ pairs and to *ii)* check variability of test conditions during each steady state. During each steady state, the standard deviation of flow rate data was comparable with the accuracy of the flow meter ($\pm 0.5\ m^3/h$) for both tap water and XG solutions. The standard deviation of the pressure signal was found to increase proportionally with the flow rate, ranging within $[0.8 \div 8\ mbar]$ for tap water and dilute XG solution (XG <0.10%); the standard deviation of the pressure signal was found to be almost independent of the flow rate ($[0.5 \div 0.6\ mbar]$) for the more concentrated 0.2% XG solution.

Tests were performed in triples to assess their repeatability over time. Average values of $Q, \Delta p$ gathered over the three tests were then compared to identify deviations due to other effects, such as temperature changes or ageing of polymer solution. We observed no systematic change of Δp over the three tests (generally performed within three subsequent days), indicating no significant mechanical degradation of the polymer during testing; whereas, since we did not used biocides, we observed the spontaneous development of microbial activity in concentrated solutions after the fourth day of storage when environmental temperature was above 20^oC.

3.2 Results

3.2.1 Velocity and specific pressure drop

Figure 3.3 shows average values of specific pressure drop: pressure drop per unit length, $\Delta p/L$, versus section averaged bulk velocity, $u = 4Q/\pi D^2$, calculated from measurements made in the flow loop. Each point represents the average over three tests, while errorbars identify data variability among the three tests performed. Considering the repeatability of each test, the accuracy of flow rate measurements was estimated to be better than ±2.5% whereas the accuracy of pressure drop measurements was estimated to be better than ±4%. Maximum variability of pressure drop was larger (±10%) for tests performed using 0.075% XG solution.

Empty circles represent the specific pressure drop measured for tap water. The solid line corresponds to the value of the specific pressure drop calculated assuming that the pipe is hydraulically smooth. In such condition, the friction factor can be calculated as

$$f = \frac{16}{Re}, \text{ if } Re \leq 2100 \tag{3.3}$$

$$\frac{1}{\sqrt{f}} = 1.7 \cdot \ln(Re\sqrt{f}) - 0.4, \text{ if } Re > 2100 \tag{3.4}$$

Equation (3.4) is known as the von Kármán equation. The agreement between experimental data and the calculated values of specific pressure

drop is excellent, confirming the proper calibration of the experimental set up.

The specific pressure drop measured for XG solutions is shown by solid symbols. The arrow indicates increasing XG concentration. For velocity values in the range $u = [0.35 \div 1\ m/s]$, the measured value of specific pressure drop is about the same as in tap water for most of the aqueous XG solutions. A different behavior is observed only for the largest concentration tested, 0.2% XG, where the measured specific pressure drop is larger than for tap water. Drag enhancement at large polymer concentration and small Reynolds number has been already observed for rigid polymers [1, 55] and attributed to the homogeneous increase of effective viscosity of the fluid which prevails over the reduction of momentum flux to the wall. At larger Reynolds number, i.e. for velocity values in the range $u = [1 \div 3\ m/s]$, the measured specific pressure drop for XG solutions is always less than in tap water. The largest reduction in specific pressure drop is found at the largest concentration of XG.

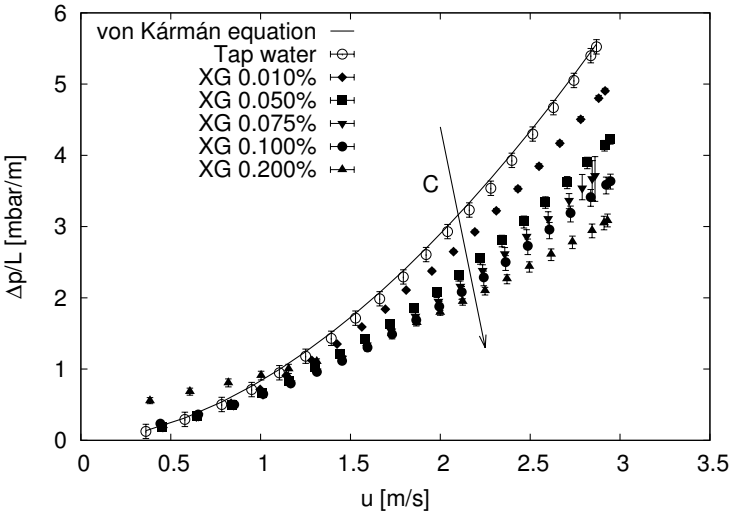

Figure 3.3: Specific pressure drop versus bulk velocity for tap water (open symbol) and aqueous XG solutions (solid symbols). Errorbars represent data variability over three independent tests. Solid line is value of specific pressure drop calculated using friction factor given by Eq. (3.4). Solid symbols represent different values of XG concentration. The arrow indicates increasing XG concentration.

3.2.2 Comparison against literature data

Same geometrical scale [20]

We compared friction factor data measured for our 0.2% XG concentration solution with those measured by [20] in a rig of the same diameter. To this aim, we calculated the Fanning friction factor, f as

$$f = \frac{2\tau_w}{\rho u^2} \quad \text{with} \quad \tau_w = \frac{\Delta p}{L}\frac{D}{4} \tag{3.5}$$

and the generalized Reynolds number, $Re = Re_{MR}$, for a shear-thinning fluid defined as

$$Re_{MR} = \frac{\rho u D}{\eta^*} \tag{3.6}$$

where ρ is the fluid density, u is the average velocity, D is the internal diameter of the pipe and η^* is the effective viscosity of the fluid. This definition of the Reynolds number is equivalent to the generalized Reynolds number defined by [50] for laminar flow, and is still meaningful for turbulent flow [5]. The effective viscosity is evaluated as

$$\eta^* = \frac{\eta(3n_{pl}+1)}{4n_{pl}} \tag{3.7}$$

where η is the apparent viscosity corresponding to the pressure drop measurement (see Eq. (3.5)) in the Carreau-Yasuda model fit to the steady-shear viscosity measurements; the second factor is the Weissemberg-Rabinowitsch correction where n_{pl} is the (local) power law index of the fluid (also evaluated from the rheological data). Using this definition, Eq. (3.3) represents the reference curve to fit friction factors calculated for Newtonian and non-Newtonian fluid in the laminar region. Here after, we will use indifferently Re or Re_{MR} to refer to the generalized Reynolds number.

Figure 3.4 shows the variation of the friction factor versus Reynolds number for the different aqueous solutions of XG tested. Considering the repeatability of each test and the accuracy of flow rate and pressure drop measurements, we estimated maximum experimental uncertainties up to $\pm 2.5\%$ for the generalized Reynolds number and up to $\pm 9\%$ for the friction factor. The curve corresponding to the friction factor for laminar/turbulent flow in a smooth pipe calculated using Eq. (3.3) and (3.4) is shown as a solid line; the maximum drag reduction (MDR) asymptote found by Virk [74], given by

$$\frac{1}{\sqrt{f}} = 8.2515 \cdot \ln(Re\sqrt{f}) - 32.4 \tag{3.8}$$

is shown as a dotted line. The experimental data obtained by [20] (XG 0.2%, open triangle pointing upward) are also shown for comparison.

Consider first our data (solid symbols only). For each value of the Reynolds number, the friction factor calculated for XG solutions is always

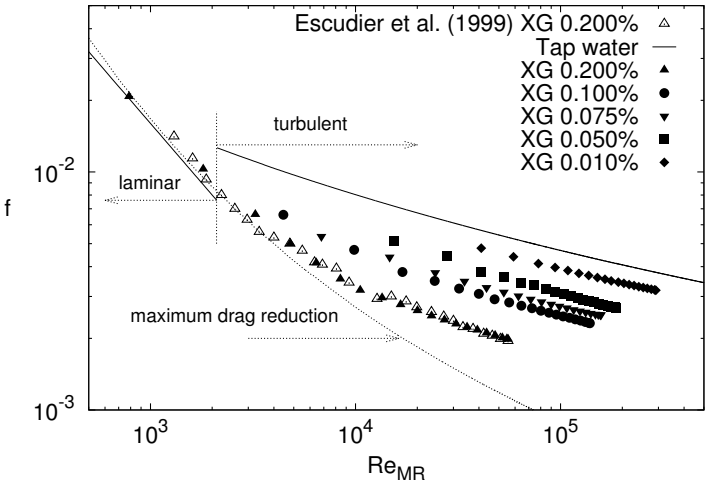

Figure 3.4: Comparison against data from [20]: friction factor, f, versus generalized Reynolds number, Re_{MR}; curve for tap water (solid line), maximum drag reduction asymptote (dotted line), data for different XG solutions (solid symbols) and data from [20] (open triangles).

smaller than for tap water (solid line); the difference between friction factors of XG solution and tap water increases with polymer concentration. The difference does not significantly change as the Reynolds number increases, indicating a Type-B behavior (rigid, rod-like chain) for XG (see [27]). For XG 0.2% and in the small flow rate region ($\simeq 10\ m^3/h$, corresponding to $Re_{MR} \simeq 1000$, i.e. in the laminar regime), the values of the friction factor for the polymeric solution align along the laminar curve and to the Virk MDR asymptote.

Comparison between our data obtained for XG 0.2% (solid triangle pointing upward) with those by [20] (open triangle pointing upward) indicates very good agreement: deviations are within $\pm 7\%$ for $Re_{MR} < 4000$ and decrease down to 2% at larger Reynolds numbers.

Scale up of drag reduction data from smaller diameter pipes

Similarly to other polymers, also for XG solution drag reduction was measured many times in small diameter pipes [3, 27, 61]. In this work, we tried to scale up data available from the literature to the size of our pipe. After a review, we selected the data by [3] as a candidate data set to test the accuracy of scaling laws available from the literature. Experiments were performed in three different pipes ($D_1 = 3.146\ mm$, $D_2 = 5.186\ mm$ and $D_3 = 6.067\ mm$) using two commercial XGs (Flocon 4800C by Pfizer

in tap water and Rhodopol 23 by Rhone-Poulenc in distilled water added with 100 ppm NaCl) for 0.01%, 0.1% and 0.2% XG concentrated solutions. Polymer additive, values of concentration and type of solvent are similar to our experiments, whereas pipe diameters are much smaller.

The difficulty of scaling up such data was early pointed out by [35], among others. They defined %DR as

$$\%DR = 100 \cdot \left. \frac{\Delta p_w - \Delta p_p}{\Delta p_w} \right|_{Q=const} = \%DR_Q \tag{3.9}$$

where Δp_w and Δp_p are the pressure drop measured for the Newtonian fluid (water) and for the polymer added fluid flowing, at the same flow rate Q, along the pipe. They found that %DR data measured for specific polymeric solutions flowing in pipes of different size and plotted versus pipe diameter depend on the pipe size: for small pipes, %DR can be very high, reaching the Virk MDR asymptote; for larger pipes, %DR moves away from the MDR asymptote, decreasing as the diameter increases and eventually reaching a plateau when the pipe diameter is large enough (order 10^2 for Guar Gum and order 10^3 mm for Hydropur SB125 from their data). This "pipe diameter effect" actually prevents the direct use of data collected at the small scale, $D_1 \simeq O(10^1)$ mm, to infer the drag reduction expected at the larger scale, $D_0 \simeq O(10^2 \div 10^3)$ mm. As a result, a number of design equations have been proposed to scale up DR data (see [63] and more recently [25, 27] among others).

We followed the work of [63] and subsequent works by [33] and used the "negative roughness" approach to scale the small diameter data (D_1, D_2 and D_3) to our pipe dimension (D_0). The methodology is based on the assumption of similarity between velocity profiles in pipes of different size, which is generally satisfied unless the size of the experimental pipe becomes too small. In such case, the similarity of velocity profiles is broken because of the growing extension of the viscous sub-layer (see [34]). In Bewersdorff's data base [3], pipe diameters are 20 to 30 times smaller than our pipe and this might make the scaling inaccurate [34].

The scaling is based on two equations which allows to transform the Prandtl-Kármán (P-K) coordinates corresponding to data obtained for pipe dimension D_i to P-K coordinates corresponding to data obtained for pipe dimension D_0. Equations are the following

$$(Re\sqrt{f})_0 = (Re\sqrt{f})_i \cdot \left(\frac{D_0}{D_i} \right) \tag{3.10}$$

to translate the x-coordinate, and

$$\frac{1}{\sqrt{f}} = 1.7 \ln \left(\frac{Re\sqrt{f}}{4.67} + N \right) + 2.28 \tag{3.11}$$

to translate the y-coordinate. Equation (3.10) states that, to make meaningful comparison between scale D_i and D_0, the shear stress (and the shear

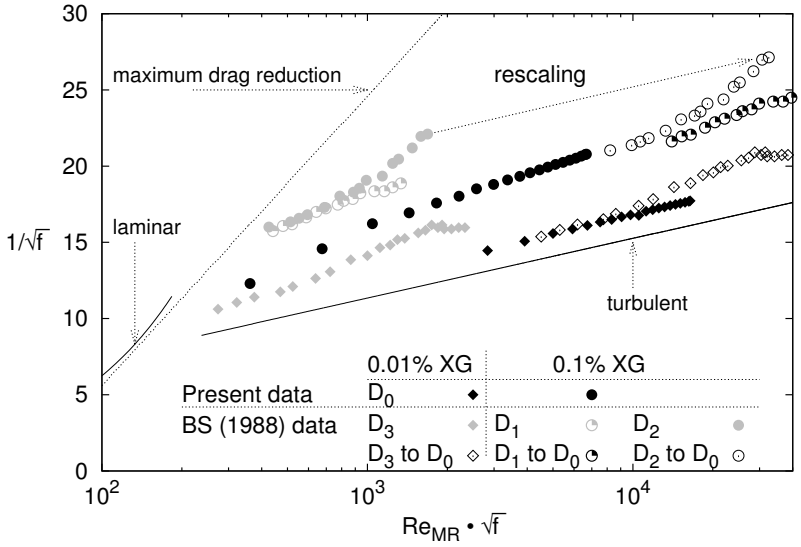

Figure 3.5: Comparison against Bewerdorff and Singh (BS) [3] data: 0.01% XG (diamonds), 0.10% XG (circles); present data (solid symbols), original BS data (gray symbols) ($D_1 = 3.146\ mm$, $D_2 = 5.186\ mm$, $D_3 = 6.067\ mm$), BS data rescaled to $D_0 = 100\ mm$ (open symbols).

velocity) should be the same in the two geometries. This produces the same level of conformational change (uncoiling/stretching and/or preferential orientation) of the polymers (and the same rheological behavior for the testing fluid) in the small and in the large pipe. Equation (3.11) is the analogous of Colebrook equation [8] including a negative roughness parameter $N = D/k$, where k is the dimensional "negative roughness". It is used twice: the first time to calculate the value of the negative roughness N using the pair of $(Re\sqrt{f}, 1/\sqrt{f})$ values known at scale D_i, and the second time to evaluate $1/\sqrt{f}$ at scale D_0.

Figure 3.5 shows original data from [3] (gray symbols), rescaled data (open symbols) and our data (solid symbols). Diamonds refer to 0.01% XG whereas circles to 0.10% XG. Solid and dotted lines represent data for tap water and Virk [74] MDR asymptote as in previous graphs. We should remark here that we did not considered for scaling those original data which lay in the MDR region. Therefore, we disregarded the entire 0.2% XG concentration data set of [3] and some points from the other two data sets.

Compared to original data (gray symbols), rescaled data (open symbols) matching the equivalent shear rate condition in the larger pipe are shifted upward and to the right (as indicated by the dashed arrow). For 0.01% XG (Rhodopol 23 with 100 ppm NaCl) (diamonds), the agreement between our data and rescaled data by [3] is quite good even if type A drag reduction (i.e. different slope of polymer solution and solvent data) is observed for that data set whereas type B drag reduction (i.e. same slope of polymer solution and solvent data) is observed for our data set. The difference in $1/\sqrt{f}$ is less than 3% for $Re\sqrt{f} < 10^4$ and $4 \div 7\%$ for $Re\sqrt{f} > 10^4$. This corresponds to deviation in the friction factor in the range $7 \div 12\%$. Deviation are most likely due to the different concentration of NaCl in the two testing fluids (100 ppm in [3], versus $\simeq 50$ ppm in our tap water), resulting in a different flexibility of the polymer (see [27]).

Data shown in [3] for 0.1% XGs (circles) correspond to the two different XGs tested: Rhodopol 23 with 100 ppm NaCl for solid gray symbol and Flocon 4800 C in tap water for white and gray symbol. As apparent from the plot, after rescaling to diameter D_0 data collected in pipe D_1 and D_2 exhibit type B and type A drag reduction, respectively. Only a qualitative comparison is possible between rescaled data and our data since they span a different range of $Re\sqrt{f}$. However, rescaled data corresponding to the Flocon in tap water data set seem to align with our data along one single line parallel to the Kármán line.

Effect of pipe cross section

We compared our drag reduction data with data available for aqueous solutions of XG in rectangular and annular pipes [18, 38, 39] to check if any systematic difference exists in drag reduction due to the shape of the pipe. This information may be useful for design purposes since in many industrial

devices (e.g. heat exchangers, air conditioning systems) circular pipes are not the typical choice and drag reduction is still a crucial issue.

Escudier [18] (ENP in fig. 3.6) evaluated drag reduction in a rectangular pipe (height $H = 25\ mm$, width $W = 298\ mm$, hydraulic diameter $D_{H1} = 46\ mm$ and aspect ratio $W/H = 11.92$) for flow rates up to 90 m^3/h. The aspect ratio of their pipe was large enough to hypothesize strong 2D flow in the cross section. The Xanthan Gum was Keltrol TF, supplied by Kelco Ltd, and was tested at 5 different concentrations (0.03, 0.05, 0.067, 0.08 and 0.15% w/w XG). Data selected for comparison are from the 0.05% XG data set: points are far from the MDR asymptote and the concentration is one of those we tested. Original data, available in the form of (Re, f) pairs (with the Reynolds number $Re = HDu/2\nu$ defined based on the channel half-height) were converted into (Re_H, f) pairs (with $Re_H = 4Re$ defined based on the hydraulic diameter) and rescaled using Eq. (3.10) and (3.11).

Jafar [38, 39] (JP in fig. 3.6) evaluated drag reduction in an annular pipe ($D_{inner} = 50.8\ mm$, $D_{outer} = 100\ mm$, hydraulic diameter $D_{H2} = 49.2\ mm$) and flow rates up to 90 m^3/h. The Xanthan Gum was Keltrol TF, supplied by Kelco Ltd, and was tested at 3 different concentrations (0.0124, 0.07 and 0.15% w/w XG). Data selected for comparison are from the 0.0124 and 0.07% XG data sets: points are far from the MDR asymptote and the concentrations are similar to the ones tested. Original data available in the form of Reynolds number (based on hydraulic diameter) and friction factor were rescaled using Eq. (3.10) and (3.11).

Figure 3.6 shows the comparison between data obtained for the rectangular (ENP) and the annular (JP) geometry and present results. Diamonds, squares and triangles correspond to 0.01% XG, 0.05% XG and 0.075% XG concentrations, respectively. Our data are shown as solid symbols, original JP/ENP data are shown as gray symbols and rescaled JP/ENP data are shown as open symbols. The values of hydraulic diameters ($D_{H0} = 100\ mm$, circular pipe, $D_{H1} = 46\ mm$ for the rectangular pipe and $D_{H2} = 49.2\ mm$ for the annular pipe) corresponding to each geometry are also indicated.

Despite the very different shapes of pipe cross sections used to collect the friction factor data, the comparison indicates a quite good agreement: for the annular section, deviation between JP and our friction factors is about $7 \div 8\%$ for 0.01% XG, whereas there is an almost perfect agreement (error less than 2%) for 0.075% XG. For the rectangular section, the error on the friction factor is 5% at maximum.

3.2.3 Assessment of predictive correlation by Housiadas and Beris [31]

We used our data to assesss the correlation developed by [31] to predict the friction factor in visco-elastic turbulent pipe flow. According to their model, the visco-elastic response of a polymer solution is described by a universal drag reduction curve in which the Weissemberg number, defined as the ratio

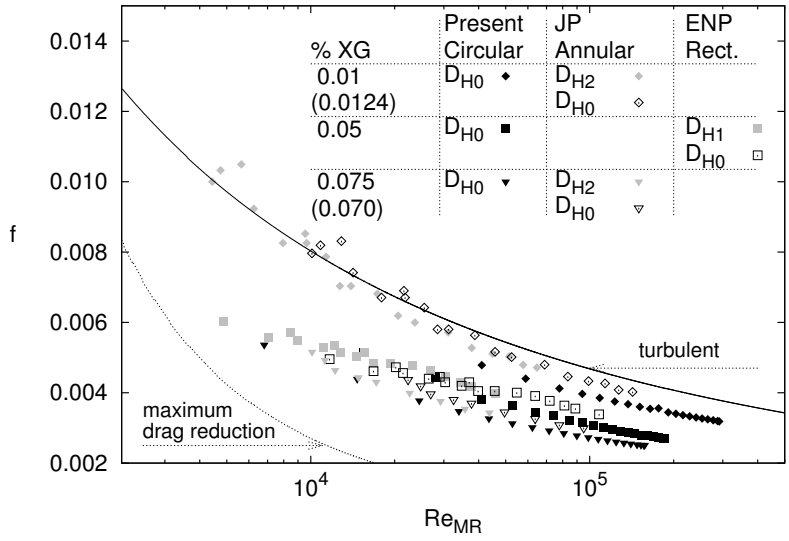

Figure 3.6: Effect of pipe cross section: drag reduction data measured for annular [38] (JP) and rectangular [18] (ENP) section at different XG concentrations (diamonds, 0.01% XG; squares, 0.05% XG and triangles 0.075% XG); our data (solid symbols), original JP/ENP data (gray symbols) ($D_{H1} = 46\ mm$, $D_{H2} = 49.2\ mm$), JP/ENP data rescaled to $D_{H0} = 100\ mm$ (open symbols).

of the polymer relaxation time to the time scale of turbulence at the wall, $We_\tau = \lambda^* u_\tau^2/\nu$ is the independent parameter. $We_\tau \simeq O(1)$ ($We_\tau \simeq 6$ from DNS results) identifies the onset of drag reduction whereas for large enough values of We_τ the DR levels up to a limiting value (Limiting Drag Reduction, LDR).

The correlation is therefore based on two dimensionless parameters: *i)* the zero shear-rate elasticity parameter, El_0, defined as $El_0 = \lambda^* \nu_0/R^2$ where λ^* is a scale for the polymer relaxation time, $\nu_0 = \eta_0/\rho$ is the kinematic zero shear-rate viscosity of the solution and R is pipe radius; and *ii)* the Limiting Drag Reduction, LDR (i.e. the drag reduction observed at high Weissemberg numbers). The predictive equation can be written as

$$\begin{aligned}\frac{1}{\sqrt{f}} =& \frac{1}{(1-DR)^{\tilde{n}/2}} \cdot \\ & \cdot \left(1.7678 \cdot \ln(Re\sqrt{f}) - 0.60 - \frac{162.3}{Re\sqrt{f}} + \frac{1586}{Re^2 f}\right)\end{aligned} \tag{3.12}$$

where DR is the drag reduction produced by the polymer in any specific flow conditions and $\tilde{n}$ is a coefficient which is a weak function of Re.

In figure 3.7 we show the percent drag reduction calculated from our data according to the definition given by [31]

$$\%DR_\tau = \left[1 - \left(\frac{Re^{(visc)}}{Re^{(Newt)}}\right)_{Re_\tau}^{-2/\tilde{n}}\right] = 100 \cdot DR \tag{3.13}$$

where the bulk Reynolds number for the viscous and the Newtonian fluid are evaluated at the same value of friction Reynolds number (shown along the x-axis).

From the plateau of $\%DR_\tau$ shown in figure 3.7 we estimated the value of LDR, which is different for each polymer concentration. We used the value of Re_τ corresponding to the onset of drag reduction for the 0.2% XG concentration data set (identified by the open triangle) to calculate the zero shear rate elasticity value ($El_0 = 0.087$) and the time scale for the polymer relaxation ($\lambda^* = 0.20\ s$ for 0.2% XG). Oscillatory shear stress tests performed by [79] on salt free solutions of XG in the range of concentration $200 \div 2000$ ppm indicate an almost constant value of the polymer relaxation time ($\simeq 10\ s$) [79]. This value is quite different from the relaxation time of the model λ^* confirming the inherent difficulty already underlined by [31] in linking the polymer relaxation time scale of the model with data derived from rheological tests. Given the difficulty of estimating an indipendent value of El_0 for each XG concentration from our experimental data (the onset is not defined for $XG \neq 0.2\%$) we decided to use the same value of the fitting parameter El_0 whichever the XG concentration. Values of the dimensionless parameters used in the correlation are summarized in table 3.2.

In figure 3.8 we show our experimental data together with the prediction obtained from the correlation (dashed lines) (see section 3.2.5 for details on

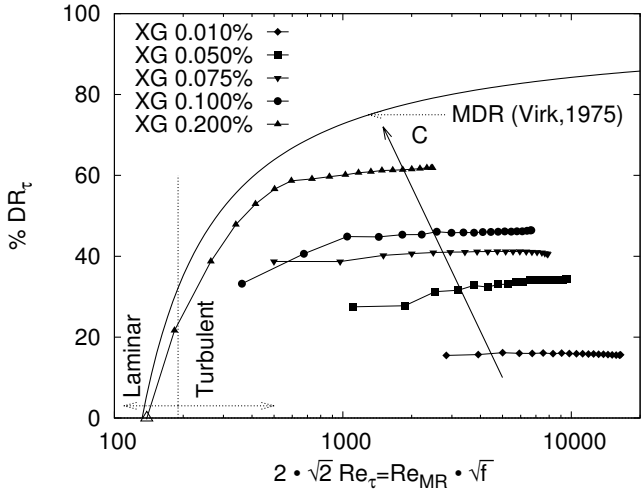

Figure 3.7: Percent drag reduction for aqueous solutions at different XG concentrations as a function of friction Reynolds number, Re_τ. Symbols represent values of XG concentration; arrow indicates increasing XG concentration; black line represents maximum drag reduction according to [74].

%XG	0.01	0.05	0.075	0.10	0.2
LDR	0.13	0.30	0.39	0.44	0.61

Table 3.2: Value of dimensionless parameters used to assesss [31] correlation. $El_0 = 0.087$ for all %XG concentrations.

model equations) using P-K coordinates. The agreement between our data

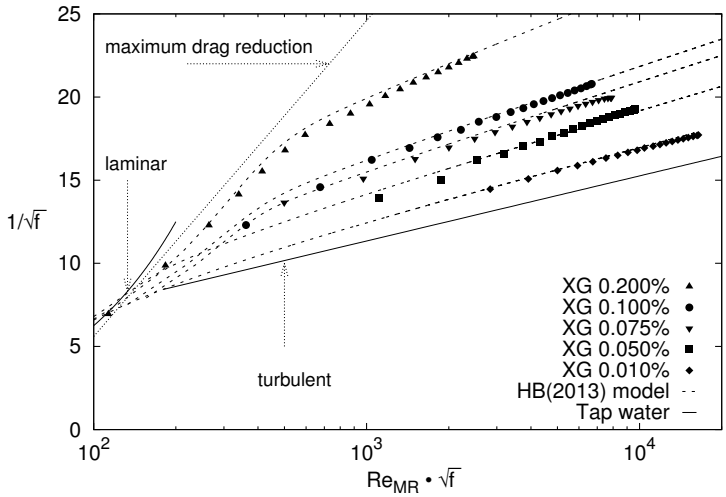

Figure 3.8: Comparison between experimental data and predictive correlation by [31]: solid symbols identify data for different XG solutions; dotted lines identify Housiadas and Beris (HB2013) correlation prediction; curve for tap water (solid line) and maximum drag reduction asymptote (dotted line) are shown for reference.

and the correlation is very good: maximum deviation is 3.5% for 0.1%XG at $Re_{MR}\sqrt{f} \simeq 700$.

3.2.4 Scale up and scale down of friction factor data using experimentally fitted predictive correlation

In figure 3.9 we show how the correlation by [31] can be used to predict the value of friction factor in pipes of different size ($D = 0.005$, 0.25, 0.5 and 1 m) for a given visco-elastic fluid ($0.2\%XG$ solution in our example). The two key dimensionless parameters, LDR and El_0, fitted from our experimental data, are modified as follows for scaling purposes: we keep fixed the value of LDR, since it depends only on polymer concentration; for each pipe diameter D, we rescale the zero shear rate elasticity value $El_0 = 0.087$ calculated from our experimental data (corresponding to $D_0 = 0.1\ m$), as $El_0(D) = El_0(D_0) \cdot (D_0/D)^2$.

The elasticity parameter controls the onset of drag reduction (the higher El_0 the earlier the onset) and increases as the pipe size is reduced [31]. Two main effects are apparent from the analysis of figure 3.9: *i)* the value of friction Reynolds number at onset of drag reduction increases with pipe diameter; *ii)* the MDR asynthote is early reached in small pipe diameters.

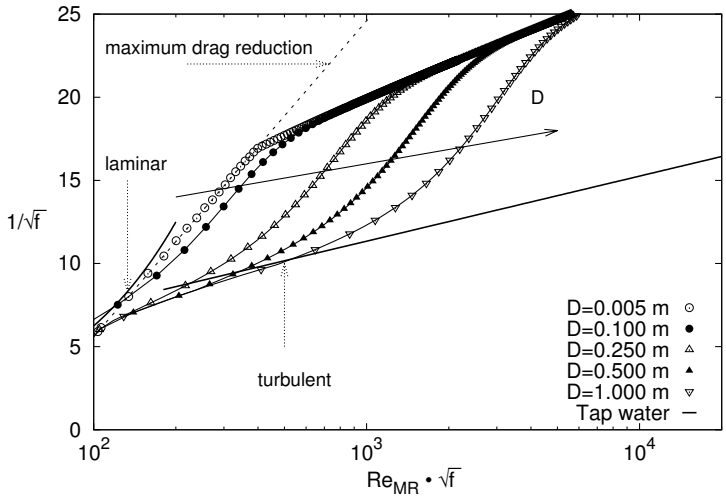

Figure 3.9: Scale up and scale down of friction factor predicted by [31] correlation: curve for tap water (solid line), maximum drag reduction asymptote (dotted line), data for different pipe diameters (solid symbols).

Housiadas and Beris [31] remark the difficulty in obtaining precise values for λ^* (and therefore El_0) *a priori* based on the rheological characterization of the fluid. It is also clear that information about the scale for polymer relaxation time can not be derived from tests performed in small pipe diameter, where the onset Re_τ can be well below the minimum friction Reynolds number for which tests can run. The scaling shown in figure 3.9 suggests that experiments performed at intermediate scales (larger than the laboratory scale and yet not as large as the typical industrial applications) could be profitably used to derive the two key parameters (i.e. the time scale for the polymer relaxation and the limiting value of drag reduction) necessary to scale-up (or scale-down) friction factor data to any other scale of interest.

3.2.5 Housiadas and Beris [31] predictive correlation

The input dimensionless parameters to derive the values of $(Re\sqrt{f}, 1/\sqrt{f})$ pairs shown in figure 3.8 are El_0 and LDR whereas We_τ is the independent variable. For each value of We_τ, we use (1) the universal fitting curve and the value of LDR to calculate the drag reduction, DR

$$\frac{DR}{LDR}(We_\tau) = \begin{cases} 0 & \text{if } We_\tau < We_\tau^{onset} \\ 1 - \frac{2}{1+\exp\left(\frac{We_\tau - We_\tau^{onset}}{\Delta We_\tau}\right)} & \text{if } We_\tau \geq We_\tau^{onset} \end{cases} \quad (3.14)$$

and (2) the rheological constitutive equation to calculate the wall dynamic viscosity normalized to the zero shear rate viscosity

$$\mu_w = \frac{\eta}{\eta_0} = \frac{\eta_\infty}{\eta_0} + \left(1 - \frac{\eta_\infty}{\eta_0}\right) \frac{1}{[1 + (\Omega \cdot We_\tau)^a]^{n/a}} \tag{3.15}$$

where $\Omega \cdot We_\tau = \gamma\lambda$ and $\Omega = \lambda/\lambda^*$. The value of μ_w is used (3) to calculate the zero shear rate value of Weissemberg number, $We_{\tau,0} = We_\tau \cdot \mu_w$, (4) the zero shear rate friction Reynolds number ($Re_{\tau,0} = \rho u_\tau R/\eta_0$) from El_0

$$Re_{\tau,0} = \left(\frac{We_{\tau,0}}{El_0}\right)^{1/2} \tag{3.16}$$

and (5) the friction Reynolds number, $Re_\tau = Re_{\tau,0}/\mu_w$. Then, starting from the initial guess for $\tilde{n} = 1.18$, we calculate (5) the bulk Reynolds number

$$\begin{aligned} Re = &\frac{2\sqrt{2}Re_\tau}{(1-DR)^{\tilde{n}/2}} \cdot \\ &\cdot \left(1.7678 \ln(2\sqrt{2}Re_\tau) - 0.60 - \frac{162.3}{2\sqrt{2}Re_\tau} + \frac{1586}{2\sqrt{2}Re_\tau}\right) \end{aligned} \tag{3.17}$$

(6) a new value for $\tilde{n}$

$$\tilde{n} = 1 + \frac{1.085}{\ln Re} + \frac{6.538}{(\ln Re)^2} \tag{3.18}$$

iterating (5) and (6) up to convergence. Finally, we calculate (7) the friction factor as

$$f = 8\frac{Re_\tau^2}{Re^2} \tag{3.19}$$

From our experimental data for 0.2% XG, the value of $Re\sqrt{f}$ at the onset of drag reduction (open triangle in fig. 3.8) is 142.69, from which we calculate $Re_\tau = 50.44$ and $\mu_w = 0.0269$. Since $We_\tau = 6$ at onset and $El_0 = We_\tau/(Re_\tau^2\mu_w)$, we calculate $El_0 = 0.087$.

3.3 Cost-effective use of drag reducing agents

3.3.1 Drag reduction

In industrial practice, the effectiveness of a polymer as drag reducing agent (DRA) is described by the drag reduction level, %DR, which is a function of the friction factor. Many different definitions of drag reduction have been used in the literature (see Eq. (3.9), (3.13) and (3.20)). All of them are related and can be calculated from (Re, f) pairs available from experiments. In this work, we choose to define drag reduction as the change in pressure drop (or wall shear stress) due to the presence of the polymer to the original

Newtonian value, while keeping the same mean flow rate [64, 76] (see Eq. (3.9)). This definition states clearly the link between the industrial target, i.e. the transport of a given amount of fluid along a pipeline, and the benefit possibly produced by drag reduction, i.e. energy savings due to a smaller pressure loss. When the density and viscosity of the polymeric solution do not change significantly with the polymer addition, our definition is equivalent to

$$\%DR_{Re} = \left.\frac{f_w - f_p}{f_w}\right|_{Re=const} \cdot 100 \tag{3.20}$$

where the difference in friction factors is evaluated keeping the Reynolds number constant [18, 30].

Figure 3.10 shows $\%DR_Q$ evaluated by Eq. (3.9) as a function of bulk velocity, u (as in [25]). Since experimental measurements of pressure drop for XG solution and water are not available at the same flow rate, Eq. (3.3) and (3.4) are used to calculate the friction factor of the tap water flowing at the same flow rate (and velocity) of the polymer solution. For 0.01%

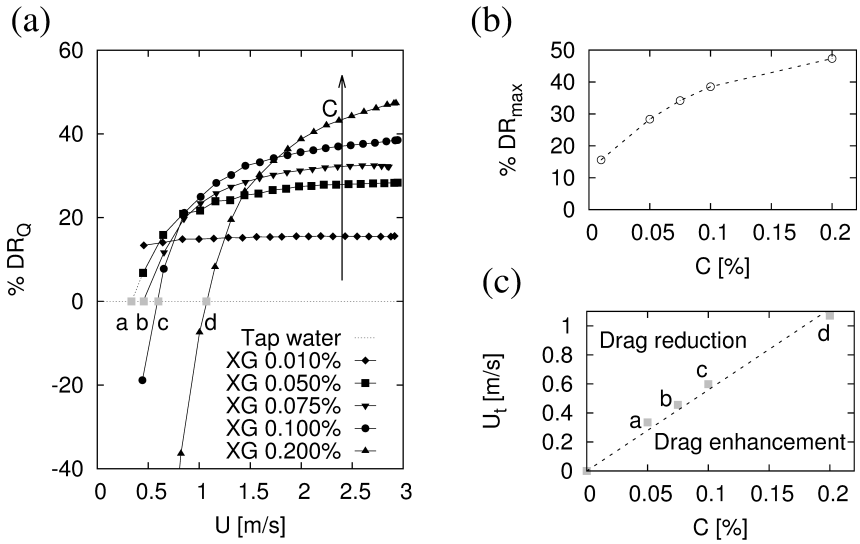

Figure 3.10: (a) Percent drag reduction for aqueous solutions at different XG concentrations as a function of bulk velocity in the pipe, u. Symbols represent values of XG concentration. Arrow indicates increasing XG concentration. (b) Variation of maximum %DR, $\%DR_{max}$, as a function of XG concentration, C: the increment in %DR is less than linear with C. (c) Variation of threshold velocity for drag reduction, u_t, as a function of polymer concentration, C, and linear fit (dashed line).

XG solution, the drag reduction is almost constant in the entire range of

velocities investigated. For any XG concentration greater than 0.01%, the profile of $\%DR_Q$ increases with bulk velocity, eventually reaching a plateau. Figure 3.10b shows the maximum value of $\%DR_Q$, $\%DR_{max}$, obtained for each XG concentration. Similarly to the analysis presented by [47] for Polyox, $\%DR_{max}$ increases with XG concentration, but less than proportionally to the amount of polymer added, C. Figure 3.10a shows also that, for any XG concentration greater than 0.01%, we can identify a threshold value of bulk velocity in the pipe, u_t, above which drag reduction is produced (i.e. $\%DR_Q > 0$). Since the polymer is semi-rigid, this threshold velocity should not be associated with a coiled/stretched transition. Rather, it should be considered as an indicator of the level of Newtonian shear rate above which the conformational change is such that the homogeneous increase in the effective viscosity is counterbalanced by the reduction of momentum flux to the wall in the near wall layer [1, 55]. Figure 3.10c shows the value of u_t, interpolated/extrapolated from data in figure 3.10a and labelled with letters. The threshold bulk velocity seems to increase almost linearly with polymer concentration (dashed line in fig. 3.10c) in the range of values investigated. These results are consistent with Direct Numerical Simulations [51] which indicate that the onset of drag reduction is observed when the Weissemberg number exceeds a (constant) threshold value. Considering that λ^* depends primarily on molecular characteristics [31], the onset condition corresponds to increasing values of friction, u_τ and bulk velocity, u, for increasing concentration of XG in solution (and larger ν).

Figure 3.10c indicates that, if we consider a reference bulk velocity equal to 1 m/s as the target for the economical transport of fluid along pipelines, the addition of XG at any concentration (among those tested) lower than 0.2% will produce some drag reduction. According to figure 3.10a, the %DR expected by 0.05%, 0.075% or 0.1% XG is about the same at this velocity. The effect the relative amount of polymer added has on %DR is best appreciated when the fluid velocity increases up to $2 \div 3$ m/s (i.e. at larger Re numbers, moving into the LDR region).

3.3.2 Cost-effectiveness analysis

Figure 3.11a shows isocontours of $\%DR$ (dotted lines, step 2%, starting from zero to 46%, labelled in gray) obtained from our tests. Similar data could be obtained for pipes of different diameter using the design equation discussed in section 3.2.4. Isocontours are drawn for velocity in the range $u = [0 \div 3\ m/s]$ and $\%XG = [0 \div 0.2]$. We do not extend $\%DR$ isocontours in the lower left region of the graph ($u < 0.35\ m/s$ and $C < 0.01\%XG$), since we have no experimental data there. In the top left corner region (high concentration, low velocity), the polymer does not produce drag reduction (drag enhancement region). At large enough velocity (i.e. into the LDR region), drag reduction becomes almost independent of velocity and increases with polymer concentration.

Isocontours of $\%DR$ alone are not enough to evaluate if the use of the drag reducing polymer may represent a cost-effective alternative for the transport of fluid along a piping system. Our evaluation will be based on a cost-effectiveness analysis which builds up on the following assumptions: *i)* the piping system is already installed (initial investment costs for pump and pipe equipments are neglected); *ii)* the concentrated pressure drop due to bends, elbows, fittings and valves has been adequately represented as distributed pressure drop generated by (properly defined) equivalent pipe lengths; *iii)* mechanical degradation of the polymer during the transport of fluid has negligible effect on pressure drop. These represent conservative assumptions for the identification of threshold operative conditions in which the polymer addition can be considered cost effective. The operating costs we are supposed to pay to convey the fluid are *i)* the pumping costs and *ii)* the polymer additive cost and can be conveniently referred to the unit of mass of fluid to be conveyed. We define the percent net savings, %S, as

$$\%S = 100 \cdot \frac{C_w - C_p}{C_w} \ [\%] \tag{3.21}$$

where C_p and C_w are transport costs per unit mass with/without the DRA. C_w can be calculated as the product of the price of energy times power and working hours divided by the mass of fluid conveyed

$$C_w = \frac{K_E \Delta p_w Q N_h}{\rho Q N_h} \ [€/kg] \tag{3.22}$$

where K_E is the price of energy, $[€/kWh]$, Δp_w is the pressure loss, $[Pa]$, Q is the flow rate, $[m^3/h]$, N_h is the number of pump working hours, $[h]$, and ρ is fluid density, $[kg/m^3]$. C_p can be calculated as the product of the price of energy times power and working hours plus the price per unit mass of polymer times the mass of polymer, divided by the mass of fluid conveyed

$$C_p = \frac{K_E \Delta p_p Q N_h + K_P \cdot \%XG \rho Q N_h}{\rho Q N_h} \tag{3.23}$$

where Δp_p is the pressure loss with the DRA, $[Pa]$, $\%XG$ is the concentration (w/w) of DRA, $[kg_p/kg]$, K_P is the price of DRA per unit mass, $[€/kg_p]$. Considering that $\Delta p_p = (1 - \%DR_Q)\Delta p_w$ (from Eq. 3.9) and $\Delta p_w = 2 f_w L \rho u^2 / D$, Eq. (3.21) becomes

$$\%S = \%DR_Q - \frac{K_P}{K_E} \frac{\%XG}{2 f_w u^2 L/D} = \%DR_Q - \frac{1}{\alpha} \frac{\%XG}{2 f_w u^2} \ [\%] \tag{3.24}$$

where $\alpha = K_E/K_P \cdot L/D$ $[s^2/m^2]$ or $[kg/J]$ is a dimensional factor which depends on the prices (of energy and polymer) and on pipeline characteristics (L/D). In short, $\%S = F(u, \%XG, \alpha)$. The use of the DRA is cost-effective only if $\%S > 0$. The largest is the value of $\%S$, the most cost-effective is the use of the polymer.

In figure 3.11a-d we show positive isocontours of $\%S$ (continuous lines, step 2%, starting from zero). The color scale (from red, bottom to pale blue, top) identifies increasing values of $\%S$. Subfigures (a)-(d) show the variation of $\%S$ isocontours calculated for different values of the parameter α.

Values of α may be associated with different values of energy/polymer price ratio or with pipelines characterized by a different L/D ratio. In this work, we assume the price of energy is $K_E = 0.15$ €$/kWh$, the price of polymer is $K_P = 10$ €$/kg$, and pipe size is $D = 0.1$ m. The values of α considered in figure 3.11 correspond to pipeline 120, 240, 600 and 1200 km long (values comparable with ductworks in small to large cities).

Figure 3.11 can be used to identify if the polymer addition represents a cost-effective solution for a given pipeline scenario or not. Assume that the task is to transport fluid at $u = 2$ m/s along the pipeline. In the scenario shown in figure 3.11a, the most cost effective option, identified by the circle, is to use no polymer. Even if drag reduction up to 38% can be achieved using 0.2% XG, this would not produce net savings because the polymer cost would be larger than savings obtained in pumping cost. In the scenario shown in figure 3.11b, i.e. a bit longer pipeline or a different economical scenario in which the price of energy is larger and savings on pumping costs can be more significant, the most cost effective option would be to add polymer at small concentration (e.g. 0.03% XG) to obtain about 18% drag reduction and 7% net savings. In the third scenario, shown in figure 3.11c, the most cost effective option would be to add polymer at larger concentration (e.g. $\simeq 0.1\%$ XG) to obtain up to 32% drag reduction and more significant net savings (about 20%). Finally, in the fourth scenario, shown in figure 3.11d, the most cost effective option would be to add a bit more polymer (concentration about 0.125% XG) to obtain up to 26% net savings.

3.4 Discussions

In this work, we build a self-consistent data base measuring Δp versus Q for different aqueous solutions of XG (Xantural 75 at 0.01, 0.05, 0.075, 0.1 and 0.2% w/w XG) in an industrial size rig (100 mm ID). The data set includes the rheological characterization of aqueous XG solutions used for testing and drag reduction data measured at different Reynolds number (from 758 to 297 000) for five XG concentrations (in the dilute and semi-dilute polymer concentration region). The data set, representing a homogeneous source of experimental data gathered on a large pipe, has been used for the validation of existing predictive correlations.

We validated our experiments by direct comparison with data by [20] who performed experiments at the same scale, in the same pipe geometry. Deviations are 4-7% and are most likely associated with non constant properties of the different XGs commercially available. We assesssed also the

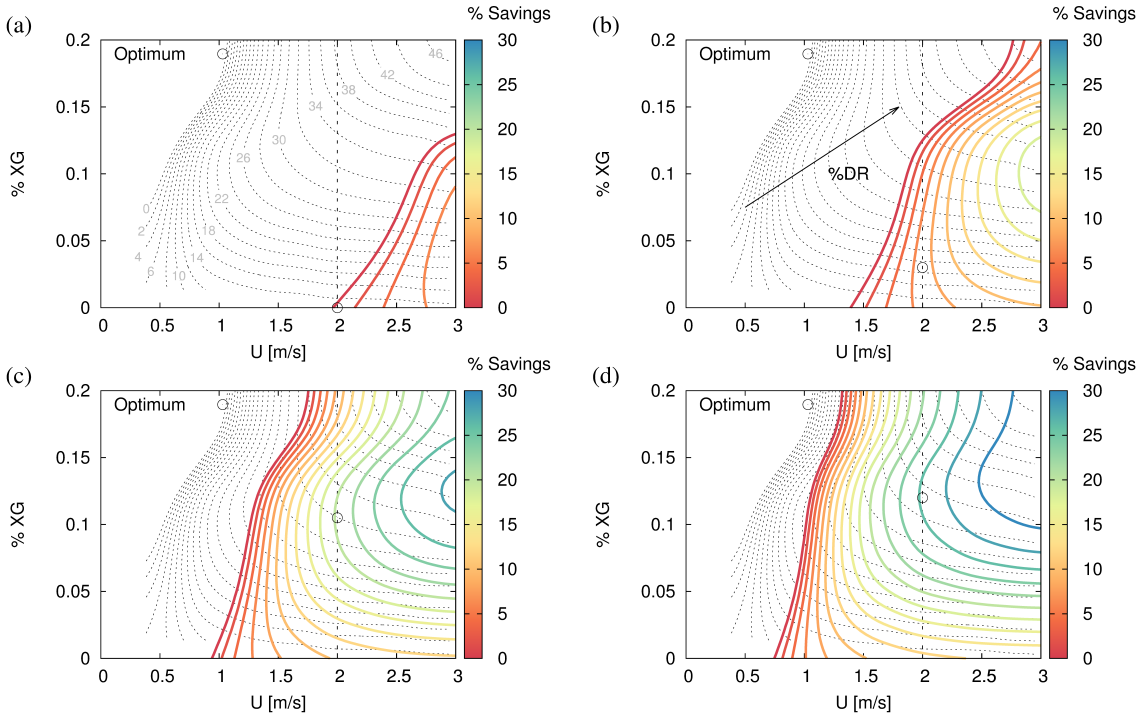

Figure 3.11: Percent net cost savings expected from use of XG as drag reducing agent: dashed lines on the background represent isocontours of $\%DR$ (starting from zero, step 2%; isocontour labels are in gray);continuous lines (in color on-line) represent isocontours of $\%S$ (starting from zero, step 2%); subfigures correspond to different pipeline scenario: (a) $\alpha = 5 \cdot 10^{-2}\ s^2/m^2$, (b) $\alpha = 1 \cdot 10^{-1}\ s^2/m^2$, (c) $\alpha = 2.5 \cdot 10^{-1}\ s^2/m^2$, (d) $\alpha = 5 \cdot 10^{-1}\ s^2/m^2$.

possibility of scaling up drag reduction data from experiments performed at a smaller scale or on different pipe geometries. Drag reduction data collected in laboratory scale rigs [3] and scaled up to the larger scale of our test rig shows deviation of the friction factor in the range $7 \div 12\%$. Drag reduction data collected in pipe with rectangular [18] or annular [38, 39] cross sections shows deviation in the range $7 \div 8\%$. We used our data to confirm the validity of the design equation proposed by [31], demonstrating also the capability of their model to scale up (or scale down) our drag reduction data to any larger (smaller) scale of interest. By the cost-effectiveness analysis proposed we identify sets of working conditions for the profitable use of XG polymer as DRA. We show that, for each industrial scenario, the most cost-effective option for the use of XG should be identified based on the joint analysis of *i)* $\%DR$ data evaluated at different bulk velocity and for solutions at different $\%XG$ concentration and of *ii)* the value of the cost parameter α, combining data on energy/polymer prices with the specific pipeline characteristics.

4

Drag reduction by synthetic polymers

4.1 Introduction

In this chapter the results obtained investigating polymer drag reduction by means of PEO and HPAM solutions, will be presented. Differently from the experiments discussed in chapter 3, in this case the polymer has been injected directly at the pipe wall (see section 2.2.3). In figures 4.1 and 4.2, typical trends of the acquired raw data are shown: as can be seen, starting from a steady-state pure solvent flow, once the polymer injection starts and the polymer effect is felt in the measurement section, the pressure drop decreases according to the *in-situ* polymer concentration; the higher the concentration, the higher the drag reduction effect. Once the injection is stopped, the pressure drop returns to the pure solvent value (see figs. 4.1b and 4.2b). After each injection, the solution was allowed to flow for a couple of minutes to obtain complete degradation of the polymer present in the solvent (mainly due to the pump's shear). Before starting a new test, the pure solvent pressure drop was compared with the results obtained when just pure water was used, to assess the flow conditions. Moreover, single pass-through test were also performed and compared with the recirculating results giving no difference in the drag reduction values; this means that the polymer was completely degraded by the action of the pump and no cumulative drag reduction effects were present.

Rheological characterization has been conducted also for these polymer solutions but, due to the very small concentrations adopted, it has been verified that the viscosity of each solution tested can be assumed equal to the one of the pure solvent at the test temperature.

In figure 4.1 the signals acquired by two consecutive pressure transducers are shown for 5 ppm polymer concentration and two bulk velocities. It is interesting to notice that there is a temporal delay in the drag reduction effect and it has been verified, that this delay is proportional to the bulk velocity. Comparing figures 4.1a and 4.1b it can be seen that the delay is reduced with increasing the bulk velocity. In figure 4.2 it can be noticed that with increasing the bulk velocity, increases the difference between the

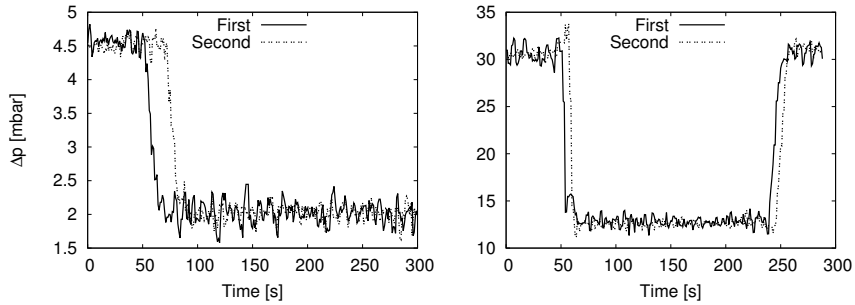

Figure 4.1: Temporal series of pressure drop raw data for PEO 308 in 30 mm pipe at 5 ppm. Signals acquired from two differential pressure transducers: the first and second downstream the inlet. (a) $u_b = 1\,m/s$. (b) $u_b = 3\,m/s$.

effects of polymer concentration.

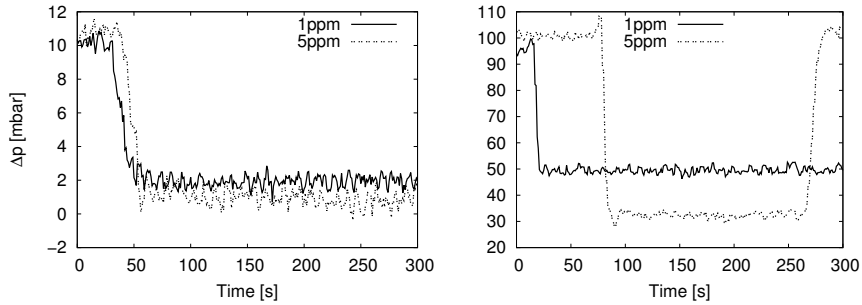

Figure 4.2: Temporal series of pressure drop raw data for PEO 308, 30 mm pipe, at different bulk velocities, for 1 and 5 ppm. (a) $u_b = 1\,m/s$. (b) $u_b = 3\,m/s$.

Starting from the temporal series, the average values of the pressure drop and the flow rate have been calculated and used to present the results as $\Delta p\,vs\,Q$ and *Prandtl-Kármán* coordinates. Pressure drop results are first compared with the von Kármán law for Newtonian flows in the $\Delta p\,vs\,Q$ plots and also with the Virk's MDR asymptote in *P-K* coordinates. Finally, plots of percent drag reduction, as a function of the bulk velocity, are presented.

4.2 Drag reduction by *Polyethylene oxide*

4.2.1 30 mm pipe

In this section the results for the PEO 301 and 308 are presented. Five concentrations have been tested for this pipe diameter: 0.25, 0.5, 1, 5 and 10 ppm, for both molecular weights. The maximum flow rate was limited to $Q \simeq 13\,m^3/h$ due to the maximum flow rate which can be injected by the polymer injection system (refer to section 2.2.3 for details).

In figure 4.3 the pressure drop results are presented for both molecular weights. As expected the pressure drop decreases with increasing polymer concentration and bulk velocity. The PEO 308 (compare fig. 4.3b with fig. 4.3a), due to its higher molecular weight, is more effective than PEO 301. A better representation is obtained with the *Prandtl-Kármán* coordinates as shown in figure 4.4.

It can be seen that, increasing the polymer concentration the results are moving toward the MDR asymptote; for a given Reynolds number the higher molecular weight (see fig. 4.4b) determines a more effective drag reduction result. The experimental data show that departure from the von Kármán law is faster (i.e. has a larger slope) with increasing polymer concentration. At a given concentration, especially above 1 ppm (see fig. 4.4b), beyond a certain value of the friction Reynold number, the line connecting the experimental results bends toward the von Kármán law. As will be discuss later on, this behaviour is due to the mechanical degradation of the polymer chains when subjected to high values of shear rate. Extrapolating the trend of data in the lower range of $Re\sqrt{f}$ it can be noticed that the departing point from the von Kármán law for the higher molecular weight occurs at lower values of the friction Reynolds number than for the PEO 301.

In figure 4.5 percent drag reduction (%DR) is presented as a function of the bulk velocity for both PEO 301 and 308 and compared to the Virk's maximum expected value. As already stated in section 3.3.1 there are different methods to evaluate the percent drag reduction; as previously done for the Xanthan Gum results also here a more industrial-like approach is considered, calculating the drag reduction as the change in the pressure drop, due to the presence of the polymer, with respect to the pure Newtonian flow, at the same mean flow rate (refer to Eq. (1.19)) [64, 76]. As expected from the previous plots the strong effect of the molecular weight on drag reduction is clearly depicted, especially at high concentration. For example, if we consider the 5 ppm results, for the PEO 308 the drag reduction is 20 % higher than in PEO 301. With increasing the bulk velocity, the degradation of the polymer chains results in a decreased drag reduction percentage.

To assess the validity of our experimental results, comparison has been done against data available in literature. In figure 4.6 our results for PEO 308 are compared with those from Elbing *et al.* [17]. The pipe diameter used in [17] was slightly smaller than ours (27 mm) so higher values of drag

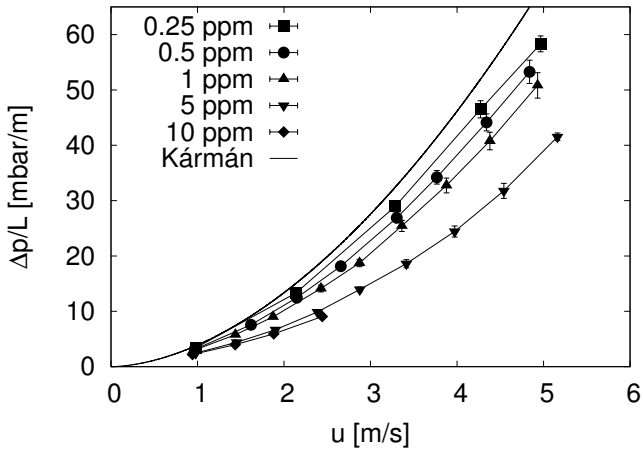

(a)

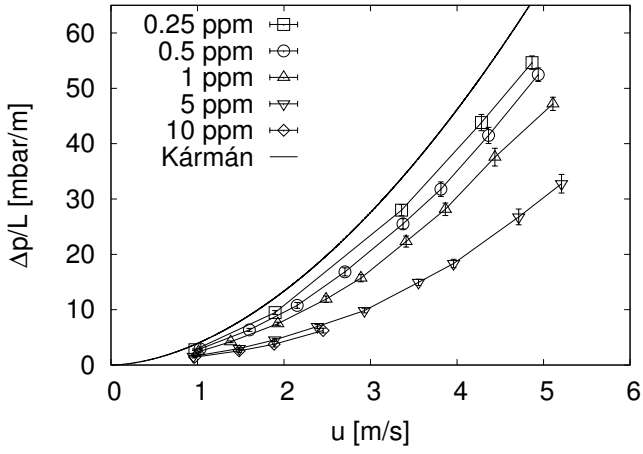

(b)

Figure 4.3: Pressure drop per unit length results as a function of the bulk velocity in the 30 mm pipe for (a) PEO 301 and (b) PEO 308.

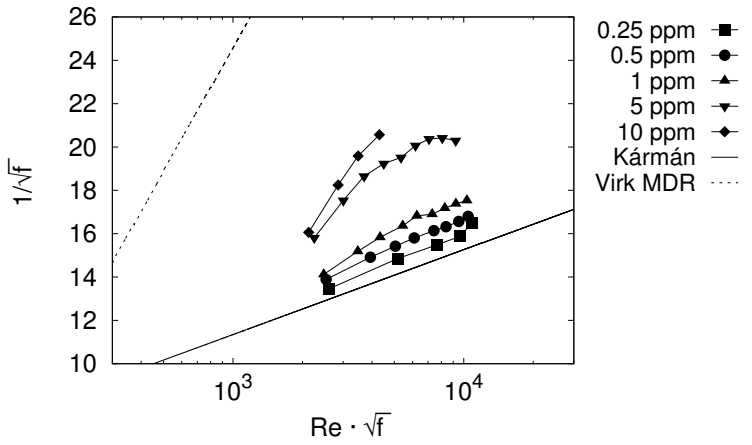

(a)

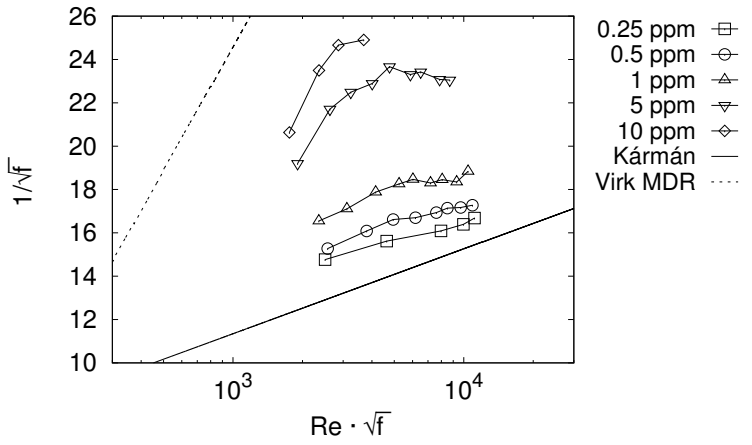

(b)

Figure 4.4: Friction factor results in Prandtl-Kármán coordinates in the 30 mm pipe for (a) PEO 301 and (b) PEO 308.

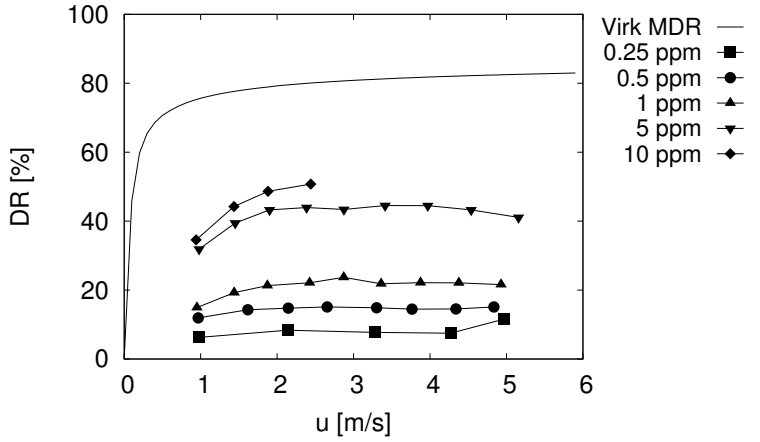

(a)

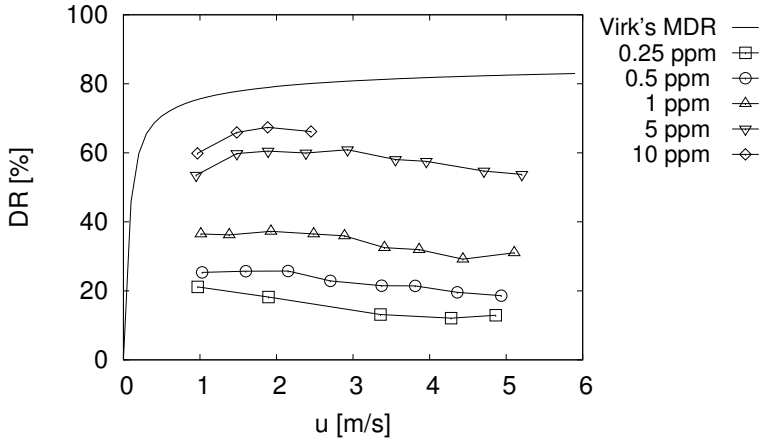

(b)

Figure 4.5: Percentage drag reduction aa a function of the bulk velocity in the 30 mm pipe for (a) PEO 301 and (b) PEO 308. Solid line represents Virk's MDR.

reduction are expected. It can be seen that a general good agreement is reported; in figure 4.6a the results from [17] are slightly higher, maybe due to the smaller pipe size while in figure fig. 4.6b it is interesting to notice that a similar degradation effect is present. Moreover, in [17] dechlorinated water has been used to avoid polymer degradation by chlorine; in our case tap water has been used, and this condition may have an influence on the results.

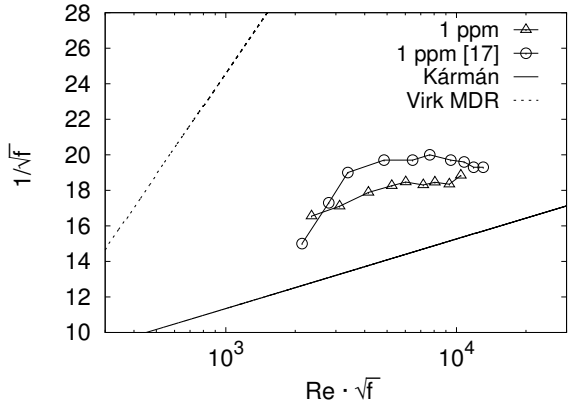

(a)

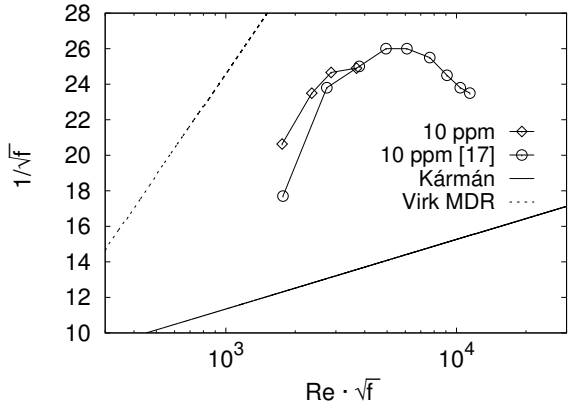

(b)

Figure 4.6: Friction factor results in the 30 mm pipe for PEO 308. Comparison against data in Elbing *et al.* [17] for 1 and 10 ppm.

4.2.2 50 mm pipe

In this section the results for PEO 301 and 308 in the 50 mm pipe are presented. Four concentrations have been tested for this pipe diameter: 0.25, 0.5, 1, 5 for both molecular weights. In this case it was not possible to reach the concentration of 10 ppm due to limitations in the capacity of the injection system (refer to section 2.2.3 for details).

In figure 4.7 pressure drop results are presented for both molecular weights. The overall behaviour is like the one depicted for the 30 mm pipe with the pressure drop decreasing with increasing polymer concentration and bulk velocity. In figure 4.8 the friction factor results are presented in *P-K* coordinates. Figure 4.8a shows that for this set of tests, the onset condition can be clearly identified. For a given molecular weight and pipe diameter, the onset point is independent on polymer concentration. Comparing the results of the two molecular weights, it is again evident that a higher molecular weight corresponds to a higher level of drag reduction. It is also interesting to notice that, for this pipe diameter, the degradation effect at high values of the friction Reynolds number is less pronounced, or even not present, with respect to the 30 mm pipe. Due to the limitations is the injection system no higher values of the Reynolds number could be explored.

The same trend can be deduced from figure 4.11 where percent drag reduction is presented with respect to the bulk velocity: percent drag reduction increases with increasing polymer concentration; at a given concentration, the molecular weight plays a relevant role in the drag reduction effectiveness.

As previously done for the 30 mm pipe, comparison against some available literature results has been made. In figure fig. 4.10 our experimental data is compare with the results from Hoyt *et al.* [32]; even if the pipe diameter is slightly different (53 mm instead of 50) and the explored Reynolds numbers are higher, it can be seen the there is good agreement between the two sets of data. The results from [32] are obtained using a thread polymer conformation, rather than an homogeneous one; as reported also by other authors (see [79] among other) polymer thread drag reduction has been demonstrated to be more effective than pre-mixed homogeneous conditions.

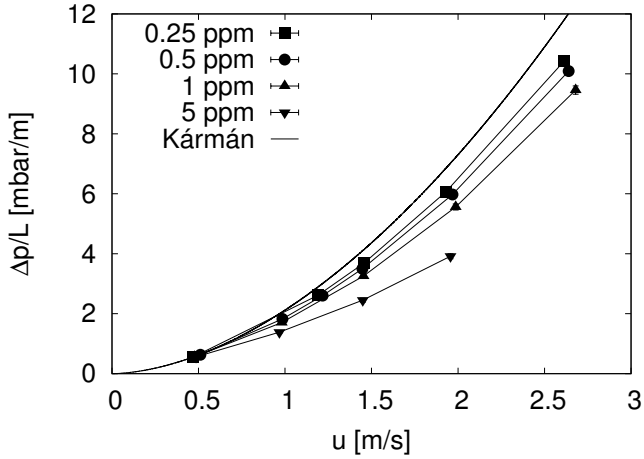

(a)

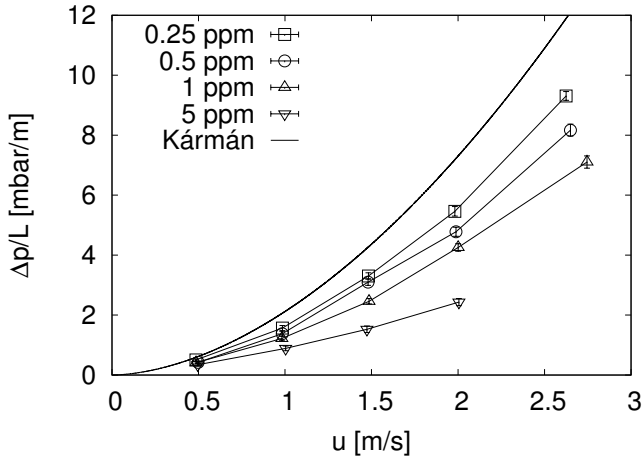

(b)

Figure 4.7: Pressure drop per unit length results as a function of the bulk velocity in the 50 mm pipe for (a) PEO 301 and (b) PEO 308.

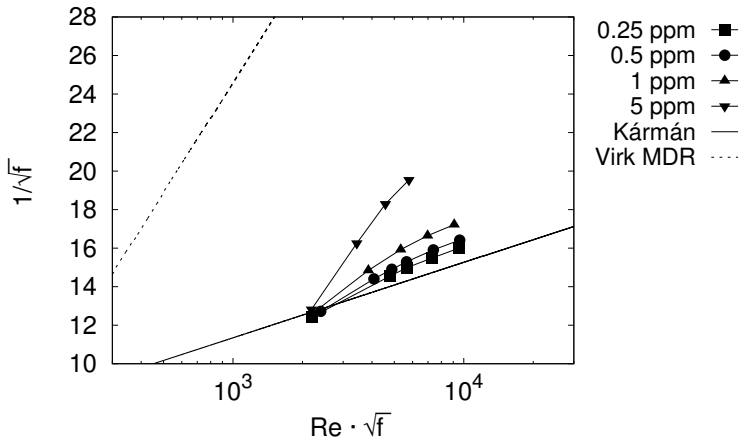

(a)

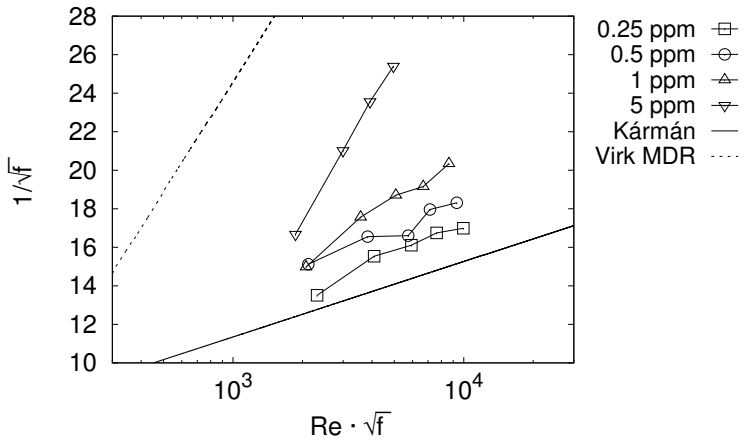

(b)

Figure 4.8: Friction factor results in Prandtl-Kármán coordinates in the 50 mm pipe for (a) PEO 301 and (b) PEO 308.

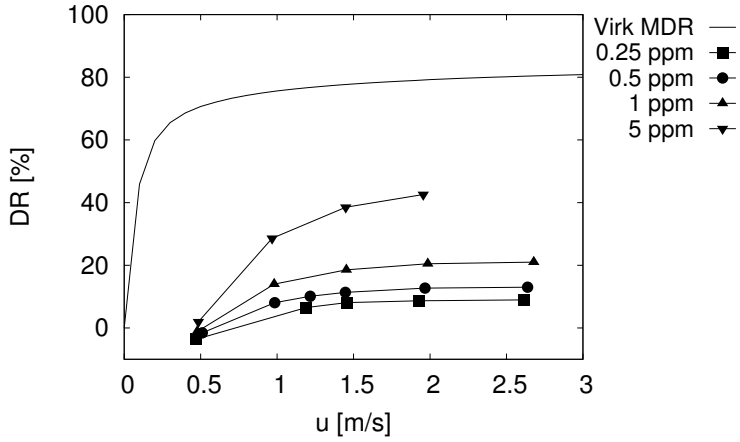

(a)

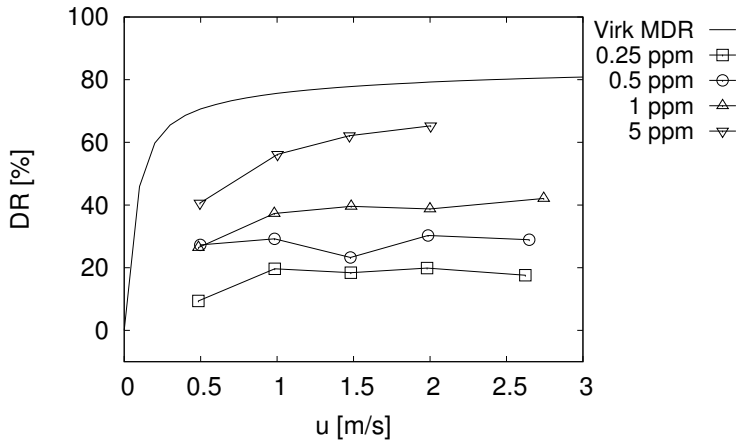

(b)

Figure 4.9: Percentage drag reduction as a function of the bulk velocity in the 50 mm pipe for (a) PEO 301 and (b) PEO 308. Solid line represents Virk's MDR.

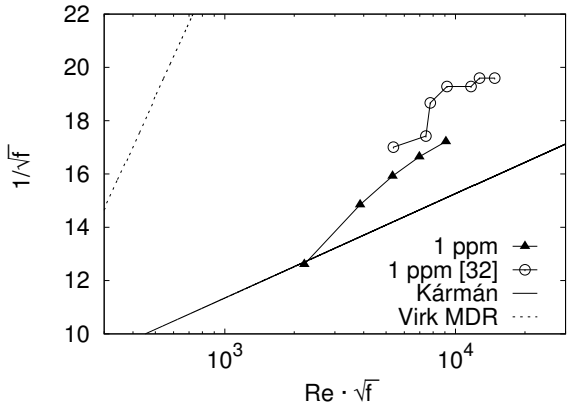

Figure 4.10: Friction factor results in the 50 mm pipe for PEO 301. Comparison against data in Hoyt *et al.* [32] for 1 ppm.

4.2.3 100 mm pipe

Some preliminary tests with the PEO 308 have been conducted also on the 100 mm pipe. Both homogeneous preparation and injection of the polymer have been tested. In the first case (not shown) no drag reduction has been registered, mainly due to the degradation within the centrifugal pump (as also ascertained in the smaller pipes). More interesting results were obtained when the injection method has been adopted. In figure 4.11a the pressure drop per unit length is shown: the drag reduction is significant even for very low polymer concentrations. In figure 4.11b the friction factor results are presented in *P-K* coordinates: high values of drag reduction are obtained; the flat behaviour of the results with increasing friction Reynolds number may indicate the occurrence of chains degradation. Percentage of drag reduction is presented in figure 4.12 as a function of the bulk velocity.

4.2.4 PEO degradation and drag reduction prediction

The theory of polymer degradation proposed by [72] and already discussed in section 1.2.2 has been applied to the results obtained during the PEO tests. In figures 4.13, 4.14 and 4.15 the results are presented in two columns: left-hand-side for PEO 301 and right-hand-side for PEO 308. Each row corresponds to a polymer concentration. In each plot, the results at the given concentration and molecular weight are shown for both pipe diameters together with the drag reduction bounds proposed in [72]. The curve named *w contr* refers to the bound determined by the chain degradation due to the high level of shear generated in a generic contraction inside the pipe; the curve named *w/o contr* refers to the degradation due to the shear caused by the turbulent structures present in the flow. As discussed in section 1.2.2

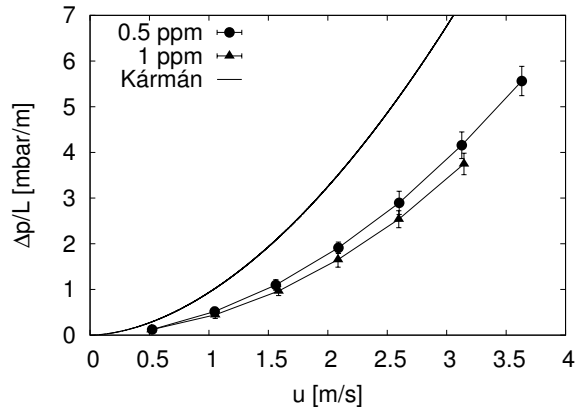

(a)

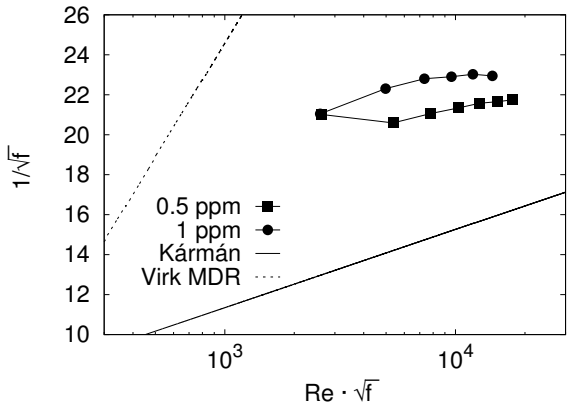

(b)

Figure 4.11: Drag reduction in the 100 mm pipe, PEO 308. (a) Pressure drop per unit length as a function of hte bulk velocity. (b) Friction factor results in P-K coordinates.

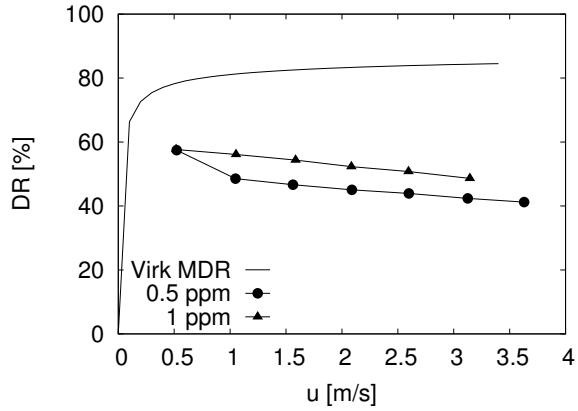

Figure 4.12: Percentage drag reduction as a function of the bulk velocity in the 100 mm pipe for PEO 308. Solid line represents Virk's MDR.

these two curves do not depend on the pipe diameter but only on polymer concentration. The straight line named *Th. slope* represent the theoretical expected slope increase as predicted by Eq. (1.32) presented in section 1.2.2.

All the plots indicate that the drag reduction is in fact limited by polymer degradation well before reaching the MDR asymptote and that there is good agreement between the experimental results and the predicted onset point and slope increase. For the lower molecular weight polymer (all the studied concentrations), the curve representing the degradation by pipe's contraction represents the maximum level of drag reduction achievable: this is consistent with our experimental procedure since the injection of the polymer occurs through a small (2 mm) hole of the injection syringe where high level of shear are generated, especially at high injection flow rates (see for example fig. 4.14 at c=5 ppm). Moreover, for the PEO 301, the trend is independent on the pipe diameter, demonstrating once again that, in the case of a low value of the molecular weight, the degradation mainly occurs due to the high levels of shear in pipe's contractions rather than other shear stress in the pipe.

For PEO 308, the limiting bound is represented by the degradation caused by the turbulent structures present in the flow: polymer molecular weight is large enough to resist to the high levels of shear in a generic contraction but is then degraded by the shear stress caused by the flow structures. This is confirmed by the results obtained in the 50 mm pipe which are not limited by this curve: in the 50 mm pipe the shear stresses are lower the in the 30 mm pipe reducing in this way the degradation of the polymer chains (see fig. 4.14 at c=1 and 5 ppm).

Experimental results are in good agreement with the polymer degradation theory presented by [72]. The procedure proposed by [72] can be profitably used as a practical tool to predict polymer degradation and hence drag re-

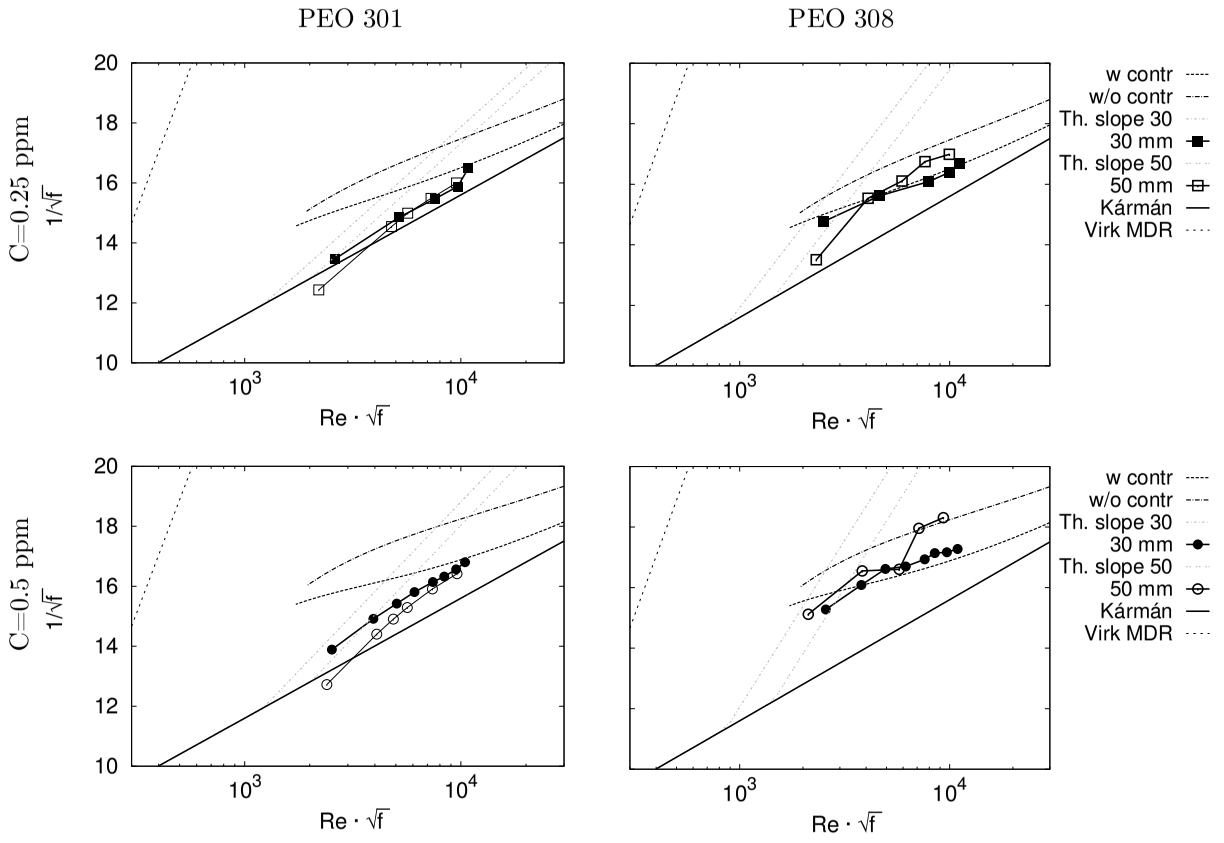

Figure 4.13: Comparison between the PEO results and the degradation bounds proposed by [72]. Left column: PEO 301, right column PEO 308. Concentration is specified at row's left-hand-side.

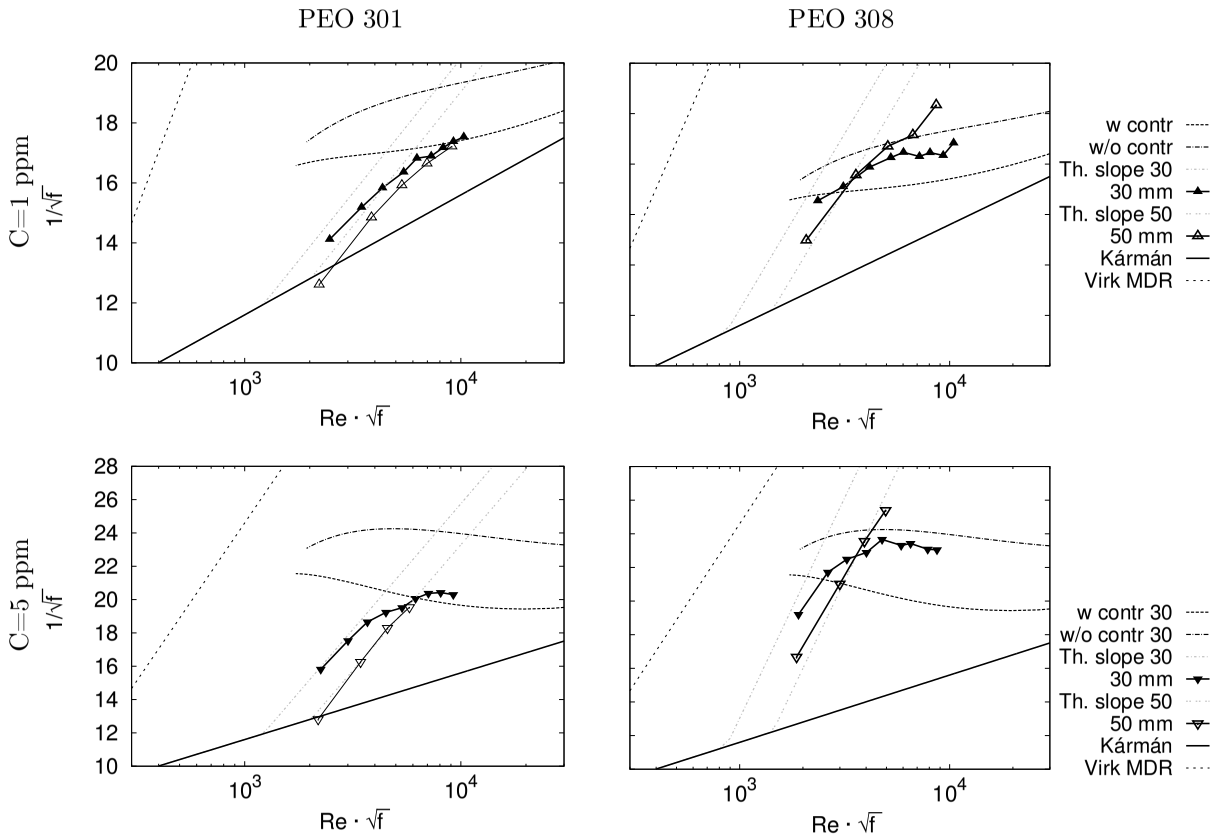

Figure 4.14: Comparison between the PEO results and the degradation bounds proposed by [72]. Left column: PEO 301, right column PEO 308. Concentration is specified at row's left-hand-side.

Figure 4.15: Comparison between the PEO results and the degradation bounds proposed by [72]. Left column: PEO 301, right column PEO 308. Concentration is specified at row's left-hand-side.

duction decrease, as a function of flow conditions and polymer characteristics such as concentration and molecular weight.

4.3 Drag reduction by *Partially Hydrolysed Polyarcylamide* (HPAM)

The concentrations investigated are: 0.25, 0.5, 1 and 5 ppm. In figure 4.16 pressure drop results per unit length are presented for both diameters as a function of the bulk velocity. Pressure drop decreases with increasing polymer concentration and bulk velocity. Figure 4.17 shows that the drag reduction efficiency increases in the smaller diameter, almost approaching the MDR asymptote. It can be also noted that, even if not expected, polymer degradation is strongly present for both pipes and for almost all the concentrations studied; this phenomenon was supposed to be less relevant in HPAM than in PEO. This trend is more evident in figure 4.18 where percent drag reduction is represented as a function of the bulk velocity: %DR starts to decrease for all the concentrations for very low value of the bulk velocity (compare with figs. 4.5 and 4.11).

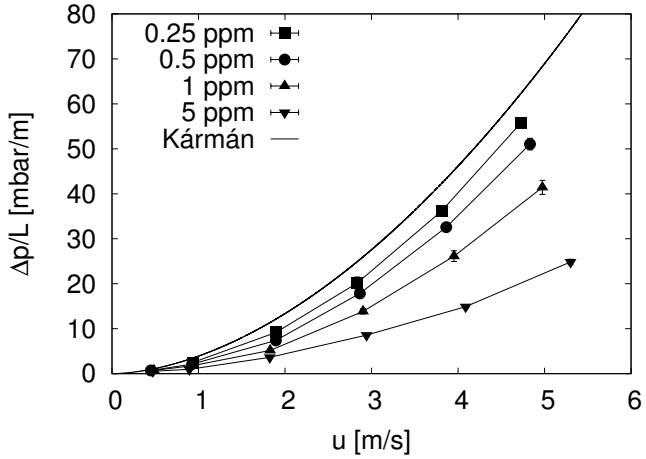

(a)

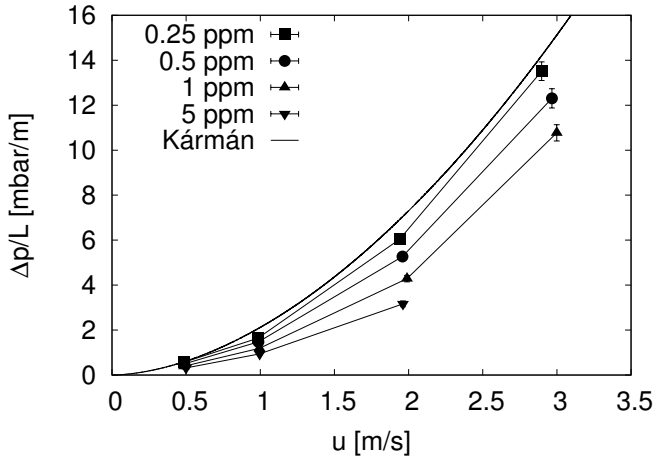

(b)

Figure 4.16: Pressure drop per unit length as a function of the bulk velocity for HPAM solutions in (a) 30 mm pipe and (b) 50 mm pipe.

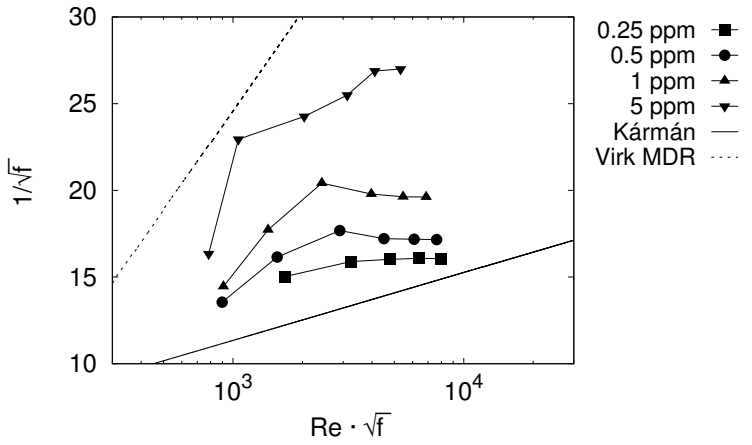

(a)

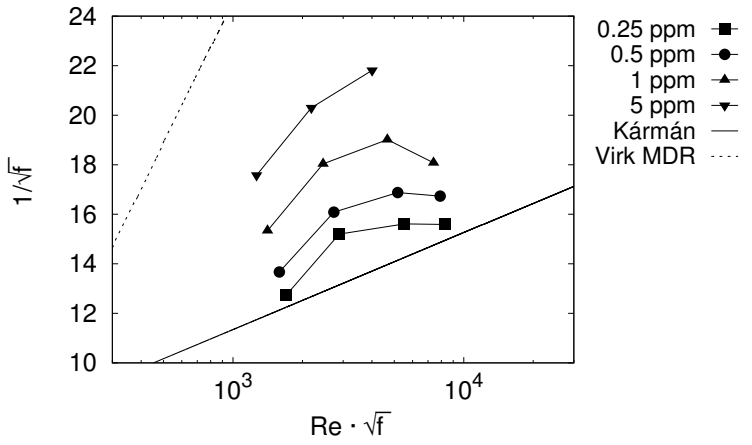

(b)

Figure 4.17: Friction factor results in Prandtl-Kármán coordinates for HPAM solutions in (a) 30 mm pipe and (b) 50 mm pipe.

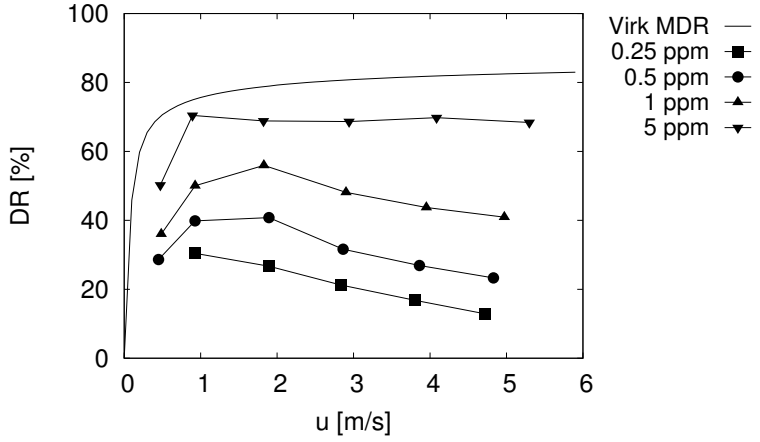

(a)

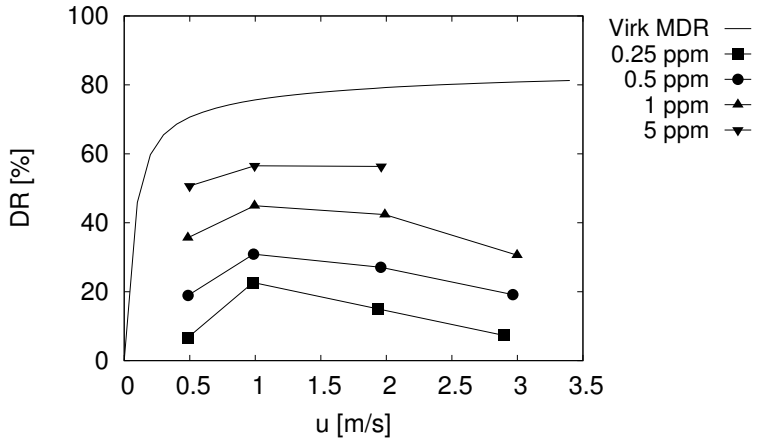

(b)

Figure 4.18: Percentage drag reduction as a function of the bulk velocity for HPAM solutions in (a) 30 mm pipe and (b) 50 mm pipe.

5

Conclusions

In this chapter collected results are summarised considering the objectives introduced in chapter 1.

It has been demonstrated that drag reduction can be obtained using both synthetic and bio-polymers; the latter result it is particularly interesting for all those applications where environmental issues are matter of concern. The main difference that can be deduced from the performed experiments is that the concentrations that should be added to achieve a comparable level of drag reduction are significantly different. In the case of bio-polymers the higher level of percent drag reduction achieved, equal to 60 %, has been obtained with a polymer concentration 4000 times higher than with the PEO 308 for the same pipe diameter (compare figs. 3.7 and 4.12). Moreover, due to the very high concentrations needed, it has been shown by means of rheological characterizations that the medium can not be considered Newtonian anymore. This result has a direct influence on the drag reduction mechanism since, for those high concentrated solutions, viscous effect may overcome elastic effect, modifying the drag reduction mechanism as also suggested by [12].

The interesting characteristic shown by Xanthan Gum solutions is the strong resistance to mechanical degradation: as described in chapter 3, for the XG tests, an homogeneous solution has been used and recirculated many times along the loop, and no mechanical degradation has been recorded despite the high levels of shear encountered in the centrifugal pump. This result should be underlined and more investigated as can represent an interesting solution in all those industrial applications where close circuits are adopted (for example in heat exchangers).

Considering the synthetic polymers, it has been demonstrated that high values of drag reduction can be achieved with a tiny amount of injected polymer: with 1 ppm of *in-situ* polymer concentration, 20 % of drag reduction can be easily obtained. This effect increases with polymer concentration and with polymer molecular weight. In figure 5.1 percent of drag reduction is shown for 5 ppm polymer solutions, in the 30 mm pipe, for PEO 301 and PEO 308; the increased polymer molecular weight determines a significant increase in percent of drag reduction achieved and as shown in figure 4.14, in the polymer chain mechanical resistance. Moreover, for a given diameter, the onset of drag reduction (departure from the von Kármán law) occurs

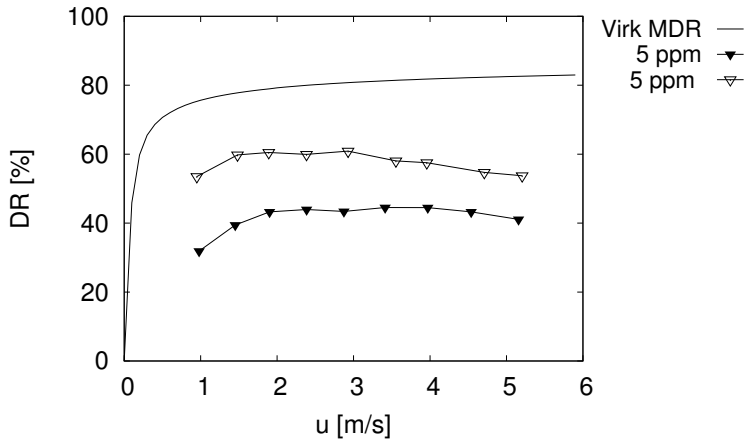

Figure 5.1: Percentage drag reduction as a function of the bulk velocity in the 30 mm pipe for 5 ppm solutions; solid symbols: PEO 301; open symbols: PEO 308. Solid line represents Virk's MDR.

at lower values of the friction Reynolds number with increasing polymer molecular weight: drag reduction can be achieved at lower values of the strain rate (lower flow rates, see fig. 4.8).

Comparing PEO and HPAM at a given concentration (see figs. 5.2 and 5.3), it can be noticed that HPAM is more effective than PEO in the 30 mm pipe while seems to degrade earlier in the 50 mm pipe. Moreover, if the experimental results are extrapolated up to the von Kármán law, HPAM seems to present an onset condition at very low values of the friction Reynolds number.

As summarised in chapter 1, drag reduction is more easily achieved in small pipes. This phenomenon has been verified also in the present experimental campaign where, for a given polymer concentration, the measured pressure loss, at same friction Reynolds number, is lower in the 30 mm pipe (see for example fig. 5.4).

This results is of great importance in industrial plants design since it has been proven that the amount of drag reduction obtained in a small experimental test rig can not be expected to occur in a larger industrial pipe; the difference may be considerable. In connection with these evidences, an interesting result is obtained when comparing the data for PEO 308 in the 30, 50 and 100 mm pipes. As can be seen in figure 5.5 the results for the 30 mm pipe are no longer higher than those for the 50 mm pipe: the higher molecular weight seems to reduce the difference in the results due to the pipe size. Moreover, results for the 100 mm pipe are above all the others. This difference may be imputed to the dynamics of the polymer once injected into the pure solvent flow: for the 30 and 50 mm

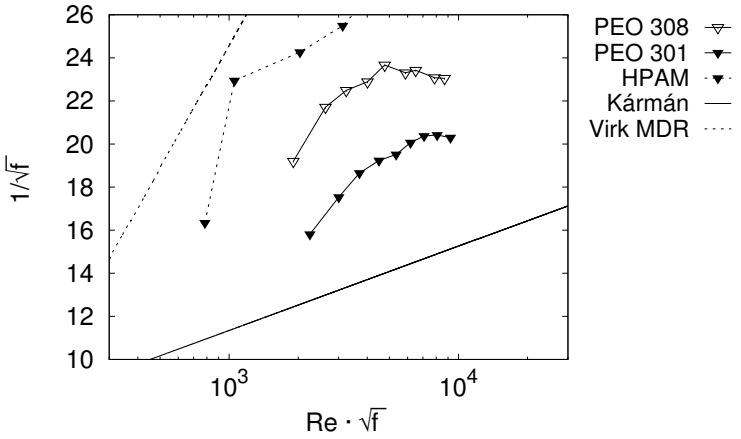

Figure 5.2: Comparison between PEO 301, PEO 308 and HPAM in *P-K* coordinates for 5 ppm in the 30 mm pipe.

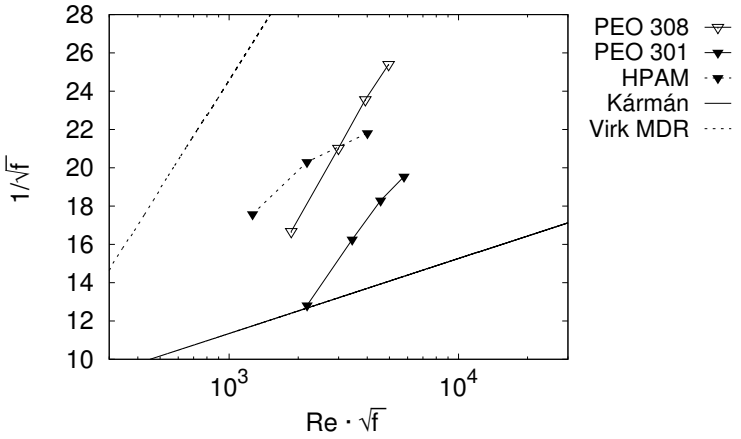

Figure 5.3: Comparison between PEO 301, PEO 308 and HPAM in *P-K* coordinates for 5 ppm in the 50 mm pipe.

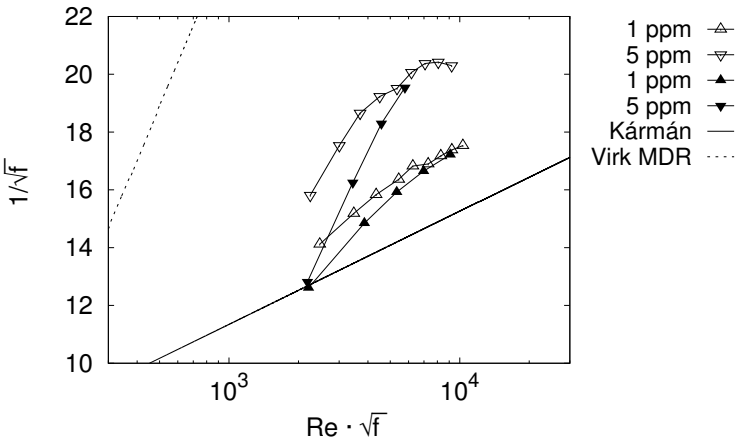

Figure 5.4: Comparison between 30 and 50 mm pipe, PEO 301; open symbols: 30 mm pipe; solid symbols: 50 mm pipe.

pipes, soon after the injection point, a mixing grid is present, enhancing the mixing process between the polymer and the solvent. In the case of the 100 mm pipe, no mixing enhancers were present and the injected polymer is supposed to remain as a thread inside the pure solvent flow, at least up to the measurement section (which is placed few diameters after the injection). Referring to Hoyt *et al.* [32] and Wyatt *et al.* [79] among others, this kind of heterogeneously injection is proven to be more effective than a diffused one (when polymer is completely homogenized soon after the injection). This result should be more investigated as soon as a new injection system is designed, to cover a broader range of flow rates, since the injection at the wall could represent a relevant option for existing industrial plants where any substantial modification to the pipe line may not be possible.

When homogeneous mixing is considered, the increased efficiency of the polymers in smaller pipes has to be ascribed, in our opinion, to the higher percentage of activated polymers with respect to the pipe cross section. It has been explained in section 1.2.1 and shown in figure 1.18 that there exist a limiting radial position y^+_{lim} below which (moving towards the wall) the polymers are activated (see dashed area in fig. 5.6): polymer deformation can occur with consequent absorption of part of the flow energy. Since the radial variation of r^{**} is a function of the polymer concentration (see Eq. (1.29)), at a given concentration and for a given τ_w (amount of deformation applied) the value of y^+_{lim} is fixed. Remembering that

$$y^+_{lim} = y\frac{u_\tau}{\nu} = (R - z)\frac{u_\tau}{\nu} \tag{5.1}$$

where R is the pipe radius and z is the generic radial position, if this quantity

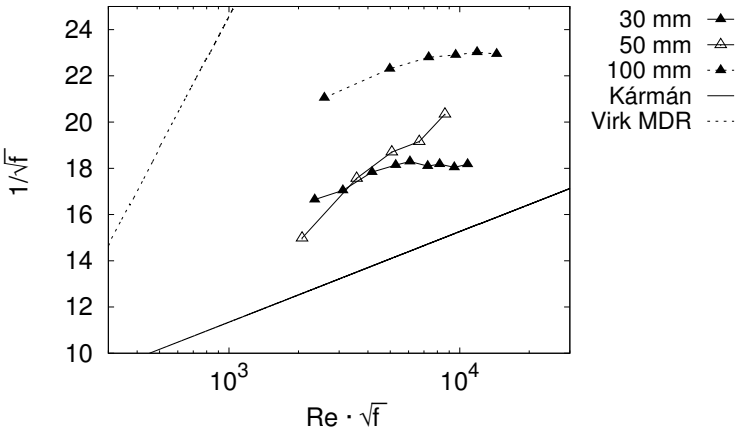

Figure 5.5: Comparison between 30, 50 and 100 mm pipe for 1 ppm, PEO 308.

has to remain constant, this means that $(R - z) = const.$

In pipes with different diameter (see fig. 5.7) this condition implies that, with respect to the pipe cross section, in a smaller pipe a larger part of the cross section presents scales lower than y^+_{lim}; this means that, assuming an homogeneous distribution of the polymer, a larger amount of polymer is activated and more energy can be subtracted from the flow structures, yielding to higher values of drag reduction compared to a bigger pipe.

Figure 5.8 shows the effects of the polymer molecular weight for the 30 and 50 mm pipes. It is evident that a higher molecular weight corresponds to higher values of drag reduction. Moreover, in larger pipes and for the higher molecular weight, polymer degradation is not registered (compare PEO 308 in 30 and 50 mm pipe).

The results presented in chapter 3 have proven that it is possible to profitably apply scaling relations [63] to scale-up the friction factors results to larger pipes, starting from those obtained in small scale experimental rigs. In this way it would be possible to assess the actual drag reduction effect in industrial scale pipes performing experiments in pilot scale rigs. If the prediction procedure proposed by [31] is applied, it is possible to predict the effect of polymer degradation in different pipe diameters, predicting both the onset friction Reynolds number, the slope increment and the merging with Virk's MDR. This may represent a relevant tool to predict the effect of polymer addition while designing brand-new industrial plants and pipelines. Moreover, the possibility to predict the drag reduction effects, given the flow conditions and the polymer concentration, may be used to assess the actual advantage in modifying existing pipelines.

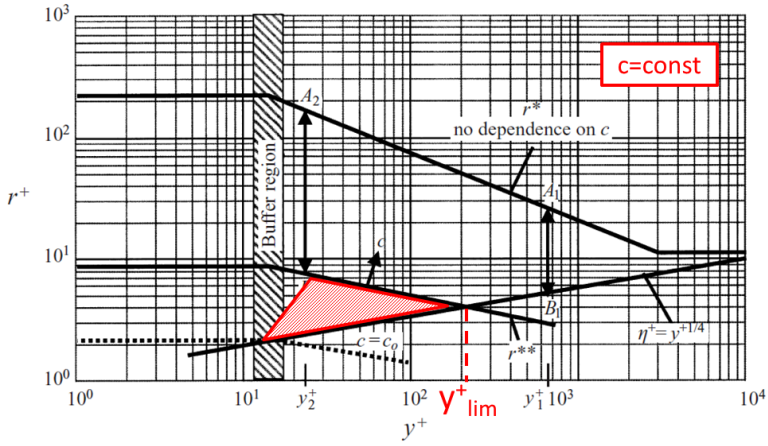

Figure 5.6: y^+_{lim} and polymer active area (dashed area). Adapted from Vanapalli *et al.* [72].

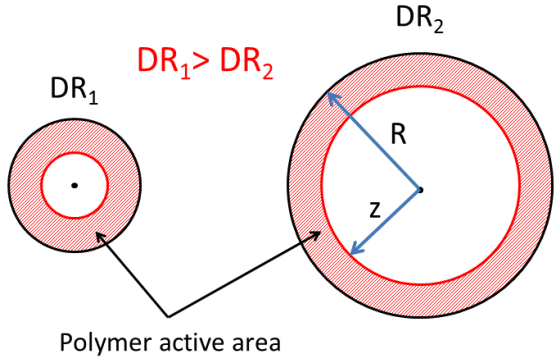

Figure 5.7: Polymer active area in pipes of different diameter.

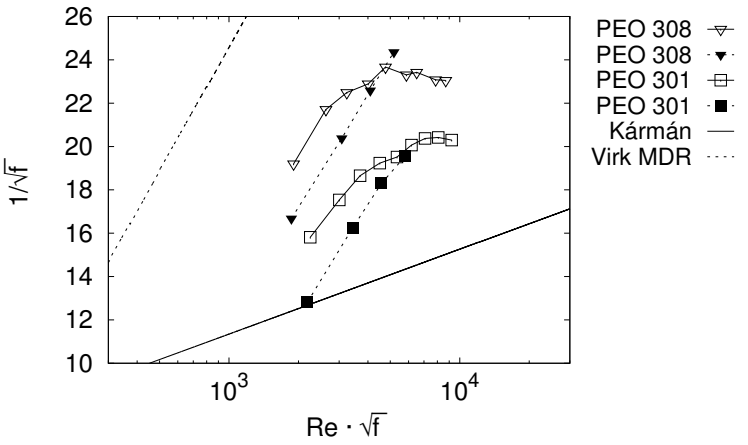

Figure 5.8: Combined effect of polymer molecular weight and pipe diameter: open symbols: 30 mm pipe; solid symbols: 50 mm pipe.

An interesting improvement of the aforementioned drag reduction prediction procedures is represented by the work of Vanapalli *et al.* [72] where new bounds for the maximum achievable drag reduction, rather than the MDR asymptote, are proposed. The introduction of polymer mechanical degradation within a prediction procedure represent a huge advantage in pipeline design. The results of the present experimental campaign were compared with the new bounds proposed and good agreement has been found (see figs. 4.13 to 4.15). Moreover, it has been verified that the molecular weight has a strong influence on the degradation process and that a higher molecular weight determines a stronger resistance to the degradation caused by the high levels of shear encountered in pipe's contractions and within the turbulent structures.

The analysis performed to predict the friction factors in visco-elastic flows can be directly related to a cost effectiveness evaluation of the adoption of polymers as drag reducers. In section 3.3.2 it has been demonstrated that, depending on the pipeline characteristics, the flow conditions and some economic variables (such as the price of polymer and electric energy) it is possible to assess the actual economical benefit of the polymer addition to the transferred medium. In figure 5.9 the costs per unit of mass of polymer (C_{poly}) and fluid pumping (C_{pump}), together with their sum (C_p), are presented as a function of polymer concentration for a given flow rate. The cost of fluid pumping, green line at the bottom, decreases with increasing polymer concentration thanks to drag reduction effects. The cost of the polymer, blue line at top, increases linearly with polymer concentration. If the sum of the two costs is considered, for the given flow conditions, a saving area can be identified with and optimum polymer concentration. It can be

noticed that there exist also a upper bound for the polymer concentration above which the increase in concentration represents only an extra-cost. This kind of evaluation, in our opinion, represents a relevant step-forward in the correct adoption of drag reducing agents in industrial applications.

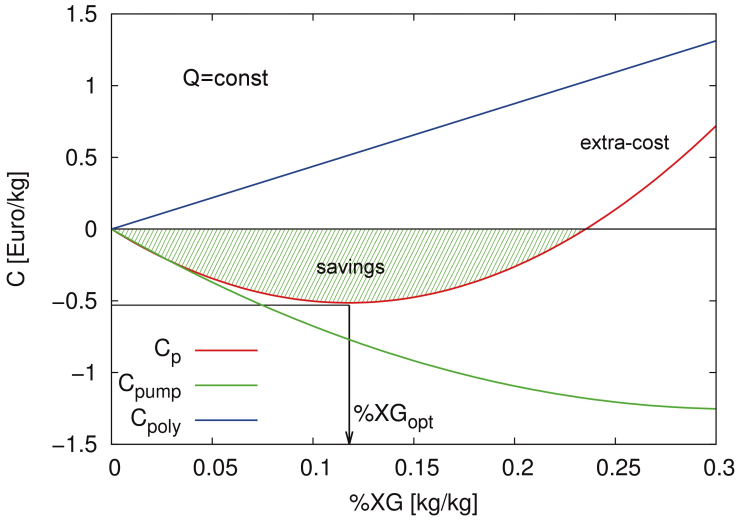

Figure 5.9: Cost effectiveness of polymer drag reduction and optimum polymer concentration.

To conclude, some future developments can be suggested. It would be interesting to complete the experimental matrix proposed in this work investigating the effect of the tested bio-polymer in the 30 and 50 mm pipes in pre-mixed homogeneous conditions and for all the three pipes, using the injection approach. Moreover, experiments with injected polymer should be conducted in the 100 mm pipe for all the synthetic polymer tested and if possible, an evaluation of the difference between threads and homogeneously mixed conditions should be performed. To achieve this results and to expand the investigated range of flow rates, a new injection system should be developed. As a result, a very interesting and complete data base of polymer drag reduction may be obtained: the investigation will comprise the effects of pipe diameter, polymer concentration, molecular weight and the difference behaviour between bio and synthetic polymers.

The relations adopted to scale-up and predict the friction factor behaviour seem to present an interesting outlook, especially when joined to a polymer degradation evaluation, and have to be tested more extensively to be considered a valuable tool during industrial plant design.

Promising results have also been obtained in fibres suspension flows added with polymers. This kind of suspensions should be investigated more

in detail: varying fibres characteristics and concentrations together with the added polymers and their concentrations. In particular it would be interesting to increase the fibres concentrations to assess any possible drag reduction effect by the fibres alone (preliminary results in this direction have been already found in this work; see fig. 6.1) and in synergy with polymers.

Considering multiphase flow, it maybe interesting to investigate the action of polymer in gas-liquid flow to verify if polymer addition can modify the flow regimes.

6

Future developments

6.1 Drag reduction in complex flows

In this chapter some preliminary results of fibres suspension flows are presented; the scope is to assess the possibility of achieving drag reduction even with rigid fibres and investigate some possible combined effects between fibres and polymers. Given the characteristics of the tested fibres (see section 2.3) and referring to the concentration regimes presented in table 1.1, three mass concentration have been tested: 0.25 %, 0.5 % and 0.75 %; corresponding to $nL^3 = 31$, 63, 95. All the solution are in the semi-dilute regime.

In figure 6.1 pressure drop per unit length in the 30 mm pipe is presented, with respect to the bulk velocity, for the three concentration. It can be seen that the three suspensions almost behave in the same manner; only for the higher concentration there is a small reduction in the pressure drop.

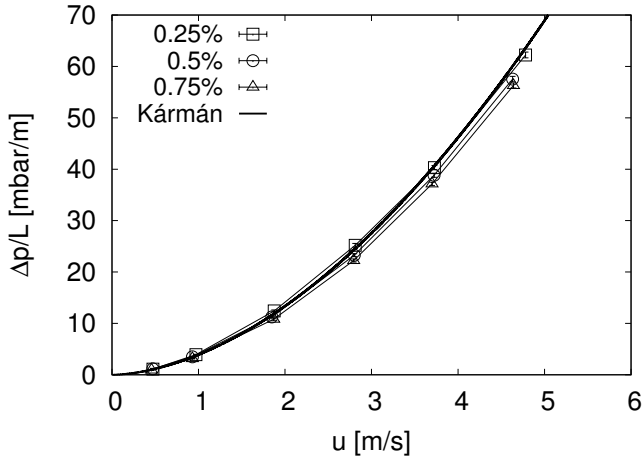

Figure 6.1: Pressure drop per unit length for fibres flow at three different concentrations in the 30 mm pipe.

A different behaviour can be deduced from figure 6.2 where the results for the 50 mm pipe are presented. It can be noticed that there is an increase

of the pressure drop for 0.25 % and 0.5 % while the higher concentration behaves like the pure water flow: the pressure drop is reduced with increasing the fibre concentration.

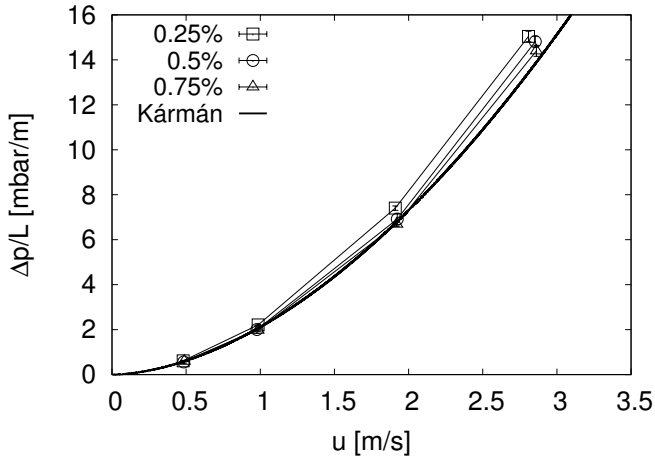

Figure 6.2: Pressure drop per unit length for fibres flow at three different concentrations in the 50 mm pipe.

To verify any possible synergetic effect of fibres and polymers drag reduction, three polymer concentrations have been added to each of the tested suspensions, for both pipes. The polymer used is PEO 308 with 0.5, 1 and 5 ppm. In the following plots, fibres pressure drop results (open symbols, solid line) are presented together with the fibres plus polymers flows (solid symbols with solid line) and the results with just the polymers (open symbols with dashed line), for both the pipes.

From figures 6.3, 6.4 and 6.5 it can be seen that the addition of the polymer determines for all the suspensions a drag reduction effect but the levels of pressure drop obtained are comparable with those of the polymer alone: no synergetic effect has been found. Only for the higher concentration and 0.5 and 1 ppm (see fig. 6.5), the pressure drop of the fibres plus polymer flow is lower than the polymer alone one.

In figures 6.6, 6.7 and 6.8 it can be seen that the behaviour is different with respect to the one encountered in the 30 mm pipe. For all the three cases it is possible to recover from the drag enhancement effect of the fibres suspensions but the results obtained with the addition of the polymer present a pressure drop higher than those with the polymer alone. This effect increases with increasing fibres concentration.

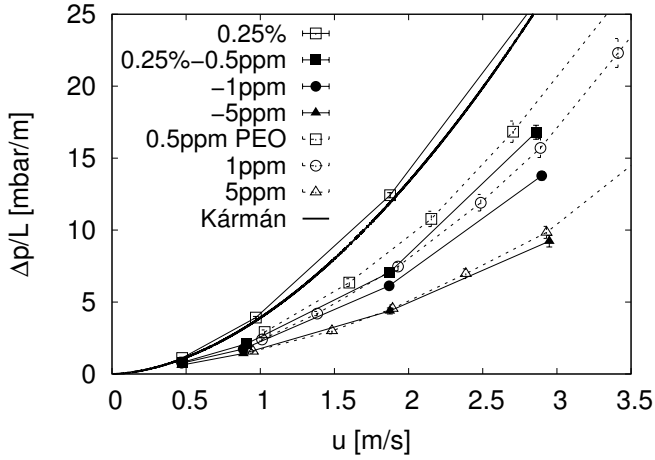

Figure 6.3: Pressure drop per unit length for 0.25 % fibres flow with polymer; open symbols with solid line: fibres pressure drop; solid symbols: fibres plus polymer pressure drop; open symbols with dashed line: polymer pressure drop. 30 mm pipe.

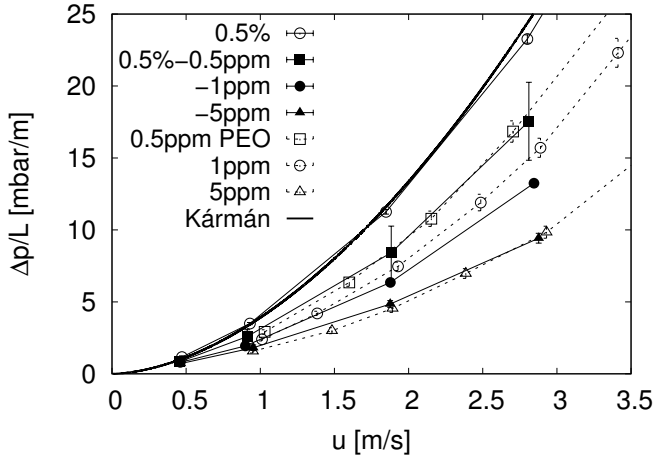

Figure 6.4: Pressure drop per unit length for 0.5 % fibres flow with polymer; open symbols with solid line: fibres pressure drop; solid symbols: fibres plus polymer pressure drop; open symbols with dashed line: polymer pressure drop. 30 mm pipe.

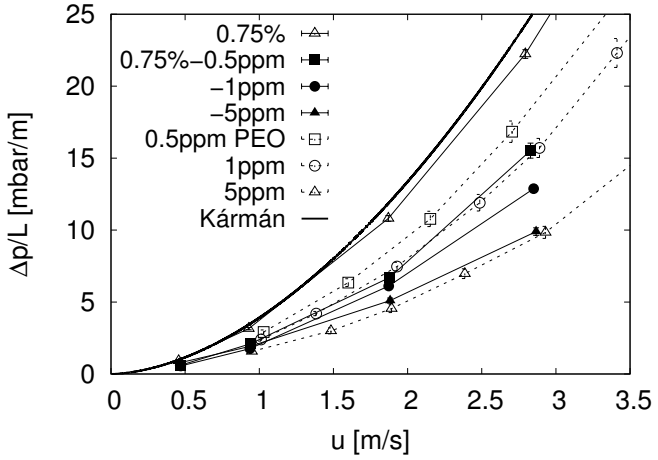

Figure 6.5: Pressure drop per unit length for 0.75 % fibres flow with polymer; open symbols with solid line: fibres pressure drop; solid symbols: fibres plus polymer pressure drop; open symbols with dashed line: polymer pressure drop. 30 mm pipe.

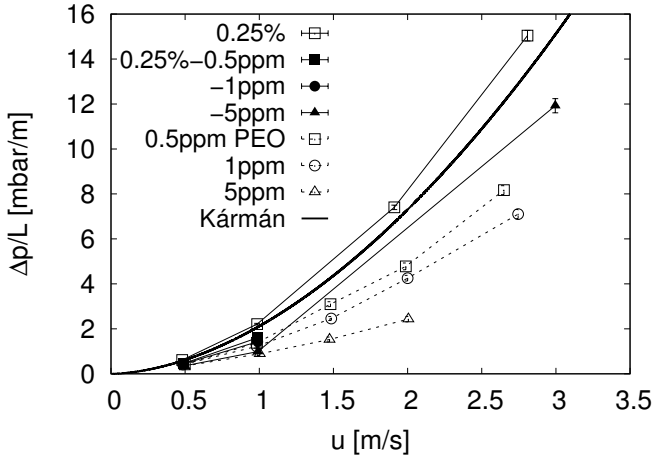

Figure 6.6: Pressure drop per unit length for 0.25 % fibres flow with polymer; open symbols with continuous line: fibres pressure drop; solid symbols: fibres plus polymer pressure drop; open symbols with dashed line: polymer pressure drop. 50 mm pipe.

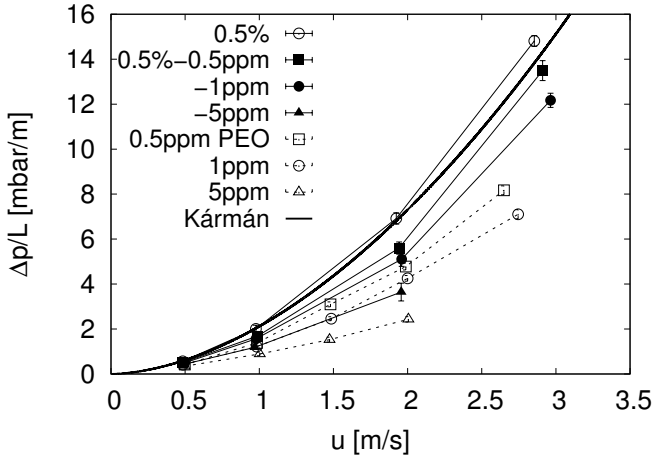

Figure 6.7: Pressure drop per unit length for 0.5 % fibres flow with polymer; open symbols with solid line: fibres pressure drop; solid symbols: fibres plus polymer pressure drop; open symbols with dashed line: polymer pressure drop. 50 mm pipe.

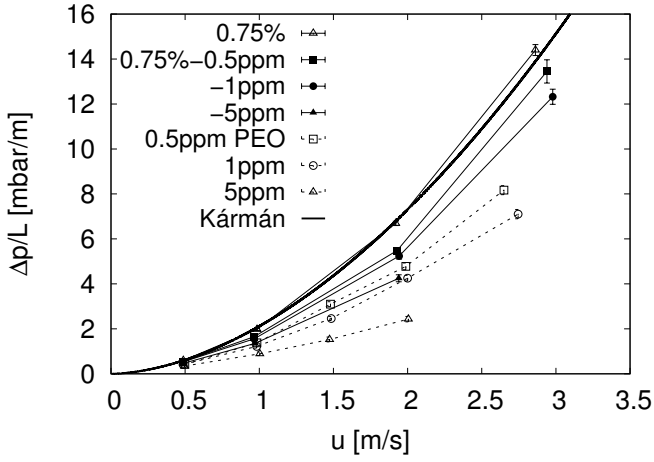

Figure 6.8: Pressure drop per unit length for 0.75 % fibres flow with polymer; open symbols with solid line: fibres pressure drop; solid symbols: fibres plus polymer pressure drop; open symbols with dashed line: polymer pressure drop. 50 mm pipe.

Appendices

A

Laboratory equipment

Pump

- Model: CALPEDA NM 65 /16 AE centrifugal pump
- Power: $15\,kW$
- Nominal engine frequency: $50\,Hz$
- Nominal speed: $2900\,rpm$
- Minimum flow rate at nominal speed: $Q = 48\,m^3/h$ with maximum head of $H = 38\,m$
- Maximum flow rate at nominal speed: $Q = 120\,m^3/h$ with maximum head of $H = 29\,m$
- Nominal current: $30\,A$ at $400\,V$ $\triangle$

Pump

- Model: KSB Sewabloc centrifugal pump
- Power: $22\,kW$
- Nominal engine frequency: $50\,Hz$
- Nominal speed: $1455\,rpm$
- Minimum flow rate at nominal speed: $Q = 9\,m^3/h$
- Maximum flow rate at nominal speed: $Q = 108\,m^3/h$
- Nominal current: $43\,A$ at $380\,V$ $\triangle$

Pump

- Model: Pedrollo NGAm 1A centrifugal pump
- Power: $0.75\,kW$
- Nominal engine frequency: $50\,Hz$
- Nominal speed: $2900\,rpm$
- Minimum flow rate at nominal speed: $Q = 3\,m^3/h$ with maximum head of $H = 19.5\,m$
- Maximum flow rate at nominal speed: $Q = 21\,m^3/h$ with maximum head of $H = 6\,m$
- Nominal current: $6.2\,A$ at $230\,V$

Inverter

- Model: SILCOVERT SVTplus by Asi Robicon
- Power supply: $380 - 480\,V$
- Output current: $30\,A$
- Power: $400\,V : 22\,kVA$

Flowmeter

- Model: ROTE YOKOGAWA Magnetic Flowmeter (SE208ME-DAE2S-LS4-D1H1/BSF)
- Nominal diameter $80\,mm$
- Power supply: $24\,V$ DC
- Analog signal output: $4 \div 20\,mA$ DC
- Minimum measurable flow rate: $5.425\,m^3/h$
- Maximum measurable flow rate: $180.95\,m^3/h$
- Accuracy: dependent on flow rate, refer to manual
- Maximum pressure: $200\,kPa$
- Temperature range: $-20 \div +60°C$

Flowmeter

- Model: Toshiba Tosmac 335/379

- Nominal diameter $100\,mm$
- Power supply: $220\,V$ DC
- Analog signal output: $4 \div 20\,mA$ DC
- Minimum measurable flow rate: N.A.
- Maximum measurable flow rate: $300\,l/min$
- Accuracy: dependent on flow rate, refer to manual
- Maximum pressure: $16\,bar$
- Temperature range: $-40 \div +65°C$

Flowmeter

- Model: Endress&Hauser Proline Promag 10
- Nominal diameter $50\,mm$
- Power supply: $12\,V$ DC
- Analog signal output: $4 \div 20\,mA$ DC
- Minimum measurable flow rate: $35\,l/min$
- Maximum measurable flow rate: $1100\,l/min$
- Accuracy: dependent on flow rate, refer to manual
- Maximum pressure: $16\,bar$
- Temperature range: $-10 \div +50°C$

Differential pressure transducer

- Model: Müeller MHDS Modular differential pressure transmitter
- Power supply: $15 \div 45\,V$ DC
- Analog output signal: $4 \div 20\,mA$ DC
- Measuring range: up to $700\,mbar$
- Turn down: up to $100:1$
- Accuracy: 0.0075% of FS up to turn down $10:1$; $\mp(0.0751 + 0.00751 \cdot URL/URV)$ for turn down $10:1$ to $100:1$ with URV: upper range limit of the instrument and URV: upper range value of the span

National Instrument FP-2000/FP-AI-110

- Power supply: $11 \div 30\,V$ DC
- Power consumption: $4.5\,W$
- Eight voltage input ranges: $0{-}1\,V$, $0{-}5\,V$, $\pm 60\,mV$, $\pm 300\,mV$, $\pm 1\,V$, $\pm 5\,V$ and $\pm 10\,V$
- Three current input ranges: $0 - 20$, $4 - 20$ and $\pm 20\,mA$
- 16-bit resolution
- Three filter settings: 50, 60, and $500\,Hz$
- Temperature range: $-40 \div +70°C$

National Instruments NI-USB 6210

- 16 analog inputs (16-bit, $250\,kS/s$)
- 4 digital inputs, 4 digital outputs
- Two 32-bit counters

Acknowledgments

I wish to express my gratitude to Professor Alfredo Soldati to have given me the opportunity to join his group and to develop my PhD programme at the best. I would also like to express my gratefulness to Professor Marina Campolo who strongly supported and encouraged me during the whole duration of my PhD period. My gratitude goes also to Professor Panagiota Angeli to have hosted me at her laboratory at University College London giving me the opportunity to improve the results of my research.

My gratitude goes to my Family who always supported and encouraged me and it is constantly my best reference point. I would also like to thank all my friends and colleagues.

Bibliography

[1] Y. Amarouchene et al. "Reynolds number dependence of drag reduction by rodlike polymers". In: *Physics of Fluids* 20.6, 065108 (2008).

[2] G. K. Batchelor. "The Stress Generated in a Non-Dilute Suspension of Elongated Particles by Pure Straining Motion". In: *Journal of Fluid Mechanics* 46 (1971), pp. 813–829.

[3] H. W. Bewersdorff and R. P. Singh. "Rheological and drag reduction characteristics of xanthan gum solutions". In: *Rheologica Acta* 27.6 (1988), pp. 617–627.

[4] M. Campolo et al. "Turbulent drag reduction by biopolymers in large scale pipes". In: *Journal of Fluids Engineering* 137.4 (2015), p. 041102.

[5] R. A. Chilton and R. Stainsby. "Pressure loss equations for laminar and turbulent non-Newtonian pipe flow". In: *Journal of Hydraulic Engineering-ASCE* 124.5 (1998), pp. 522–529.

[6] E. Choppe et al. "Rheology of xanthan solutions as a function of temperature, concentration and ionic strength". In: *Carbohydrate Polymers* 82.4 (2010), pp. 1228–1235. ISSN: 0144-8617.

[7] R. Colby. "Structure and linear viscoelasticity of flexible polymer solutions: comparison of polyelectrolyte and neutral polymer solutions". In: *Rheologica Acta* 49.5 (2010), pp. 425–442. ISSN: 0035-4511.

[8] C. F. Colebrook. "Turbulent flow in pipes, with particular reference to the transition region between the smooth and rough pipe laws". In: *J. Inst. Civil Eng.* 11.4 (1939), pp. 133–156.

[9] J. Daily and G. Bugliarello. "The Effect of Fibers on Velocity Distribution, Turbulence and Flow Resistance of Dilute Suspensions". In: *M.I.T. Hydrodynamics Laboratory Report* 30 (1958).

[10] E. De Angelis et al. "Drag reduction by a linear viscosity profile". In: *Physical Review E* 70 (5 Nov. 2004), p. 055301.

[11] P. G. De Gennes. "Coil-stretch transition of dilute flexible polymers under ultrahigh velocity gradients". In: *The Journal of Chemical Physics* 60.12 (1974), pp. 5030–5042.

[12] P. G. De Gennes. *Introduction to Polymer Dynamics*. Cambridge University Press, 1990.

[13] S. S. Dearing et al. "Phase discrimination and object fitting to measure fibers distribution and orientation in turbulent pipe flows". In: *Experiments in Fluids* 54.1, 1419 (2012). ISSN: 0723-4864.

[14] Y. Dubief et al. "New answer on the interaction between polymers and vortices in turbulent flows". In: *Flow Turbulence and Combusion* 74 (2005), pp. 311–329.

[15] Y. Dubief et al. "On the coherent drag-reducing and turbulent-anhancing behaviour of polymers in wall flows". In: *Journal of Fluid Mechanics* 514 (2004), pp. 271–280.

[16] K. W. Ebagninin, A. Benchabane, and K. Bekkour. "Rheological characterization of poly(ethylene oxide) solutions of different molecular weights". In: *Journal of Colloid and Interface Science* 336.1 (2009), pp. 360–367. ISSN: 0021-9797.

[17] B. R. Elbing et al. "Degradation of homogeneous polymer solutions in high shear turbulent pipe flow". In: *Experiments in Fluids* 47.6 (2009), pp. 1033–1044. ISSN: 0723-4864.

[18] M. P. Escudier, A. K. Nickson, and R. J. Poole. "Turbulent flow of viscoelastic shear-thinning liquids through a rectangular duct: Quantification of turbulence anisotropy". In: *Journal of Non-Newtonian Fluid Mechanics* 160.1 (2009), pp. 2–10.

[19] M. P. Escudier, F. Presti, and S. Smith. "Drag reduction in the turbulent pipe flow of polymers". In: *Journal of Non Newtonian Fluid Mechanics* 81 (1999), pp. 197–213.

[20] M. P. Escudier, F. Presti, and S. Smith. "Drag reduction in the turbulent pipe flow of polymers". In: *Journal of Non-Newtonian Fluid Mechanics* 81.3 (1999), pp. 197–213.

[21] M. P. Escudier et al. "On the reproducibility of the rheology of shear-thinning liquids". In: *Journal of Non-Newtonian Fluid Mechanics* 97.2–3 (2001), pp. 99–124. ISSN: 0377-0257.

[22] P. Escudier and S. Smith. "Fully developed turbulent flow of non-Newtonian liquids through a square duct". In: *Proceedings of the Royal Society of London A: Mathematical, Physical and Engineering Sciences* 457.2008 (2001), pp. 911–936. ISSN: 1364-5021.

[23] P. J. Flory. *Principles of Polymer Chemistry*. Cornell University Press, 1953.

[24] F. Garcia-Ochoa et al. "Xanthan gum: production, recovery and properties". In: *Biotechnology Advances* 18.7 (2000), pp. 549–579.

[25] K. Gasljevic, G. Aguilar, and E. F. Matthys. "An improved diameter scaling correlation for turbulent flow of drag-reducing polymer solutions". In: *Journal Non-Newtonian Fluid Mechanics* 84.2-3 (1999), pp. 131–148.

[26] K. Gasljevic, G. Aguilar, and E. F. Matthys. "Measurement of temperature profiles in turbulent pipe flow of polymer and surfactant drag-reducing solutions". In: *Physics of Fluids* 19.8 (2007), p. 083105.

[27] K. Gasljevic, G. Aguilar, and E. F. Matthys. "On two distinct types of drag-reducing fluids, diameter scaling, and turbulent profiles". In: *Journal of Non-Newtonian Fluid Mechanics* 96.3 (2001), pp. 405–425.

[28] R. A. Gore and C. T. Crowe. "Modulation of turbulence by dispersed phase". In: *Journal of Fluids Engineering* 113.2 (1991), pp. 304–307.

[29] K. J. Harder and W. G. Tiederman. "Drag Reduction and Turbulent Structure in Two-Dimensional Channel Flows". In: *Philosophical Transactions of the Royal Society of London A: Mathematical, Physical and Engineering Sciences* 336.1640 (1991), pp. 19–34. ISSN: 0962-8428.

[30] K. D. Housiadas and A. N. Beris. "Characteristic scales and drag reduction evaluation in turbulent channel flow of non constant viscosity viscoelastic fluids". In: *Physics of Fluids* 16.5 (2004), pp. 1581–1586.

[31] K. D. Housiadas and A. N. Beris. "On the skin friction coefficient in viscoelastic wall-bounded flows". In: *International Journal of Heat and Fluid Flow* 42 (2013), pp. 49–67. ISSN: 0142-727X.

[32] J. W. Hoyt. "Drag reduction by polymers and surfactants". In: *Viscous Drag Reduction in Boundary Layers* (1990), pp. 413–432.

[33] J. W. Hoyt. "Negative roughness and polymer drag reduction". In: *Experiments in Fluids* 11.2-3 (1991), pp. 142–146.

[34] J.W. Hoyt and R.H.J. Sellin. "Scale effects in polymer solution pipe flow". In: *Experiments in Fluids* 15.1 (1993), pp. 70–74. ISSN: 0723-4864.

[35] W. Interthal and H. Wilski. "Drag reduction experiments with very large pipes". In: *Colloid & Polymer Science* 263.3 (1985), pp. 217–229.

[36] Den Toonder J. M. J. "Drag reduction by polymer additives in the turbulent pipe flow: laboratory and numerical experiment". PhD. Delft, The Netherlands: Technische Universiteit Delft, 1999.

[37] Den Toonder J. M. J. et al. "Drag reduction by polymer additives in the turbulent pipe flow: laboratory and numerical experiment". In: *Journal of Fluid Mechanics* 337 (1997), pp. 193–231.

[38] A. Japper-Jaafar, M. P. Escudier, and R. J. Poole. "Drag reduction of biopolymer flows". In: *Journal of Applied Sciences* 11.9 (2010), pp. 1544–1551.

[39] A. Japper-Jaafar, M.P. Escudier, and R.J. Poole. "Laminar, transitional and turbulent annular flow of drag-reducing polymer solutions". In: *Journal of Non-Newtonian Fluid Mechanics* 165.19–20 (2010), pp. 1357–1372. ISSN: 0377-0257.

[40] A. D. Jenkins et al. "Glossary of basic terms in polymer science". In: *Pure and Applied Chemistry* 68.12 (1996), pp. 2287–2311.

[41] D. D. Joseph. *Fluid dynamics of viscoelastic liquids*. New York: Springer-Verlag, 1990.

[42] A. Kamel and S.N. Shah. “Effects of salinity and temperature on drag reduction characteristics of polymers in straight circular pipes”. In: *Journal of Petroleum Science and Engineering* 67.1–2 (2009), pp. 23–33. ISSN: 0920-4105.

[43] A. R. Khokhlov and F. Kremer. In: *Polymer Science: A Comprehensive Reference*. Ed. by K. Möller and M. Matyjaszewski. Amsterdam: Elsevier, 2012. ISBN: 978-0-08-087862-1.

[44] K. Kim and R. Sureshkumar. “Spatiotemporal evolution of hairpin eddies, Reynolds stress, and polymer torque in polymer drag-reduced turbulent channel flows”. In: *Physical Review E* 87 (6 June 2013), p. 063002.

[45] D. L. Koch and E. S. G. Shaqfeh. “The average rotation rate of a fiber in the linear flow of a semidilute suspension”. In: *Physics of Fluids A* 2.12 (1990), pp. 2093–2102.

[46] P. F. W. Lee and G. G. Duffy. “Relationship between velocity profiles and drag reduction in turbulent fibre suspension flow”. In: *AIChE Journal* 22.4 (1976), pp. 750–753.

[47] R. C. Little et al. “The Drag Reduction Phenomenon. Observed Characteristics, Improved Agents, and Proposed Mechanisms”. In: *Industrial & Engineering Chemistry Fundamentals* 14.4 (1975), pp. 283–296.

[48] J. L. Lumley. “Drag reduction by additives”. In: *Annual Review of Fluid Mechanics* 1.1 (1973), pp. 263–290.

[49] C. Marchioli and A. Soldati. “Mechanisms for particle transfer and segregation in a turbulent boundary laye”. In: *Journal of Fluid Mechanics* 468 (2002), pp. 283–315.

[50] A. B. Metzner and J. C. Reed. “Flow of non-newtonian fluids: correlation of the laminar, transition and turbulent flow regions”. In: *AIChE J.* 1.4 (1955), pp. 434–440.

[51] T. Min et al. “Drag reduction by polymer additives in a turbulent channel flow”. In: *Journal of Fluid Mechanics* 486 (June 2003), pp. 213–238. ISSN: 1469-7645.

[52] I. C. F. Moraes et al. “Dynamic and steady: shear rheological properties of xanthan and guar gums dispersed in yellow passion fruit pulp (Passiflora edulis f. flavicarpa)”. In: *Brazilian Journal of Chemical Engineering* 28 (Sept. 2011), pp. 483–494. ISSN: 0104-6632.

[53] J. S. Paschkewitz et al. “Numerical simulation of turbulent drag reduction using rigid fibres”. In: *Journal of Fluid Mechanics* 518 (2004), pp. 281–317.

[54] R. J. Poole and B. S. Ridley. “Development-Length Requirements for Fully Developed Laminar Pipe Flow of Inelastic Non-Newtonian Liquids”. In: *Journal of Fluids Engineering* 129.10 (2007), pp. 1281–1287.

[55] I. Procaccia, V. S. L'vov, and R. Benzi. "Colloquium: Theory of drag reduction by polymers in wall-bounded turbulence". In: *Rev. Mod. Phys.* 80.1 (2008), pp. 225–247.

[56] P. K. Ptasinski et al. "Experiments in turbulent pipe flow with polymer additives at maximum drag reduction". In: *Flow Turbulence and Combusion* 66 (2001), pp. 159–182.

[57] P. K. Ptasinski et al. "Turbulent channel flow near maximum drag reduction: simulations, experiments and mechanisms". In: *Journal of Fluid Mechanics* 490 (Sept. 2003), pp. 251–291. ISSN: 1469-7645.

[58] L. Radin, J. L. Zakin, and G. K. Patterson. "Drag reduction in solid-fluid systems". In: *AIChE Journa* 21 (1975), pp. 358–371.

[59] A. A. Robertson and S. G. Mason. "The flow characteristics of dilute fibre suspensions". In: *TAPPI Journal* 40.5 (1967), p. 326.

[60] A. B. Rodd, D. E. Dunstan, and D. V. Boger. "Characterisation of xanthan gum solutions using dynamic light scattering and rheology". In: *Carbohydrate Polymers* 42.2 (2000), pp. 159–174. ISSN: 0144-8617.

[61] S. Sasaki. "Drag reduction effect of rod-like polymer solutions. I. Influences of polymer concentration and rigidity of skeletal back bone". In: *Journal of the physical society of Japan* 60.23 (1991), pp. 868–878.

[62] C. M. Schroeder et al. "Characteristic Periodic Motion of Polymers in Shear Flow". In: *Physical Review Letters* 95 (1 July 2005), p. 018301.

[63] R. H. J. Sellin and M. Ollis. "Effect of pipe diameter on polymer drag reduction". In: *Industrial & Engineering Chemistry Product Research and Developement* 22.3 (1983), pp. 445–452.

[64] R. S. Sharma. "Drag reduction by fibers". In: *Canadian Journal of Chemical Engineering* 58.6 (1981), pp. 3–13.

[65] D. E. Smith, H. P. Babcock, and S. Chu. "Single-Polymer Dynamics in Steady Shear Flow". In: *Science* 283.5408 (1999), pp. 1724–1727.

[66] D. E. Smith and S. Chu. "Response of Flexible Polymers to a Sudden Elongational Flow". In: *Science* 281.5381 (1998), pp. 1335–1340.

[67] K. R. Sreenivasan and C. M. White. "The onset of drag reduction by dilute polymer additives, and the maximum drag reduction asymptote". In: *Journal of Fluid Mechanics* 409 (Apr. 2000), pp. 149–164. ISSN: 1469-7645.

[68] K. R. Sreenivasan and C. M. White. "The onset of drag reduction by dilute polymer additives, and the maximum drag reduction asymptote". In: *Journal of Fluid Mechanics* 409 (2000), pp. 149–164.

[69] J. H. Sung et al. "Mechanical degradation kinetics of poly(ethylene oxide) in a turbulent flow". In: *Korea-Australia Rheology Journal* 16.2 (2004), pp. 57–62.

[70] M. Tabor and P. G. de Gennes. "A cascade theory of drag reduction". In: *Europhysics Letters* 2.7 (1986), pp. 519–522.

[71] W. G. Tiederman, T. S. Luchik, and D. G. Bogard. "Wall-layer structure and drag reduction". In: *Journal of Fluid Mechanics* 156 (1985), pp. 419–437.

[72] S. A. Vanapalli, M. T. Islam, and M. J. Solomon. "Scission-induced bounds on maximum polymer drag reduction in turbulent flow". In: *Physics of Fluids*, 095108 (2005), pp. 1–11.

[73] R. C. Vaseleski and Metzner A. B. "Drag reduction in turbulent flow of fibre suspension". In: *AIChE Journal* 20.2 (1974), pp. 301–306.

[74] P. S. Virk. "Drag reduction fundamentals". In: *AIChE Journal* 21 (1975), pp. 625–656.

[75] P. S. Virk and D. L. Wagger. "Aspects of mechanisms in type B drag reduction fundamentals". In: *Structure of Turbulence and Drag Reduction*. Ed. by A. Gyr. Springer-Verlag, IUTAM Symposium, 1989, pp. 201–213.

[76] D. Vlassopoulos and W. R. Schowalter. "Characterization of the non-newtonian flow behavior of drag-reducing fluids". In: *Journal of Non-Newtonian Fluid Mech.* 49.2-3 (1993), pp. 205–250.

[77] C. M. White and Mungal M. G. "Mechanics and predictions of turbulent drag reduction with polymer additives". In: *Annual Review of Fluid Mechanics* 40 (2008), pp. 235–256.

[78] N. B. Wyatt. "Rheological changes with solvent conditions in entangled polyelectrolyte solutions". PhD. Golden, Colorado, USA: Colorado School of Mines, 2010.

[79] N. B. Wyatt and M. W. Liberatore. "Rheology and viscosity scaling of the polyelectrolyte xanthan gum". In: *Journal of Applied Polymer Science* 114.6 (2009), pp. 4076–4084. ISSN: 1097-4628.

[80] H. Xu. "Measurement of fiber suspension flow and forming jet velocity profile by pulsed ultrasonic doppler velocimetry". PhD. Atlanta, Georgia: The Institute of paper Science and Technology, 2003.

[81] K. Yasuda, R. C. Armstrong, and R. E. Cohen. "Shear flow properties of concentrated solutions of linear and star branched polystyrenes". In: *Rheologica Acta* 20.2 (1981), pp. 163–178. ISSN: 0035-4511.

[82] B. H. Zimm. "Dynamics of Polymer Molecules in Dilute Solution: Viscoelasticity, Flow Birefringence and Dielectric Loss". In: *The Journal of Chemical Physics* 24.2 (1956), pp. 269–278.